Pnictogen-Halide Semiconductors for Photovoltaics

Pengjun Liu

Worcester College

Inorganic Chemistry Laboratory, Department of Chemistry

University of Oxford

This thesis is submitted for the degree of

Doctor of Philosophy

September 2024

Declaration of Originality

I declare that the contents of this thesis are the result of my own work, except where specific reference is made to the work of others. This thesis has not been submitted in whole or in part for consideration for any other degree or qualification in this, or any other university. All figures from literature are obtained with permission as described in caption.

Pengjun Liu

September 2024

Abstract

Indoor photovoltaic (IPV) development has garnered increasing interest in recent years because of the potential to sustainably provide energy to the billions of autonomous devices part of the Internet of Things (IoT) ecosystem. The emission spectra of indoor light sources are narrower and blue-shifted compared to the standard terrestrial outdoor AM 1.5G solar spectrum, which is the reference spectrum for standard testing of solar energy conversion systems, with a specified standard irradiance of 1000 W/m^2[1]; AM stands for air mass coefficient. The intensity of indoor light sources is approximately three orders of magnitude lower than 1-sun illumination [2, 3]. Crystalline silicon photovoltaics (PVs), which dominate the outdoor PVs industry, are not suitable for indoor light harvesting because of their low bandgap and high dark currents, which limits their performance under indoor illumination. The current commercial IPV devices are hydrogen passivated amorphous silicon (a-Si:H), but have low efficiencies, typically in the range of 4.4% to 9.2%[4-8]. There is significant scope, therefore, to develop alternative classes of light absorbers that could more efficiently harvest energy from indoor lighting.

Lead halide perovskites (LHPs) have shown promise due to their superior optoelectronic properties (diffusion lengths > 1 μm in polycrystalline thin films) and power conversion efficiency (44.72% under indoor fluorescent tube illumination)[3]. However, the presence of lead gives rise to concerns about toxicity, especially since these devices will be predominantly used in consumer electronics, as well as the limited stability of the devices. These limitations have prompted research into lead-free alternative absorbers, with the aim of finding materials that could match or approach the optoelectronic properties of LHPs but surpass them in stability and overcome their toxicity limitations. This research focuses on caesium antimony-bismuth halides (vacancy-ordered triple perovskites) and silver bismuth halides, both of which have high theoretical optical limits in efficiency (>40%) under 1000 lux white light emitting diode (WLED) illumination, and which are free from elements that are restricted for use in consumer electronics.

But reaching the optical limits in efficiency requires long diffusion lengths, and this can be severely limited by carrier-phonon coupling. Therefore, I investigate the nature of carrier-phonon coupling in vacancy-ordered triple perovskites. Thin film samples were prepared through solution processing. I

confirm the samples to be phase pure via X-Ray Diffraction (XRD), with $Cs_3Bi_2I_9$ and $Cs_3Sb_2I_9$ having a 0D-structured hexagonal phase ($P6_3/mmc$ space group) while $Cs_3Bi_2Br_9$ and $Cs_3Sb_2Br_9$ are 2D-structured ($P\bar{3}m1$ space group). All four compositions were excitonic and showed large Stokes shift, which indicted presence of self-trapped excitons. I went into more depth into $Cs_3Bi_2I_9$, and confirmed via temperature-dependent PL that carrier localisation takes place in this material.

Next, I focus on $AgBiI_4$. This is a highly novel material for light harvesting, and I focus on developing the thin film synthesis route to achieve a dense morphology devoid of pinholes, which is necessary to develop these materials for PVs. Films were prepared on fluorine-doped tin oxide (FTO)-coated glass covered with compact TiO_2 films and a mesoporous TiO_2 scaffold. The effect of antisolvent treatment and precursor/substrate pre-heating temperature, as well as the annealing temperature on the final morphology of the films prepared were investigated. I obtained pinhole-free morphology through hot-casting at 110 °C and chlorobenzene antisolvent treatment during spin coating, but the power conversion efficiencies (PCEs) obtained for these devices were still poor. It is likely that device performance is fundamentally limited by short charge-charrier transport lengths, such as through carrier localisation and/or exciton formation.

I further collaborated with Prof. Shijing Sun's group from University of Washington to make use of machine learning models to analyse the morphology obtained from the parameters I investigated experimentally. Convolutional Neural Network (CNN) models were used to evaluate the density of pinholes in the scanning electron microscopy images, and the Segment Anything Model (SAM) was used to separate different regions within the images. The Reinforcement Learning (RL) algorithm was able to identify processing parameters that gave pinhole free morphology, but more data on continuous variables could potentially lead to extrapolation of parameters that lead to better thin films with larger grain sizes. The Random Forest (RF) algorithm extrapolated parameters that were unable to be reliably reproduced experimentally due to the model not accounting for batch-to-batch variation in the data supplier. This problem could potentially be resolved by tuning the weighing mechanics of the algorithm.

My thesis work offers insights into the efficiency-limiting mechanisms in vacancy-ordered triple perovskites, which may also be applicable in other bismuth- and antimony-based perovskite-inspired materials. Future investigations could focus on the effect of bismuth-antimony and bromide-iodide

alloying on the electronic dimensionality and self-trapping in these materials. My work also showed how the morphology of spin-coated $AgBiI_4$ thin films is dependent upon its processing conditions, but as device efficiency is still low despite pinhole free thin films, my work indicates that the performance of this material is inherently limited by the fundamental properties of the material itself, and future investigation should focus on identifying these factors, and whether they could be overcome through compositional engineering.

Acknowledgements

Reaching the end of my PhD has been both a challenging and rewarding experience, and I owe this achievement to the encouragement, guidance, and help of many remarkable people. First and foremost, I would like to express my deepest gratitude to my PhD supervisor, Dr. Robert Hoye, for his unwavering support and invaluable mentorship, especially during the challenging period when I began my PhD amidst the uncertainties of the COVID-19 pandemic. His guidance has been instrumental in the development of my research and helped me grow throughout my PhD.

My research group has been a pleasure and honour to work with. I would like to thank Dr. Jason Ye for his assistance with temperature-dependent photoluminescence (PL) and transient absorption spectroscopy (TAS) measurements, which were vital for my research. I also owe thanks to Xiaoyu Guo for taking PV and steady-state PL measurements for me. Special thanks to Dr. Yi-Teng Huang, Dr. Huimin Zhu, Dr Kaiwen Zhang, Dr. Daniel Price, Dr. Sachin R. Rondiya, and Hugh Lohan for their expertise guiding me over my PhD journey. Additionally, I'd like Yuchen Fu and Kavya Reddy Dudipala for supporting me throughout.

I am incredibly fortunate to have worked with such remarkable collaborators. I would like to extend my sincere thanks to Dr. Rob Palgrave, Dr. Shijing Sun and Kshithij Nandishwara for their insightful contributions and partnership. Collaborating with them has broadened my perspective and enriched my work in countless ways.

Beyond the academic realm, my friends have been a constant source of support and joy during these past years. A heartfelt thank you to Karen Zhu, Allison Ou, Zheni Fei, Tianning Tang, and Barbara Ding. Your friendship has been invaluable, helping me to balance the demands of research with moments of laughter and relaxation.

Finally, I would like to express my deepest gratitude to my parents, Guizhen Liu and Aimin Liu. Their love, support, and unwavering belief in me have been my foundation throughout this journey. Without their encouragement and sacrifices, none of this would have been possible.

To all of you, from the bottom of my heart, thank you for your guidance, support, and friendship.

Table of Contents

List of Figures

List of abbreviations

Abbreviation	Full description
ABS	Absorption spectroscopy
AHE	Adaptive histogram equalization
AM	Air mass coefficient
ARF	Ambient radiofrequency
BBO	Beta barium borate
CB	Conduction band
CBM	Conduction band minimum
CBO	Conduction band offset
CCD	Charge-coupled device
CIE	Commission Internationale de l'Éclairage
CNN	Convolutional neural network
DAP	donor–acceptor pair
DFT	Density functional theory
DI	De-ionized
DMF	*N*,*N*-dimethylformamide
DMSO	Dimethyl sulfoxide
EDX	Energy-dispersive X-ray
EQE	External quantum efficiency
ETA	Extremely thin absorber
ETL	Electron transport layers
FF	Fill factor
FTO	Fluorine tin oxide
FWHM	Full width at half maximum
GSB	Ground state bleach
HCl	Hydrochloric acid
HTL	Hole transport layers
IPA	Isopropyl alcohol
IPV	Indoor photovoltaic
IV	Current-voltage
LED	Light emitting diode
LHP	Lead-halide perovskite
LO	Longitudinal optical
NC	Nanocrystal
OPTP	Optical pump terahertz probe

PCE	power conversion efficiency
PDS	Photothermal Deflection Spectroscopy
PIA	Photo-induced absorption
PIM	Perovskite-inspired material
PL	Photoluminescence
PRTRMC	Pulse-radiolysis time-resolved microwave conductance
PSC	Perovskite solar cell
PTB7	Poly[[4,8-bis[(2-ethylhexyl)oxy]benzo[1,2-b:4,5-b']dithiophene-2,6-diyl][3-fluoro-2-[(2-ethylhexyl)carbonyl]thieno[3,4-b]thiophenediyl]])
PTFE	Polytetrafluoroethylene
PV	Photovoltaic
RF	Random forest
RFID	Radio-frequency identification
RL	Reinforcement learning
RoHS	Restriction of Hazardous Substances
SAM	Segment Anything Model
SE	Stimulated emission
SEM	Scanning electron microscopy
SHG	Second harmonic generation
SLME	Spectroscopic limited maximum efficiency
SQ	Shockley–Queisser
SRH	Shockley-Read-Hall
STE	Self-trapped exciton
TA	Transient absorption
TAS	Transient absorption spectroscopy
TC	Texture coefficient
TTIP	Titanium (IV) isopropoxide
UV	Ultraviolet
VB	Valence band
VBM	Valence band maximum
VBO	Valence band offset
WLED	White light emitting diode
WOLED	White organic LED
XRD	X-ray diffraction
α	Absorption coefficient
γ	Exciton–phonon coupling constant

μ	Reduced effective mass of exciton
τ	Carrier lifetime
ω	Characteristic frequency of the optical phonons

1 Introduction

The Internet of Things (IoT) is a rapidly growing market. It consists of a network of interconnected devices, such as digital technologies, low-power microprocessors, radio-frequency identification (RFID) tags, wireless sensors, and communication technologies. These devices are able to sense and process surrounding environmental data into useful information to end-users. This combination of smart sensor systems and wireless communications allows the enhancement of the quality and efficiency of our daily lives and businesses. Its usage spans from e-health applications such as wearable smart devices to smart buildings (e.g., smart home appliances such as ventilation and heating) to smart cities (e.g., smart cameras, smart lighting). As such, it is a rapidly growing market, with US$848 billion in revenue for the global market for IoT end-user solutions in 2023 and is predicted to reach ~US$ 1.56 trillion by 2029[9].

A key aspect of IoT is its 'intelligence', which requires cloud computing and end-user interaction. Therefore, a major portion of IoT devices needs to be equipped with data connectivity and without connections to a power grid for a functional IoT ecosystem. From this, the challenge of power supply arises. Currently, the mainstream approach is to use batteries as the power source. However, battery sizes are typically limited to below the cm^2-range in IoT devices, which exacerbates the problems of batteries having an inherently limited lifetime and require periodic replacement and maintenance. As the number of IoT devices grows, the frequency of battery replacement also grows and soon becomes unfeasible – Harrop[10] estimated that if batteries are to be the sole power supply of IoT nodes, then at least 80% of the potential of the IoT ecosystem would be unable to be actualized. There is also an economic concern in solely using batteries for IoT devices, as the need for frequent replacement results in a significant overhead maintenance cost, especially if they are sealed within infrastructure that make access difficult. Rechargeable batteries may remove the problem removal maintenance, but they are still constrained by the limited number of charge-discharge cycles and diminished performance and energy storage density after each cycle. Furthermore, the necessity for recharging introduces functional limitations, and is especially burdensome for IoT nodes placed in hard-to-reach locations. Therefore,

there is a strong demand for an alternate energy-harvesting system that enables IoT devices to operate independently.

Indoor photovoltaic (IPV) devices that convert ambient indoor light into electricity have come into focus as an attractive power supply as a significant number of IoT devices are used in indoor environments, and therefore may produce power by harvesting energy from ambient lighting. Other energy harvesting methods, such as thermoelectric, piezoelectric and ambient radiofrequency (ARF) energy harvesting have been considered, but IPV has the advantage of not being spatially constrained (compared to thermoelectrics, which are localised to heat source and sink) and piezoelectrics (required to be in the immediate vicinity of an actuator to stress the piezoelectric). Ambient lighting also has higher power densities than ambient radiofrequency waves[11]. Therefore, IPVs were chosen as the focus of alternate energy harvesting technology for IoT devices.

IPV differs from conventional outdoor solar PV in the power and spectrum of the light sources. The optimum bandgap for outdoor solar cells is 1.1-1.4 eV[12] while indoor light sources are typically fluorescent light tubes (FL) or white light-emitting diodes (WLED), for which the optimum bandgap is 1.9-2.0 eV[11]. This is because these light sources emit only over the visible wavelength range. Furthermore, the power density of indoor light is approximately three orders of magnitude lower than that of solar illumination (≈6–30 W m^{-2} compared to 1kW m^{-2})[13]. Currently, the dominant commercial IPV devices are hydrogen-passivated amorphous silicon (a-Si:H). These devices have a bandgap of 1.6 eV, which is closer to this optimal range than c-Si, and commercial a-Si:H IPVs under WLED or FL illumination have efficiencies of 4.4% to 9.2[5, 7, 14]. Given a-Si:H has long been commercialised, there are few prospects for substantial future improvements in efficiency, and there is therefore strong interest in developing other absorbers that could reach higher performance.

Recently, lead-halide perovskites have emerged as a promising IPV absorber due to their superior optoelectronic properties (diffusion lengths > 1μm) and its power conversion efficiency has recently reached 44.72%[3] under indoor lighting (U30 fluorescent light tubes at 1000 lux). However, toxicity and instability concerns arise with the presence lead, and in indoor usage, the only barrier between the end-user and the lead within the device would be the encapsulation layer which may fail in event of device damage. Hence, investigations have turned to searching for substitutions to Pb^{2+} to create

perovskite-inspired materials (PIMs). Antimony-/bismuth-halide perovskites ($A_3M_2X_9$ compounds where A^+ is a monovalent organic or alkali metal cation, M^{3+} is either Sb^{3+} or Bi^{3+} and X^- is a halide anion) have attracted significant attention. In particular, Sb^{3+} substitutes have qualitatively similar composition of orbitals at band-edges as lead-halide perovskites, which are conductive for defect tolerance[15], and its halide derivatives have a wide bandgap of around 2eV[16]. Antimony- and bismuth-based materials also have the advantage of being able to be synthesized on low-cost plastic substrates[17-20], which allows integration with a broad range of IoT devices, including flexible devices.

This research focuses on the investigation of caesium antimony-bismuth halides and silver bismuth iodide, both of which have been calculated to have high efficiency limits under indoor lightning conditions. The focus on caesium antimony-bismuth halides is the influence of dimensionality and composition on carrier localisation. For silver bismuth halide, the influence of processing conditions on absorber efficiency will be investigated. The PV performance of the devices under FL and WLED illumination will be used to assess whether their efficiency is sufficient for powering IoT devices.

2 Literature

2.1 Fundamentals

2.1.1 Charge carrier recombination

An electron-hole pair can be generated in the semiconductor when the incident photon energy is larger than the band gap energy (E_g). The absorption coefficient α of a material governs its photon absorption and hence its charge generation rate. For a material with uniform α, the electron-hole generation rate G(x) at a depth x is:

$$G(x) = \alpha F_0 e^{-\alpha x} \quad (1)$$

Where F_0 = incident monochromatic photon flux.

However, when the photon energy is larger than the band gap, the electrons will quickly dissipate the excess energy by colliding with the lattice until are back down to the conduction band edges in a process called thermalisation.

The efficiency of a semiconductor is also affected by charge recombination, where a conduction band electron loses energy and re-occupies an electron hole in the valence band. Carrier recombination can happen through multiple relaxation channels, which can be separated into two types: radiative and non-radiative. Radiative recombination occurs when energy is released by light emission or luminescence, and the characteristic time that describes this process is the lifetime, τ_r. The main radiative recombination mechanism is band-to-band recombination. Non-radiative recombination occurs when the excess energy is converted into heat by multi-phonon emission with a characteristic lifetime of τ_{nr}. The main non-radiative recombination types are trap-assisted recombination (including the one-trap Shockley-Read-Hall recombination model, or SRH [21] and surface recombination) and Auger recombination[22]. These recombination mechanisms are shown in Figure 1.

The carrier lifetime τ of a material is obtained from the rate of both types of recombination{Hoshi, 2017-06-07 #278}:

$$\frac{1}{\tau} = \frac{1}{\tau_{\mathrm{r}}} + \frac{1}{\tau_{\mathrm{nr}}}$$

(2)

Where τ_r is the average carrier lifetime due to radiative recombination and τ_{nr} is the average carrier lifetime due to nonradiative recombination.

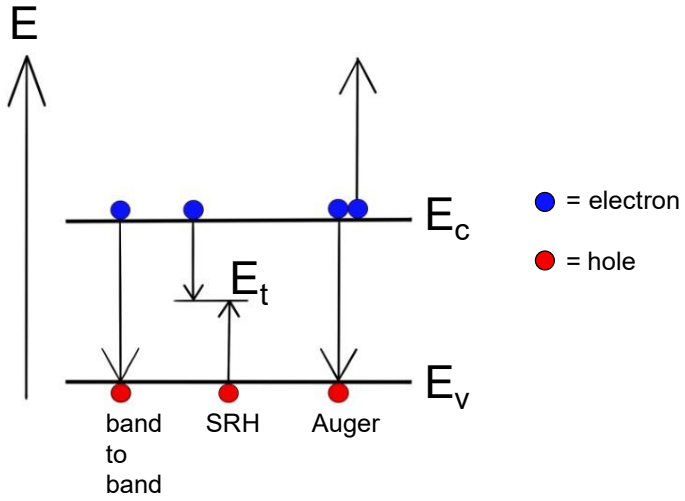

Figure 1. Diagram illustrating band to band, SRH and Auger recombination mechanisms. E_c is the conduction band energy, E_v is the valence band energy, and E_t is the trap state energy.

Band-to-band recombination occurs when electrons transition from the conduction band to the valence band and releases photon energy that are equal to or less than that of the incident photons. In thermal equilibrium, the radiative recombination R_0 and thermal generation rate G_0 are equal. This is given in the following equation[23]:

$$R_0 = G_0 = B_{\mathrm{r}} n_0 p_0 = B_{\mathrm{r}} {n_{\mathrm{i}}}^2$$

(3)

Where B_r = radiative recombination constant, n_i = intrinsic carrier density, n_0 and p_0 are the equilibrium carrier densities.

In the presence of electron-hole pairs, the net recombination rate R_r is given by[23]:

$$R_{\mathrm{r}} = B_{\mathrm{r}} np - G_0 = B_{\mathrm{r}} (np - {n_{\mathrm{i}}}^2)$$

(4)

In Shockley-Read-Hall recombination (SRH), also known as trap-assisted recombination, dopants and/or defects in the crystal lattice create new localized energy states. These are able to capture the free carriers transitioning between bands.

The Shockley-Read-Hall expression for the trap-assisted recombination R_{SRH} can be expressed as[23]:

$$R = \frac{np}{\tau_{\mathrm{n}}(p + p_{\mathrm{t}}) + \tau_{\mathrm{p}}(n + n_{\mathrm{t}})}$$

(5)

Where n_t and p_t = the electron and hole densities when the quasi-Fermi level matches the trap energy, τ_n and τ_p = the average lifetime for electrons and holes captured, and

$$n_{\mathrm{t}} = N_{\mathrm{c}} \exp\left[\frac{-(E_{\mathrm{c}} - E_{\mathrm{t}})}{kT}\right]$$

(6)

$$p_{\mathrm{t}} = N_{\mathrm{c}} \exp\left[\frac{-(E_{\mathrm{t}} - E_{\mathrm{v}})}{kT}\right]$$

(7)

Where N_c/N_v = effective density of states for electrons/holes, and $E_c/E_v/E_t$ = energy level of CB edge/VB edge/defect state[23].

Shallow defects are defect states near the band-edge where the trapped carriers could be easily released back to the band by thermal activation. Deep defects are those near the centre of the band gap which require much higher energy for captured electrons to be released.

Auger recombination occurs when the energy of the free carrier is passed to a third carrier, which is then excited to a higher energy level without moving from the energy band. The third carrier loses the excess energy via thermal vibrations and return to the band edge. Auger recombination is only significant when there is a high carrier density.

The non-equilibrium Auger recombination rate R_A given by[23]:

$$R_{\mathrm{A}} = C_{\mathrm{n}}(n^2 p - {n_0}^2 p_0)$$

(8)

Where C_n is the Auger capture probability.

Surface recombination occurs when traps at or near the surface form due to dangling bonds. It is a significant mechanism of recombination in PV devices due to the collection and extraction of free carriers at the surface. The net recombination rate due to surface recombination rate R_s is[23]:

$$R_{\mathrm{s}} = v_{\mathrm{s}}(n - n_0)$$

(9)

Where v_s = recombination velocity and n is the charge-carrier density on surface

The change in the carrier concentration in a semiconductor can be described by Poisson's equation[23]:

$$\frac{dp}{dt} = \frac{1}{q}\nabla J_{\mathrm{p}} + G_{\mathrm{p}} - R_{\mathrm{p}} \quad (For\ holes)$$

(10)

$$\frac{dn}{dt} = \frac{1}{q}\nabla J_{\mathrm{n}} + G_{\mathrm{n}} - R_{\mathrm{n}} \quad (For\ electrons)$$

(11)

Where n/p= electron/hole concentration, J_n/J_p = electron/hole current, G_n/G_p = generation rate for electrons/holes and R_n/R_p = recombination rate for electrons/holes.

2.1.2 Defects and defect tolerance

Defects are thermodynamically unavoidable at room temperature in all semiconductors[24]. They play a major role in affecting the conductivity, free carrier mobility and carrier lifetime of the semiconductor. Defects are typically divided into four different categories by dimensionality: 0D (vacancies or interstitials), 1D (dislocations), 2D (stacking faults or grain boundaries) and 3D (precipitates)[25].

Defects may introduce electronic energy states into the semiconductor band gap, which can be placed into two categories: shallow levels and deep levels. Shallow levels are located near their related band edges and are thermally ionized at room temperature. Therefore, shallow defects resemble acceptors and donors: they provide free carriers to form p-type or n-type semiconductor. Defects positioned deeper in the band gap are called deep defects and will bind the carriers much more strongly into highly compact, localized states. This type of defect will act as traps and recombination centers and are detrimental to minority carrier lifetimes.

Defect tolerance in perovskite solar cells gives them a major advantage over traditional silicon and GaAs solar cells. When the conduction band minimum (CBM) and the valence band maximum (VBM) is mainly composed of antibonding and bonding states respectively, deep defect states tend to be formed from vacancies and trap charge carriers, making the material defect intolerant. It has been proposed that the electronic band structure of lead-halide perovskites may result in shallow defects and so give rise to defect tolerance. A typical $MAPbI_3$ perovskite has both band-edges exhibiting an antibonding characteristic, with the CBM and VBM formed by the hybridization of Pb(6s)-I(5p) and Pb(6p)-I(5p) orbitals respectively. Hence anion vacancies produce defect energy levels near or within the band edges. Furthermore, the defect states are made shallower by the strong spin-orbital coupling between the lead nucleus and the electrons.

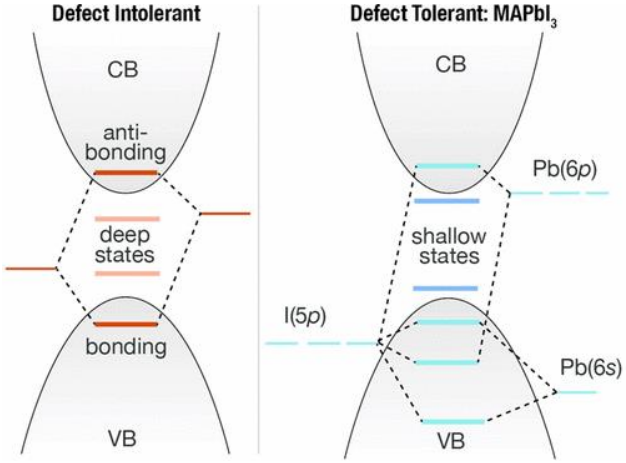

Figure 2. Electronic structures of typical semiconductor with the direct band gap (left) and $MAPbI_3$. Reproduced with permission from Chemistry of Materials,29 (11), 4667-4674(2017).[26] *Copyright © 2017 American Chemical Society.*

The Pb^{2+} in $MAPbI_3$ have stable valence $6s^2$ lone electron pairs which can lead to dispersive band-edges and strengthened antibonding characteristic. The coupling between the Pb lone pair s and the I p orbital push the VBM up and as a result the acceptors are generally shallower. Furthermore, the large electron cloud of the cation also induces a large Born effective charge (the coefficient of proportionality relating a change in polarization to atomic displacement), which results in a large dielectric constant ε_r. Therefore, the capture cross-section of a charged defect is reduced.

2.1.3 Carrier-phonon coupling

Charge carrier-phonon coupling has been associated with self-trapping character in semiconductors[27-29]. The conventional electronic band model of semiconductors, depicted in an E vs k diagram, provides insights into carrier mobility and recombination. However, carrier transport and recombination are also influenced by thermal displacements of atoms from their equilibrium positions. Atoms vibrate around their ideal crystallographic sites, and these vibrations, quantised by phonons, which can be optical or acoustic. Optical phonons involve out-of-phase vibrations of adjacent atoms, while acoustic phonons describe in-phase vibrations. For both optical and acoustic phonons, displacements occur either perpendicular (transverse mode) or in-plane (longitudinal mode) to the direction of propagation of an electron through the structure. The electron couples to phonons due to electrostatic interactions from the local dipoles created (note, there is no macroscopic dipole, since these local dipoles cancel out), or changes in electronic structure. Charge-carriers interacting with phonons behave as a quasi-particle, known as a polaron.

The Fröhlich interaction, involving longitudinal optical (LO) phonons, is a widely studied interaction in polar materials like Bi-based PIMs. When charge carriers couple to LO phonons, there is a variation in interatomic distances, resulting in energy fluctuations and electric polarization. Additionally, charge carriers can couple to acoustic phonons, leading to shorter-range interactions localized to one unit cell. If this coupling is strong, carriers can experience significantly reduced mobility, referred to as being "self-trapped," with the resulting polarons termed small polarons, in contrast to large polarons formed through more delocalized Fröhlich interactions.

The coupling between charge-carriers and LO phonons can be described by the Fröhlich coupling constant α_{OP}, which is given by[30]:

$$\alpha_{\mathrm{OP}} = \frac{1}{4\pi\epsilon_0}\frac{e^2}{\hbar}\left(\frac{1}{\epsilon_{\mathrm{optical}}} - \frac{1}{\epsilon_{\mathrm{static}}}\right)\sqrt{\frac{m^*}{2\hbar\omega_{\mathrm{LO}}}} \qquad (12)$$

where $\epsilon_{optical}$ and ϵ_{static} are the dielectric constant at high (optical) frequency and zero (static) frequency, respectively, $m*$ is the effective mass either for electrons or holes, and ω_{LO} is the characteristic frequency for LO phonons. Net dipole for longer when frequency decreases – more likely for carrier to be captured. When α_{OP} <1, the regime is considered weak. A α_{OP} of 1-10 is intermediate, and when it is >10 the regime becomes strong and self-trapping could occur.

The coupling between charge-carriers and acoustic phonons is characterised by deformation potential E_d and can be expressed as:

$$\Delta E = E_{\mathrm{d}} \frac{\Delta V}{V} \qquad (13)$$

Where V is the surrounding crystal volume, ΔV is the distorted volume from the charge-carrier, and ΔE is the change in the potential energy for the carrier. Charge carriers may be trapped inside this crystal distortion made by carrier-acoustic phonon coupling. The change in lattice energy as carriers become localized can be modelled by the following equation:

$$g_{\mathrm{ac}} = \frac{{E_{\mathrm{d}}}^2}{C_{\mathrm{a0}}} \frac{m}{3\pi\hbar^2} \qquad (14)$$

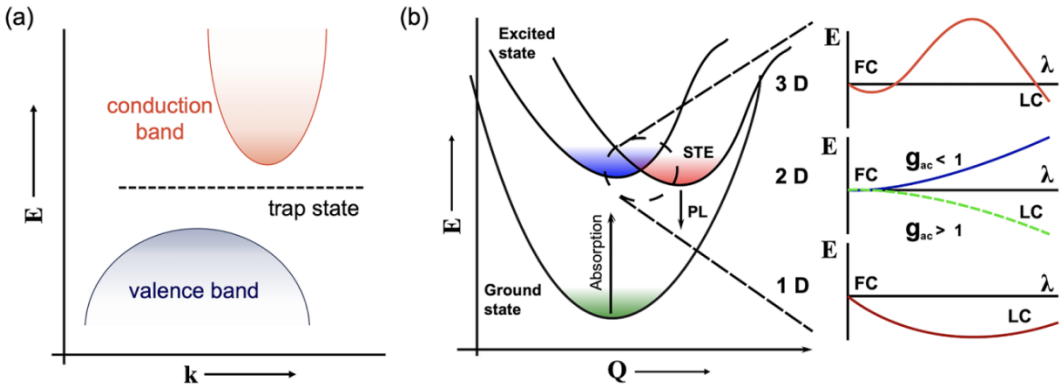

Figure 3. a) E vs k diagram of trap state in semiconductor b) diagram showing effect of dimensionality on self-trapping behaviour. Reproduced with permission under Creative Common CC BY License from Appl. Phys. Lett. 119, 220501 (2021). [31] *Copyright 2021.*

Where g_{ac} is the acoustic coupling factor, C is the elastic constant of the material, m is the effective mass of the electron, and $\hbar$ is the reduced Planck's constant. Self-trapping becomes energetically favourable when g_{ac} > 1. In this model, the energetically unstable free carriers undergoing localisation (λ = 0 relaxes to > 0 where λ is the dimensionless localisation parameter for structurally 3D, 2D an 1D

materials). Therefore, strength of coupling to acoustic phonons is not a barrier to self-trapping, but rather self-trapping becomes easier with reduced dimensionality as shown in Figure 3. Soft materials with low elastic constants and high acoustic deformation potential will have higher g_{ac} values.

2.2. Photovoltaic Devices

2.2.1 Working mechanisms of solar cell heterojunctions

A photovoltaic device must be able to separate the charge carriers that was generated upon absorption of photons in order to produce an external current, and also needs to have a quasi-Fermi level splitting in order to produce a voltage. In silicon solar cells, this is commonly accomplished by using a p-n junction – a diode made from a p-type and a n-type semiconductor. At the interface between the two semiconductors a depletion region that contains no carriers will form due to the majority carriers from both sides diffusing down the concentration gradient and recombining with the complementary carriers on the other side. When the free electrons in the n-region diffuse across the junction and combine with holes to form negative ions, positive ions are left at the donor impurity sites. Similarly, holes in the p-region leave behind negative ions. Therefore, a space charge is built up across the depletion region, creating an electric field that leads to band bending across the junction to align the Fermi level as shown in Figure 4.

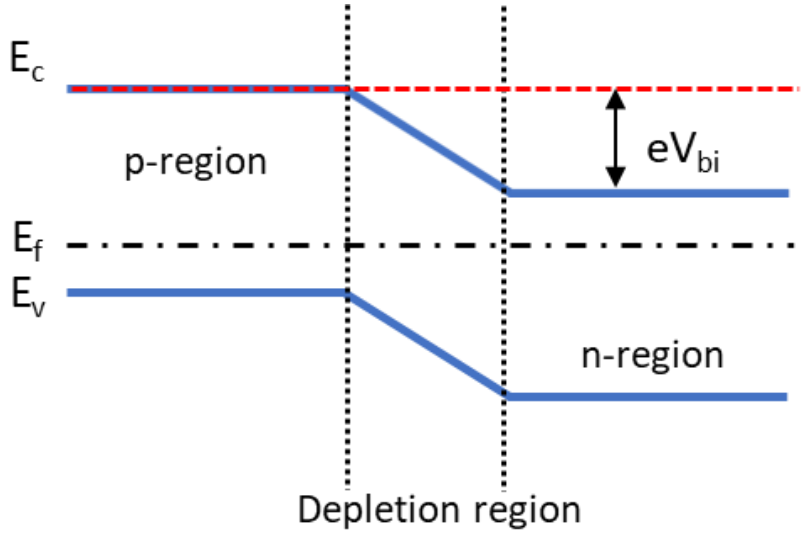

Figure 4. A simplified energy band diagram of a p-n junction.

The built-in electric potential eV_{bi} arising from the bent bands will prohibit any further charge-carrier diffusion a forward bias larger than eV_{bi} is applied. Under a reverse bias, the electric field of the depletion zone becomes stronger until it reaches a critical level where Zener or avalanche breakdown occurs and current begins to flow. The I-V characteristic of a p-n junction is as shown in Figure 5.

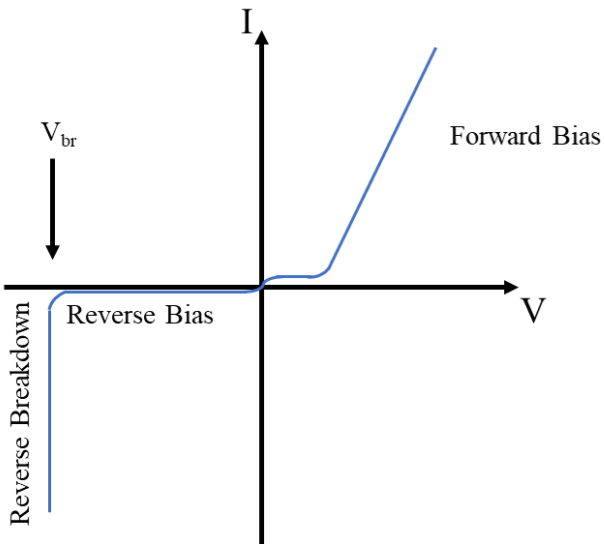

Figure 5. I-V characteristic of a p-n junction

For a p-n junction acting as a diode, the current from the diode I_D can be given as a function of the bias applied across the diode in the equation:

$$I_D = I_0(e^{\frac{qV}{nkT}} - 1) \quad (15)$$

Where: I_D = the net current flowing through the diode, I_0 = the diode leakage current in absence of light, also known as dark saturation current, V = applied voltage, n = the ideality factor, q = electron charge, k = Boltzmann's constant, and T = temperature (K).

The diode ideality factor n is a dimensionless parameter that quantifies the deviation of a real diode from the ideal behaviour and ranges from 1 – 2. An ideal diode would have an ideality factor equal to 1 - no non-radiative recombination at the heterojunction so current is dominated by diffusion of carriers. A value of *n* approaching 2 indicates that non-radiative recombination within the depletion region plays a significant role in the current flow.

Although p-n junctions are common in silicon solar cells, thin film photovoltaic devices tend to have a p-i-n structure. This is due to minority charge-carrier diffusion lengths are limited in thin films. As shown in Figure 6a), the p-i-n junction consists of an intrinsic semiconductor sandwiched between p-type and n-type semiconductors. The space charge region spans the entirety of the i-region, and hence the electric field can extend across this entire region, instead of having a depletion region that only partially covers the absorber layer as would typically be the case for p-n junctions.

As a result, photo-excited charge carriers within the intrinsic region are driven towards the junction ends, enhancing charge-carrier collection efficiency. Charge-carrier extraction is further improved in thin film solar devices by using materials with high carrier mobilities for n-and p-doped semiconductors in transport layers. For example, n-doped semiconductors such as TiO_2, ZnO, and SnO_2 are commonly used materials for electron transport layers (ETLs) while polymers (e.g. PTB7), Spiro-OMeTAD and MoOx are used as p-doped semiconductors for hole transport layers (HTLs). This is due to the alignment of energy bands at the semiconductor interfaces playing an important role in charge carrier injection, separation, and transport, and therefore critical to photovoltaic device efficiency. They are characterized by the conduction- and valence-band offsets at the heterojunctions and may present themselves as type-I (bandgap of one material is completely within the bandgap of the other, e.g. GaSb/AlSb), type-II staggered (bandgaps overlap but do not completely enclose, e.g. ZnSe/ZnTe), type-II broken-gap (bandgaps no dot overlap at all, e.g. InAs/GaSb), and type-III (heterojunction contains a semi-metallic compound, e.g. HgTe/CdTe)[32, 33].

In solar cells, efficient charge separation is critical and therefore Type-II staggered alignment is ideal for such devices. Conduction Band Offset (CBO) and Valence Band Offset (VBO) improves charge separation as electrons are directed toward the material with the lower CBM, while holes migrate to the material with the higher VBM. However, for efficient charge transfer across the heterojunction interface, the band alignment must minimize energy barriers: if the CBOs and VBOs are too large, charge carriers encounter significant resistance while crossing the junction, leading to energy losses. However, if the offsets are too small, there may be insufficient driving force for separation of charges. After separation and transfer, charge carriers must be extracted to their respective electrodes with minimal losses. The efficiency of charge extraction depends on the built-in electric field at the heterojunction interface as the differences in the Fermi levels of the two materials drives the carriers toward the electrodes. The energy levels of the materials adjacent to the electrodes must also match the work functions of the electrodes for charge extraction. A simplified scheme of a p-i-n junction solar cell (without band bending and assumed relative energy levels) is shown in Figure 6b) demonstrating the charge extraction mechanism.

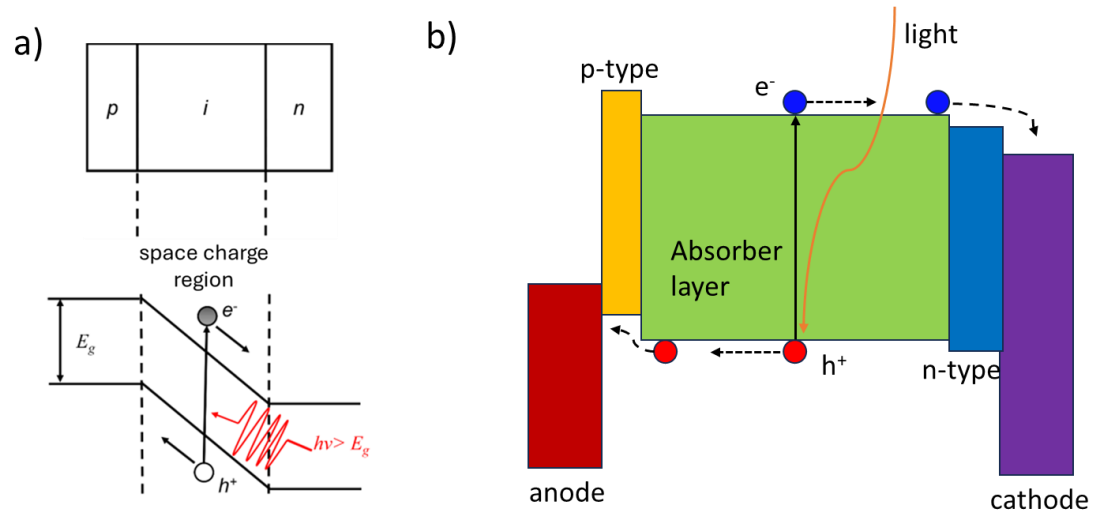

Figure 6. a) The energy band diagram of a p-i-n junction and b) working principle of a p-i-n junction solar cell

An ideal solar cell may be modelled by a current source in parallel with a diode (p-n junction). In practice no solar cell is ideal and parasitic resistances may dissipate the output power, degrading the performance of solar cells. The two most common parasitic resistances in a solar cell are the series resistance R_S, which arises from the net effect of the contact resistances between the electrodes and the semiconductor, and the shunt resistance R_{SH}, which is caused by the defects within the semiconductor. Hence the current produced by the solar cell, I, is equal to that produced by illumination, I_L minus that which flows through the diode, I_D, minus that which flows through the shunt resistor, I_{SH}:

$$I = I_L - I_D - I_{SH} \quad (16)$$

For a non-ideal diode, I_{SH} is given by the equation:

$$I_{SH} = \frac{V_j}{R_{SH}} \quad (17)$$

Where V_j = voltage across both diode and shunt resistor, and R_{SH} = shunt resistance.

The maximum current available from a solar cell occurs when the voltage across the solar cell is zero (i.e., when the solar cell is short circuited). This current is known as the short circuit current, I_{SC}. The maximum voltage available from a solar cell occurs at zero current, and is known as the open-circuit voltage, V_{OC}. It is equal to the maximum potential difference built up by quasi-Fermi level splitting.

Assuming that the shunt resistance is high enough to neglect the final term of the characteristic equation, V_{OC} can be given by the equation:

$$V_{\mathrm{OC}} = \frac{nkT}{q} \ln\left(\frac{I_{\mathrm{L}}}{I_0} + 1\right) \quad (18)$$

At both I_{SC} and V_{OC}, the power from the solar cell is zero. Hence another important parameter for solar cells is the fill factor (*FF*), which is defined as the ratio of the maximum power from the solar cell to the product of V_{OC} and I_{SC}:

$$FF = \frac{I_{\mathrm{M}} V_{\mathrm{M}}}{I_{\mathrm{SC}} V_{\mathrm{OC}}} \quad (19)$$

Where I_M = maximum current and V_M is maximum voltage

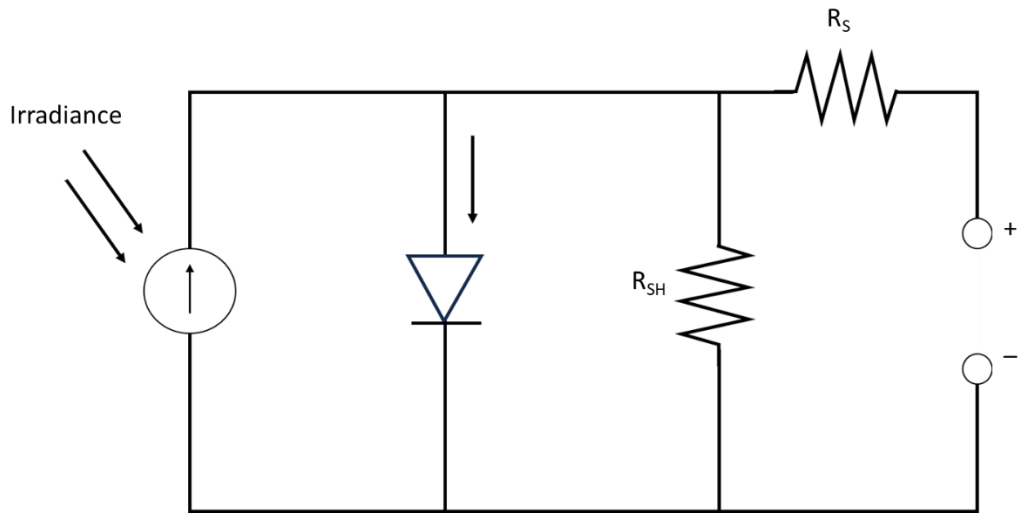

Figure 7. Equivalent circuit model diagram of a solar cell

However, this is a simplification, and a more complex model exists that accounts for series and shunt resistance based on the equivalent circuit mode as shown in Figure 6. For this model, J and FF can be described by the equations:

$$J = J_0\left(e^{\frac{q(V+JR_S)}{nk_BT}}\right) + \frac{V + JR_S}{R_{SH}} - J_{SC} \quad (20)$$

$$FF = FF_0\left[(1 - 1.1r_s) + \frac{r_S^2}{5.4}\right]\left[1 - \frac{V_{OC} + 0.7}{V_{OC}}\frac{FF_0}{r_{SH}}\left\{(1 - 1.1R_s) + \frac{r_S^2}{5.4}\right\}\right] \quad (21)$$

Where $r_S = R_S \frac{J_{SC}}{V_{OC}}$ and $r_{SH} = R_{SH} \frac{J_{SC}}{V_{OC}}$

Solar cell efficiency can also be evaluated by the power conversion efficiency (PCE):

$$PCE = \frac{I_{\mathrm{M}} V_{\mathrm{M}}}{P_{\mathrm{in}}} = \frac{I_{\mathrm{SC}} V_{\mathrm{OC}} FF}{P_{\mathrm{in}}}$$

(22)

Where P_{in} = incident illumination power.

The maximum theoretical efficiency of a solar cell made from a single p-n junction is known as the Shockley–Queisser limit. It assumes that the sun and the cell are both blackbodies with temperature T_s = 6000 K and T_c = 300 K, respectively, and that every photon from the sun with an energy larger than the bandgap of the semiconductor E_g will excite an electron-hole pair, but none of the photon with energy less than E_g will be absorbed. It also that radiative recombination is the only energy loss pathway, and the absorption profile is a step function with 100% external quantum efficiency (EQE) above the bandgap. The maximum theoretical PCE calculated for a device under the standard solar spectrum (AM 1.5G) is of 33.7% at 1.34 eV [12].

A better estimate of the theoretical PCE of a solar cell is the spectroscopic limited maximum efficiency (SLME). It utilises an energy-dependent absorption spectrum $a(E)$ instead of the step function used in the Shockley–Queisser model. In this model, EQE is identical to the absorptance (a(λ)). Both models are expressed through the equation[34]:

$$J_{\mathrm{sc}} = q \int_0^{\infty} \eta_{\mathrm{EQE}} \phi(\lambda) d\lambda$$

(23)

An ideal V_{OC}, assuming that the generated carriers only recombine radiatively under open-circuit condition as well as the same assumptions as that for SLME, then at thermal equilibrium without illumination, J_0 can be expressed as:

$$J_0 = q\pi \int_0^{\infty} a(E) I_{\mathrm{bb}}(E, T) dE$$

(24)

where $I_{BB}(E)$ is the spectral photon flux of blackbody radiation:

$$I_{\mathrm{bb}} = \frac{1}{4\pi^2 \hbar^3 c^2} \frac{E^2}{e^{\frac{E}{kT}} - 1}$$

(25)

And hence V_{OC} can be expressed as:

$$V_{\mathrm{OC}} = \frac{k_{\mathrm{B}}T}{q} \ln\left(\frac{J_{\mathrm{SC}}}{J_0} + 1\right)$$

(26)

For indirect bandgap semiconductors, there exists an extra non-radiative recombination that need to be accounted for:

$$J_0^n = \frac{J_0^r}{f_r}$$

(27)

Where J_0^{r} is the J_0 for direct bandgap semiconductor and $f_r = \exp\left(-\frac{E_{\mathrm{g}}^{\mathrm{da}} - E_{\mathrm{g}}}{k_{\mathrm{B}}T}\right)$

2.2.2 Indoor photovoltaics

The emission spectra of indoor light sources are more narrowly distributed and blue-shifted compared to the standard terrestrial outdoor AM 1.5G solar spectrum (the optimal bandgap for indoor light harvesting is ~1.9 eV compared, to 1.34eV for AM1.5G illumination), and the intensity of is approximately three orders of magnitude lower[11]. Therefore, the current dominant material in outdoor light harvesting, crystalline silicon (c-Si), is no longer suitable for this application. This is not just because its bandgap (1.12 eV) falls below the optimal value for indoor light harvesting, but also because at low lighting levels, its high dark currents severely limiting the efficiency. Alternative materials therefore need to be developed.

Currently, the industry standard material for indoor light harvesting is hydrogenated amorphous silicon (a-Si:H). Currently, it has an efficiency of 4.4%-9.2%[4-8], which is far below the radiative limit. It is inherently limited by defects present both in the material and at the interface[12, 35-37]. Furthermore, a-Si:H suffers from light-induced degradation which can cause the device to lose 10-20% (relative) of its initial PCE during the first few months of operation[11].

In an indoor light energy harvesting system, the ambient indoor light sources are a crucial point of consideration. The most commonly used indoor light sources are fluorescent (FL) and white light-emitting diode (WLED) lighting, which differs from outdoor light in that their emission spectra are purely in the visible wavelength range. The spectrum of the FL light sources has peaks at ~400 nm and ~600 nm, whereas white LED light has peaks at ~450 nm and ~550 nm of its spectrum[38]. As of 2023, IEC has released the first standard for IPV measurements. This species two standard light sources, a

WLED spectrum of 5000K colour temperature (CIE B4 LED), and FL spectrum of CIE FL10, but user-specified light sources are also permitted [39].

This difference in the emission spectra results in a difference in the Shockley–Queisser limit, which is the maximum theoretical efficiency of a photovoltaic device made from a single bandgap light absorber. The Shockley–Queisser (SQ)-limited efficiency η_{SQ} had been calculated by Ho *et al.*[40] with the equation:

$$\eta_{\mathrm{SQ}} = \eta_{\mathrm{u}} \times \eta_{d} \times \eta_{FF} \quad (28)$$

Where the ultimate efficiency η_u, the Shockley-Queisser efficiency limit η_d and the fill factor η_{FF} are the three sources of device energy loss. η_u results from the sub gap absorption loss and the energy loss of high-energy electron–hole (e–h) pairs relaxation, η_d originates from radiative recombination and the fill factor (*FF*) loss is from the non-square diode behaviour of the device.

Ho *et al*. showed that the ηSQ reaches a maximum value of ~57% at E_g= 1.82 and 1.96 eV (Figure 7) for various indoor light sources under 300 lux. Peng *et al.*[2] calculated a theoretical maximum efficiency SLME (calculated as discussed in Section 2.2.1) of ≈62% under both FL and WLED lighting with absorbers possessing a bandgap of 1.9 eV (Figure 8). The indoor ηSQ is significantly higher than that of solar light (33.7%) as a result of the narrower emission spectra reducing the dispersion of the incident photon energy, which leads to less thermalisation losses. They also found that the value of ηSQ and the corresponding optimal E_g have only a weak dependence on the type of indoor light source as long as the emission band is similar, which indicates a common optimal condition for IPVs. Another difference between indoor and outdoor lighting is that the power density of indoor light sources is ≈0.6–3 Wm^{-2}, which is around three orders of magnitude lower than the outdoor lighting power density of 170 Wm^{-2}[13]. This results in a reduction in the quasi-Fermi level splitting under indoor illumination compared to outdoor illumination, and hence a lower open-circuit voltage (*Voc*).

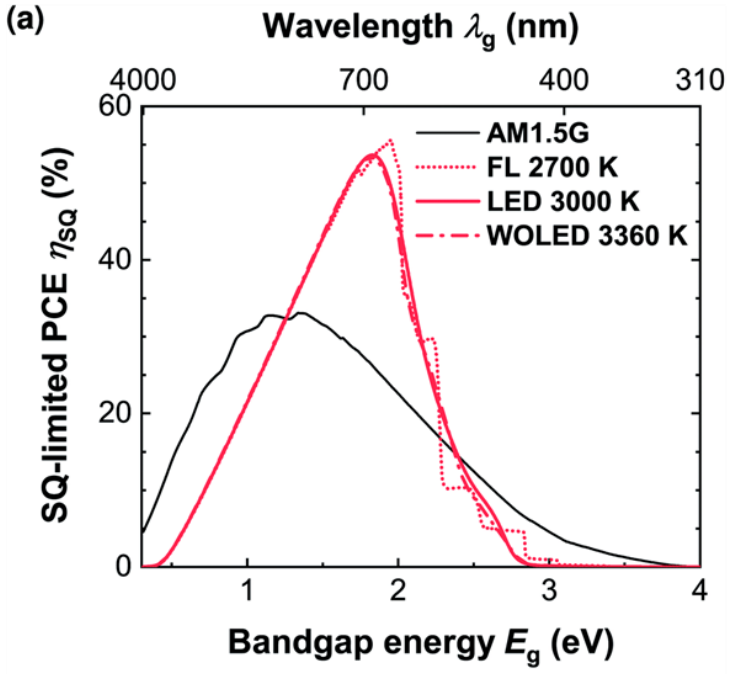

Figure 8. The Shockley–Queisser (SQ) limited power conversion efficiency (PCE) vs. bandgap energy E_g for different white light sources: sunlight (AM1.5G) and warm white fluorescent (FL) lamps, phosphor light-emitting diode (LED) light tubes and white organic LEDs (WOLEDs). Reproduced with permission from Journal of Materials Chemistry A, 2020/01/28. 8(4). [40] *Copyright 2020 Royal Society of Chemistry.*

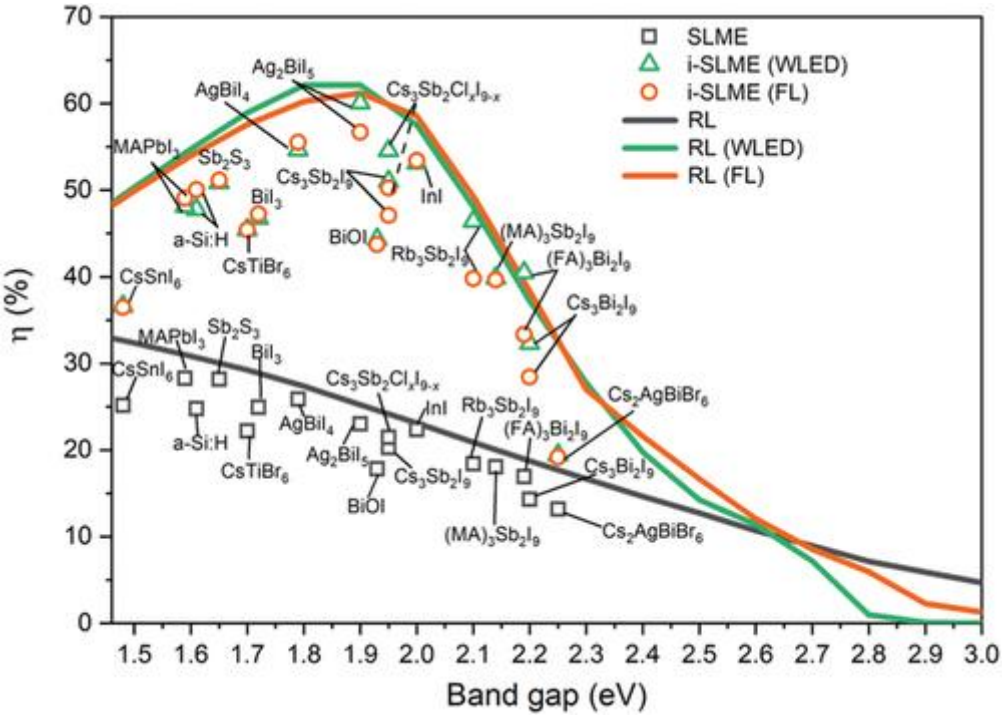

Figure 9. Indoor spectroscopic limited maximum efficiency (i-SLME) of various perovskite-inspired materials under WLED and FL spectra compared to the radiative limit (RL). FL and WLED light sources had irradiance of 340 μW cm^{-2} and 320 μW cm^{-2} respectively. The lamps

were adjusted to the appropriate height to achieve an illuminance of 1000 lux. Reproduced with permission under Creative Common CC BY Licence from Advanced Energy Materials, John Wiley and Sons (2020).[2] *Copyright 2020.*

2.3 Light-harvesting materials for outdoor and indoor photovoltaics

2.3.1. Lead-halide perovskite photovoltaics

Lead-halide perovskite (LHP) solar cells are currently the fastest-advancing solar technology, having increased efficiency from 3.8% in 2009 to a certified value of 26.7% in 2024 in single-junction architectures under outdoor illumination[41, 42]. For indoor lighting, efficiencies at 44.72% have been achieved[3]. Historically, the first compound discovered with this structure was $CaTiO_3$, discovered by Rose in 1839 and named after Lev Perovski[43]. Initial perovskite research was focused on oxides such as $BaTiO_3$, $PbTiO_3$, $SrTiO_3$, $BiFeO_3$, etc.[44-46]after this discovery, and PV applications were found to be limited to below 1.25% due to wide bandgaps of over 2.5 eV[47]. Lead-halide perovskite have rapidly overtaken oxide perovskites in terms of PV performance due to factors such as narrower bandgaps (e.g. 1.55 eV for $MAPbI_3$[48], high absorption coefficients of $\approx 10^5$ cm^{-1}[49, 50], long diffusion lengths, and defect tolerance[51-53].

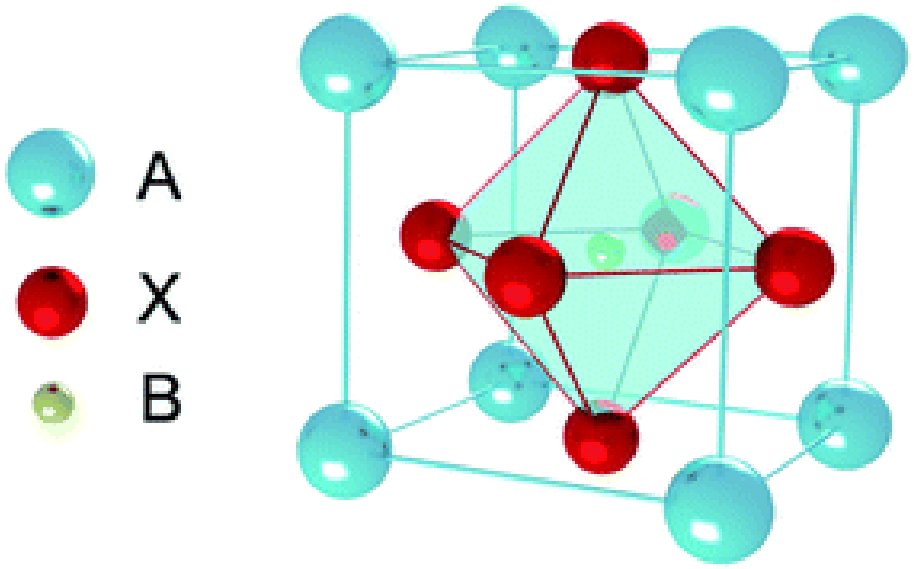

Figure 10. ABX_3 perovskite structure. Reproduced with permission under Creative Common CC BY Licence from RSC Adv.,8, 10489-10508, (2018).[54] Copyright 2018.

Perovskite crystal structure stability is determined by the Goldschmidt tolerance factor t:

$$t = \frac{r_A + r_B}{\sqrt{2}(r_A + r_X)} \quad (29)$$

Where r_A, r_B, and r_X are the ionic radii of A-site, B-site cations, and X-site anions respectively. For a stable perovskite crystal structure, the Goldschmidt tolerance factor must be between 0.8 and 1.1[55].

For t=1, the crystal will be of cubic structure. For 0.89 < t < 1, the crystal structure will be α-phase (cubic with slight distortion). 0.8 < t < 0.9 gives rise to tetragonal β -phase or orthorhombic γ -phase structure, while t > 1 gives rise to hexagonal or tetragonal crystal structure[56-59].

In LHPs the VBM and CBM, and therefore the bandgap, are primarily derived from the interactions between the B-site cation and the halide anions. The VBM is predominantly composed of the antibonding states formed by the overlap of the Pb^{2+} $6s^2$ lone-pair electrons and the p orbitals of the halide anions[60]. As previously mentioned in Section 2.1.2 and shown in Figure 2, this antibonding leads to a higher energy state at the VBM and so contributes to the material's defect tolerance by reducing the likelihood of deep trap states.[26] The bandgap of halide perovskites could also be tuned by altering the halide composition.[61] Substituting the halide anion (X) in the ABX_3 structure with different halides (e.g., Cl^-, Br^-, I^-) modifies the energy levels of the p orbitals involved in bonding. For instance, replacing iodide (I^-) with bromide (Br^-) or chloride (Cl^-) decreases the lattice constant and the electron affinity, which leads to the halide vacancy (0/+) donor level becoming deeper{Ganose, 2022-08-11 #277}. This leads to greater overlap between Pb dangling bonds when halide vacancies form and can lead to stronger carrier trapping due to the larger electrostatic potential. It also leads to a larger bandgap due stronger Coulomb potential separating the valence and conduction bands{Ganose, 2022-08-11 #277}.

Despite the demonstrated efficiency of perovskite solar cells, the presence of lead and the resulting toxicity and instability is a major issue on their commercialization. Only recently have companies obtained EU Restriction of Hazardous Substances (RoHS) certification[62] and have claimed up to 25 years of stability from encapsulation. However, the stability is still controversial as it is an extrapolation [62]. Phase transitions could occur in LHPs under the operational temperature range of -15 – 65 °C of a solar cell which has a significant effect on the optical and electrical properties of the device[63, 64]. Perovskite solar cells (PSCs) have also reported to experience moisture-[65] and light-[66, 67] induced degradation. Therefore, investigation into stable lead-free alternatives that could replicate the defect tolerance of the perovskite structure has garnered increasing interest.

2.3.2 Lead-free perovskite-inspired materials

To tackle the issues of replacing Pb with nontoxic elements while still maintaining device performance, studies have investigated different elements based on their similarity in size, charge, and chemical reactivity to Pb[68]. The most obvious chemical substitution of Pb^{2+} is to use B-site cations that also have a +2 oxidation state, but due to the limiting Goldschmidt tolerance factor only Sn^{2+} or Ge^{2+} can form the perovskite structure. Moving away from 2+ cations to replace Pb, double perovskites (structurally elpasolites) where two sets of Pb^{2+} cations are replaced to maintain charge neutrality have also been investigated. Finally, perovskite structure could be maintained using vacancies to balance charge, resulting in vacancy-ordered perovskites. The crystal structures of these perovskite-inspired materials are as shown in Figure 11.

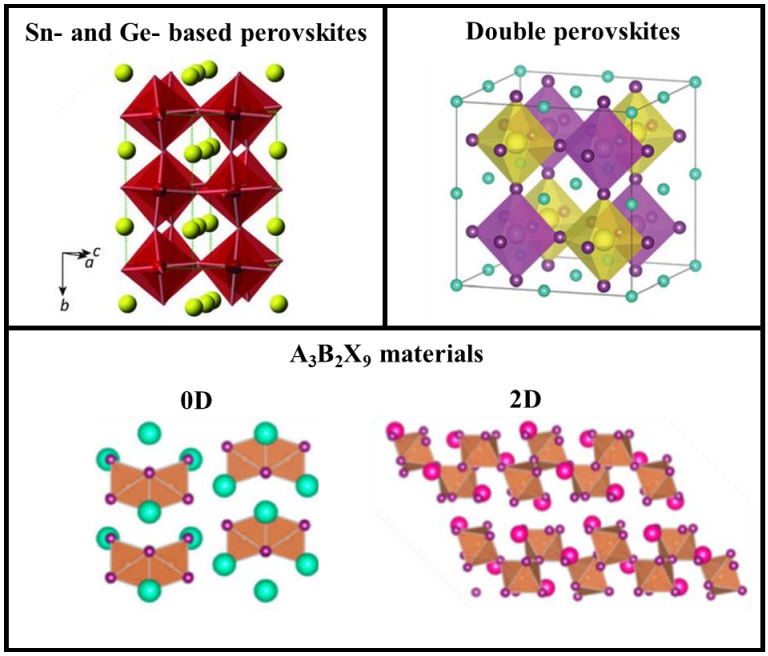

Figure 11. Crystal structures of Sn- and Ge-based perovskites (adapted with permission from John Wiley & Sons. ***8****,24 (2018)* [69] *Copyright 2018 John Wiley & Sons.) Double perovskites (adapted with permission from Advanced Energy Materials, John Wiley & Sons.* ***9****,12 (2019).*[70] *Copyright 2019 John Wiley & Sons.) and* $A_3B_2X_9$ *vacancy-ordered perovskites in 0D and 2D structure (adapted with permission from Chemistry of Materials.* ***30****, 11. ACS (2018).* [71] *Copyright 2018 American Chemical Society.)*

Currently, the reported performances of Sn and Ge-based photovoltaic devices are significantly poorer than those of lead halide perovskites[72-78] with the best Sn-based device performance being reported by Yu *et al.* as 14.81%[79] and the record for pure Ge-based devices have not passed 1%[80]. Theoretical

calculations[81] indicate that the low ionisation of tin-based perovskites lead to highly stable tin vacancies and interstitial defects easily forming below the valence band edge. This results in electrons being captured at the valence band edge and releases holes. Although this does not directly affect the carrier mobility, the tin vacancies lead a locally iodine-rich environment which promotes the Sn^{2+} oxidation to Sn^{4+}.

Double perovskites have a formula A_2BX_6 where A is a monovalent cation (e.g. Cs^+ or MA^+), X is a halide anion (e.g. I^-) and the B site may be composed of either a 4+ cation (e.g. Sn^{4+}) or a pair of cations one with a +1 formal oxidation state (*e.g.,* Ag^+) and the other with a +3 oxidation state (*e.g.*, Bi^{3+} or Sb^{3+}). Double perovskites have the advantage of having a 3D crystal structure, a long carrier lifetime (~660 ns for $Cs_2AgBiBr_6$[82]), as well as stability and bandgap tunability arising from the different combination of A, B and X ions. However, they have an indirect bandgap[83] which results in significantly lower PCE than lead-halide perovskites.

Another way to replace Pb while keeping the perovskite structure is by using vacancies to maintain charge balance, resulting in vacancy-ordered perovskites as shown in Figure 11. Vacancy-ordered double perovskites can be formed by replacing every other +4 cation with a vacancy to give A_2BX_6 compounds. Vacancy-ordered triple perovskites have a composition of $A_3M_2X_9$ with one vacancy out of every three +3 cations (e.g., Bi^{3+}). Vacancy-ordered perovskites also have good stability and bandgap tunability for photovoltaic applications. However, researchers have focused more on vacancy-ordered double perovskites compared to vacancy-ordered triple perovskites as the former have intrinsically lower bandgaps that are more suitable for solar cell applications[84, 85]. Although vacancy triple perovskites have larger bandgaps, they could be potentially used in indoor photovoltaic applications.

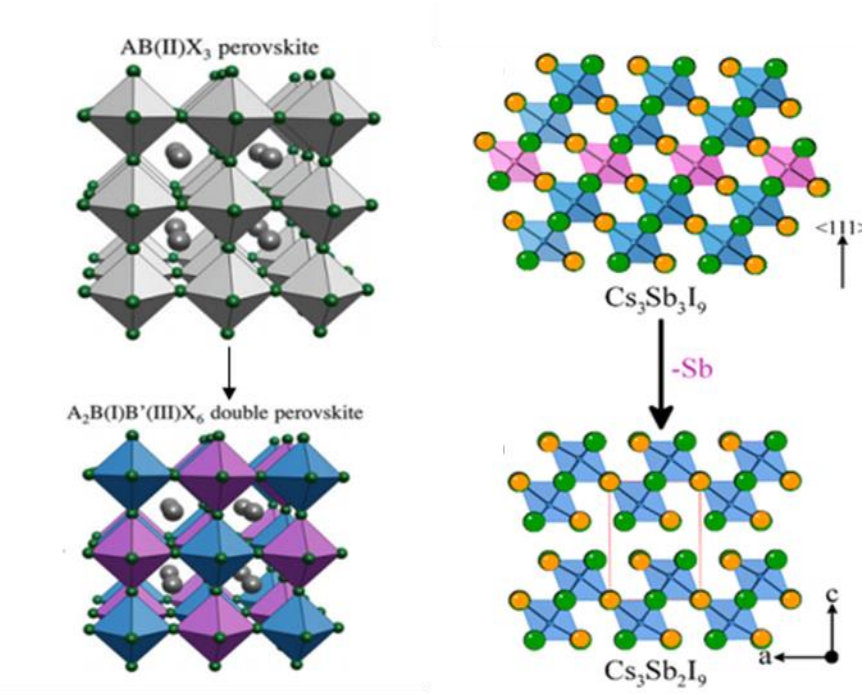

Figure 12. Crystal structure of vacancy ordered double perovskite (left) and vacancy ordered triple perovskite. Adapted with permission from Handbook of Materials Modeling. Springer, Cham.(2018).[86] *Copyright 2018 Springer Nature. And from Chemistry of Materials, August 6, 2015. 27(16) under ACS AuthorChoice license.* [87] *Copyright 2015 American Chemical Society.*

2.3.3. Compositional effects on structural dimensionality of vacancy-ordered triple perovskites

Conventional $A_3B_2X_9$ vacancy-ordered triple perovskites have Cs^+, Rb^+ or K^+ as their A-site cations, Bi^{3+} or Sb^{3+} as their B-site cations, and Cl^-, Br^- or I^- as their X-site anions. It is important to understand the effect of composition of each species (e.g. Bi^{3+} vs Sb^{3+}) has on the electronic properties and the structure as they are integral to the optoelectronic properties and hence practical applications of $A_3B_2X_9$. Different compositions have been found to crystallize into different space groups. In the cases where the pnictogen species differ but the crystal structure remains the same, Sb^{3+}- based compounds have higher angle diffraction peaks than Bi^{3+} based compounds due to lattice contraction.

Of the chloride-based compounds, $Cs_3Bi_2Cl_9$ has been reported to have a pure trigonal phase (space group: *Pmcn)*[88]. Pradhan *et al.*[89] synthesized $Cs_3Sb_2Cl_9$ with this structure at temperatures below 85 °C, but obtained an addition polymorph of a pure orthorhombic phase (space group *Pnma*) when synthesizing above 130 °C. A mix of the trigonal and orthorhombic phase was present for synthesis between 85 – 130 °C. It was also reported that when the reaction temperature for $Cs_3Sb_2Cl_9$ was kept

between 85 and 130 °C, a mixture of both trigonal and orthorhombic phases was obtained[89]. The trigonal phase consists of corner shared sharing [$BiCl_6$] or [$SbCl_6$] octahedra that form layers of hexagonal structures held to each other via van der Waal forces[88, 89] while the orthorhombic phase consists of 1D chains of the [$SbCl_6$] octahedra.

Bromide-based compounds such as $Cs_3Sb_2Br_9$ and $Cs_3Bi_2Br_9$ crystallize into structurally 2D compounds, with a space group of $P\bar{3}m1$[90, 91]. However, although the $P\bar{3}m1$ space group for bromide- and iodide-based compounds also consists of corner-sharing octahedra, the two octahedra shares one vertex, which differs from the chlorine-based compounds that consist of four octahedra sharing four Cl vertices[88, 91]. $Cs_3Bi_2Br_9$ have been found to have second-order phase transition at 96 K to $C12/c1$[92] while $Cs_3Sb_2Br_9$ have been reported to be stable from 80-300K[93].

Iodide-based compounds form different structures depending upon the composition. Both $Cs_3Sb_2I_9$ and $Cs_3Bi_2I_9$ form a hexagonal structure with the space group $P6_3/mmc$[94]. This is due to the octahedra fusing together to form face sharing dimers, which are electronically isolated from each other, giving a structurally 0D compound. However, $Cs_3Bi_2I_9$ at low temperatures (<130 K) have space group $C2/c$[95] while $Cs_3Sb_2I_9$ has a sequence of phase transitions at 85 K, 78 K and 72.1 K.[96]. A 2D $P\bar{3}m1$ structure that is more commonly seen in of bromide-based compounds could also occur in $Cs_3Sb_2I_9$ at high temperatures of ~300 °C[87]. It has also been reported that replacing the Cs^+ cation with the smaller Rb^+ cation for the iodide compounds will result in a change to a 2D structure of space group $P2_1/n$[97].

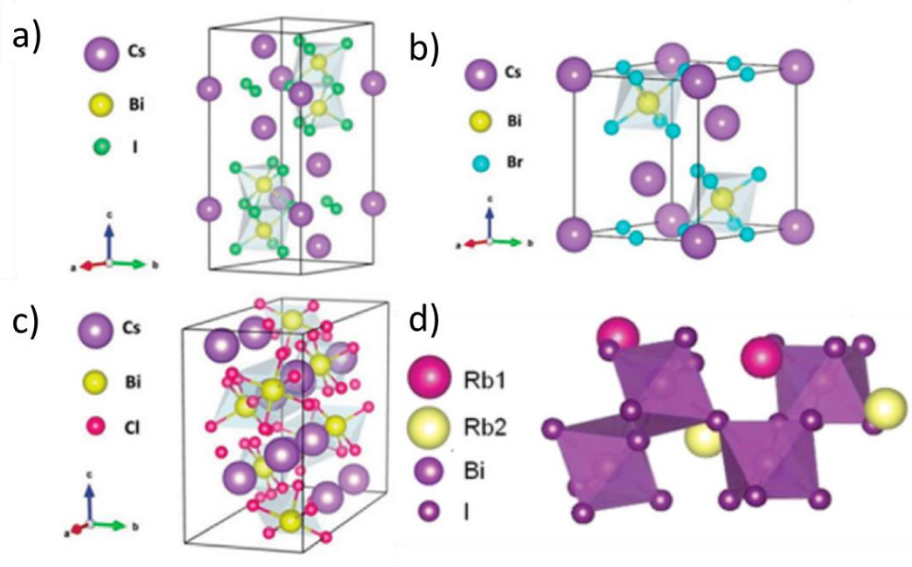

*Figure 13. Crystal structure of a) $P6_3/mmc$, b) $P\bar{3}m1$ space group, c) Pnma space group and d) P21/n space group. Adapted with permission from Catalysts, **12**,11 (2022)[98] under Creative Common CC BY License Copyright 2022 and John Wiley & Sons. **30**, 24 (2019)[99] Copyright 2019 John Wiley & Sons.*

2.3.4 Effect of composition on electronic structure and bandgap

The structural dimensionality and the electronic dimensionality of perovskites are interrelated parameters that influences the material's properties. The former refers to the physical arrangement of atoms and ions within the crystal lattice, while the latter refers to the degree of freedom that charge carriers have within the perovskite structure[100].

A key parameter that determines PV efficiency is carrier mobility (μ), and one of the intrinsic factors affecting carrier mobility is the carrier effective mass (m^*) as given in the Drude model:

$$\mu = \frac{q\tau}{m^*} \qquad (30)$$

Where q = fundamental charge and τ = momentum relaxation time[101]. This model is applicable for scenarios where there is no scattering by extrinsic factors and shows an inverse correlation between carrier mobility and effective mass of carriers. Effective masses are affected by band curvature[102, 103], which is strongly affected by structural dimensionality as it influences the arrangement of atomic orbitals and hence degree of band dispersion. LHPs and Sn- and Ge-based perovskites demonstrate low effective mass with high carrier mobilities due to disperse bands[104]. Charge movement in 2D LHPs and Sn- and Ge-based perovskites are restricted between layers due to the band dispersion between layers being lower than within the planes of the inorganic layers[100, 105].

0D Bi- and Sb- based $A_3B_2X_9$ compounds have flat bands and hence high effective masses and low carrier mobilities due to the crystal structure being isolated $[B_2X_9]^{3-}$ groups that alternate with the A-site cations. The 2D layered phases of $A_3B_2I_9$ compounds have lower effective masses and higher mobilities along the covalently bonded directions, and smaller and more direct bandgaps have been reported for 2D polymorphs of the same composition[87]. However, pure 2D compounds with no 0D polymorphs tend to have a much larger bandgap due to the 2D compounds being composed of lighter elements such as bromide and chloride having reduced covalent character and a smaller lattice constant

which results in a larger bandgap. For example, 2D $Cs_3Bi_2Br_9$ has a bandgap of 2.7 eV[106] compared to $Cs_3Bi_2I_9$ which has a bandgap of ~1.9 eV[107].

Vacancy-ordered triple perovskites exhibit bandgap bowing behaviour when the halide or the pnictogen species is mixed. *Yu et al.* [108]have reported an indirect bandgap of 1.85 eV and an optical (direct) bandgap of 2.23 eV for $Cs_3Bi_2I_9$ can be lowered to 1.75 eV and 2.05 eV, respectively for a $Cs_3Bi_2I_6Br_3$ film. Using first principles calculations, *Yu et al.* also reported that for $Cs_3Bi_2I_9$ ($P6_3/mmc$), the narrowest direct band gap is 2.43 eV located at Γ, while for $Cs_3Bi_2Br_9$ ($P\bar{3}m$) it is 2.71 eV, also located at Γ. According to their experimental results, the phase transition from $P6_3/mmc$ to $P\bar{3}m$ occurred when the Br/I reached 3/6. They also found that the vacancy-ordered triple perovskite produced broad PL emission peaks that are characteristic of phonon scattering along with surface recombination.

Hodgkins et al.[85] had similarly investigated $Cs_3Bi_2Br_{9-x}I_x$ and found that pure phased compounds for the bromide-iodide mixed compounds could not be made past a stoichiometry of $Cs_3Bi_2I_6Br_3$. They suggest there is a segregation of the bromide and iodide anions within the mixed phases, due to the iodide ions localising towards the sites on the top and bottom of the layer close to the Bi vacancy to alleviate the strain of size mismatch (Figure 14).

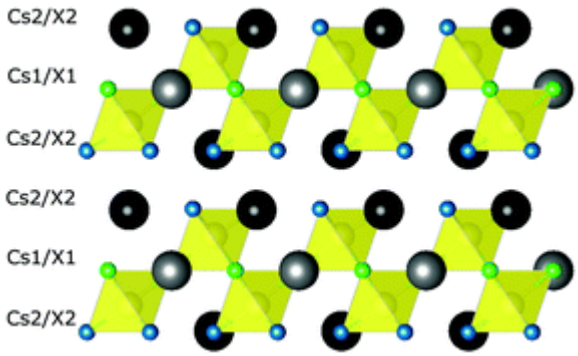

*Figure 14. View of the $Cs_3Bi_2Br_9$ structure. Substituting iodide for bromide shows a clear preference for the X2 site over the X1. Image is reproduced with permission from Chem. Commun., **55**, 3164-3167 (2019).* [85] *Copyright 2019 Royal Society of Chemistry.*

The effect of the pnictogen species on vacancy-ordered triple perovskites were studied by Shi *et al.*[109] bandgap bowing also occurs with the introduction of Sb (Figure 15). They propose that sub-bandgap energy levels may form in the bandgap for Cs_3SbBiI_9 due to energy mismatch between Sb and Bi atomic

orbitals. They also found that Cs_3SbBiI_9 have a significantly enhanced PL emission intensity of nearly two orders of magnitude relative to the $Cs_3Bi_2I_9$ and $Cs_3Sb_2I_9$, suggesting a reduction in trap density. However, multiple emission peaks at long wavelengths indicate the recombination of the self-trapped excitons and the excitons localized at sub-bandgap states.

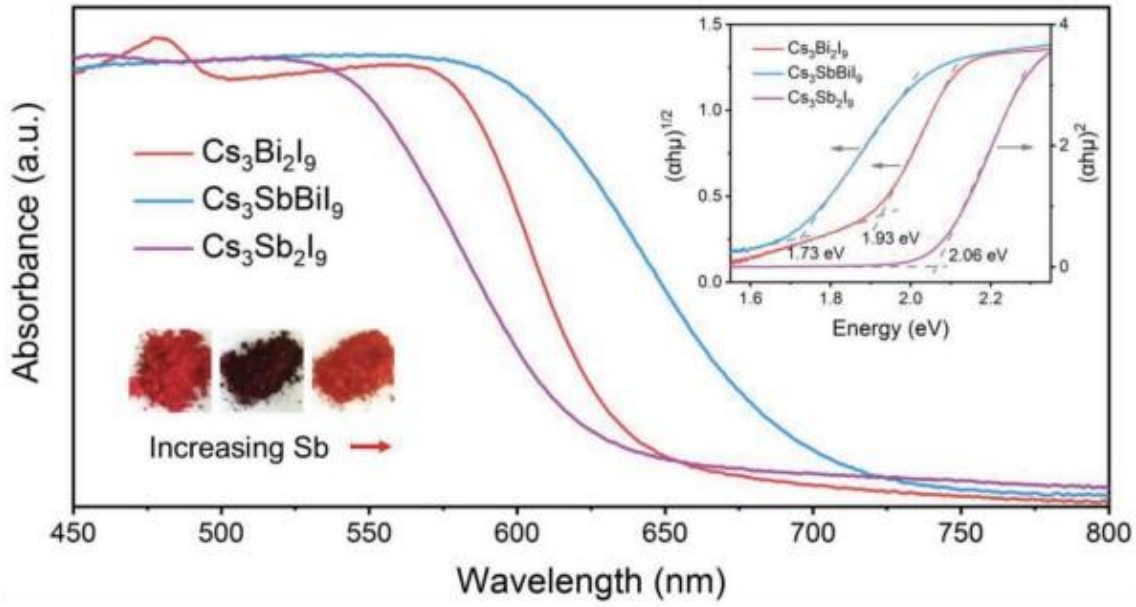

*Figure 15. UV–vis spectra and corresponding Tauc plot of $Cs_3Bi_2I_9$, Cs_3SbBiI_9, and $Cs_3Sb_2I_9$. Reproduced with permission from Small Methods, John Wiley and Sons, **8**,2 (2023)[109] Copyright 2023 John Wiley & Sons.*

Geng et al. found that the bandgap of 2D $Cs_3Sb_2I_9$ nanocrystals (NCs) could also be manipulated by applying pressure to the NCs[110]. They were able to synthesize $Cs_3Sb_2I_9$ NCs that had a band gap of 2.06 eV under ambient conditions but could be lowered to 1.36eV when the NC undergoes compression. They proposed that this is due to the Sb–I bond contraction from the pressure promoting orbital overlap as well as the altering of energy levels from pushing up the valence band and dropping the conduction band.

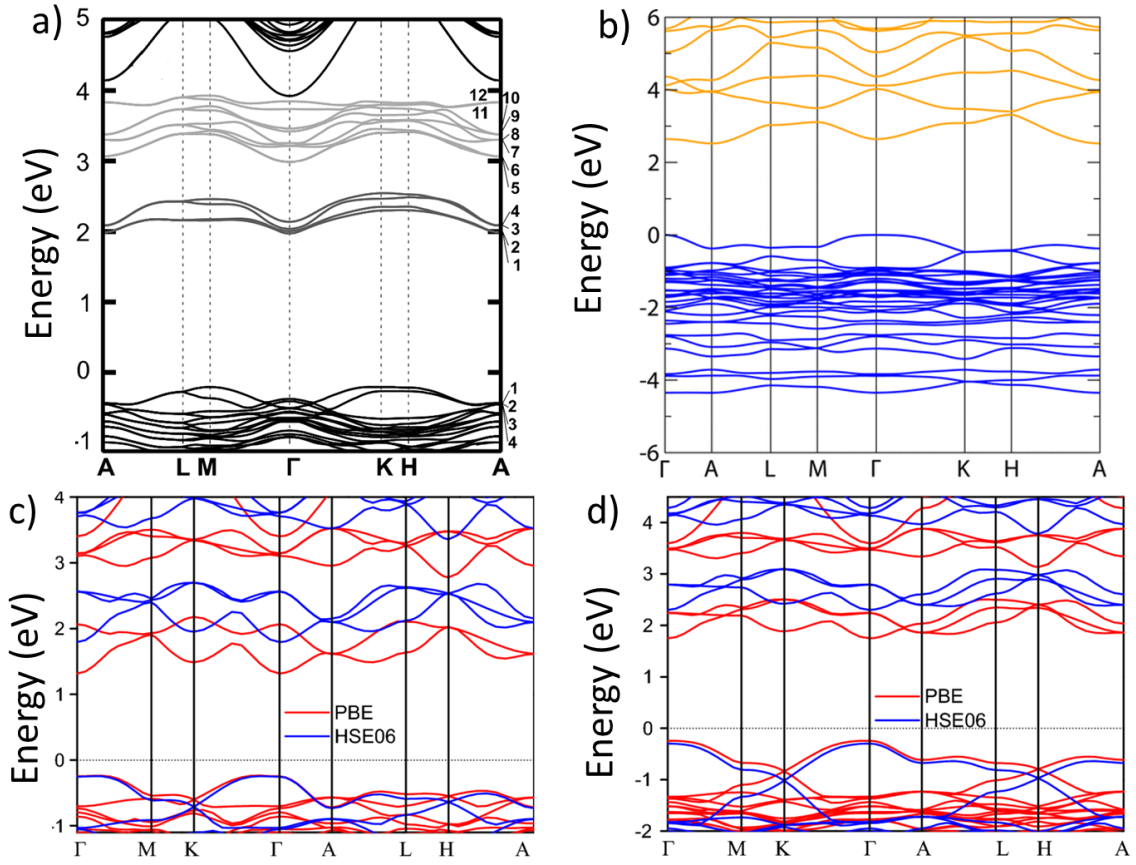

*Figure 16. DFT calculated band structure of a) $Cs_3Bi_2I_9$ b) $Cs_3Bi_2Br_9$ c) $Cs_3Sb_2I_9$ and d) $Cs_3Sb_2Br_9$. Reproduced with permission from Bass, K.K., et al., Inorganic chemistry **56**,1 (2017), Copyright 2017 American Chemical Society. From Physical Review B, 100(20), (2019) Copyright (2019) by the American Physical Society. And from Journal of Materials Science 2018 54:6, 2018-11-27. 54(6). Copyright © 2018, Springer Science Business Media.* [111-113]

The band structures of vacancy-ordered triple perovskites have been calculated via density functional theory (DFT) as shown in Figure 16. A point of interest are the narrow sub-bands which may produce sharp absorption peaks that are similar to excitonic absorption under UV-Vis spectroscopy.

2.3.5 Exciton binding energy of vacancy-ordered triple perovskites

The excitonic behaviour of vacancy-ordered triple perovskites is an important area to study as it significantly impacts the photocurrent and hence the PV performance of a photovoltaic device. Excitons are a result of band-edge excitations and are Coulombically bound electron–hole pairs with a neutral charge that need to be dissociated into free carriers in order to extract the electrons and holes. There are two types of excitons: Wannier–Mott excitons and Frenkel excitons. Wannier-Mott excitons are also

known as free excitons, have a low E_b, and are able to move in the crystal. Frenkel excitons are confined within a unit cell and have a high E_b of ~100 - 1000 meV[114].

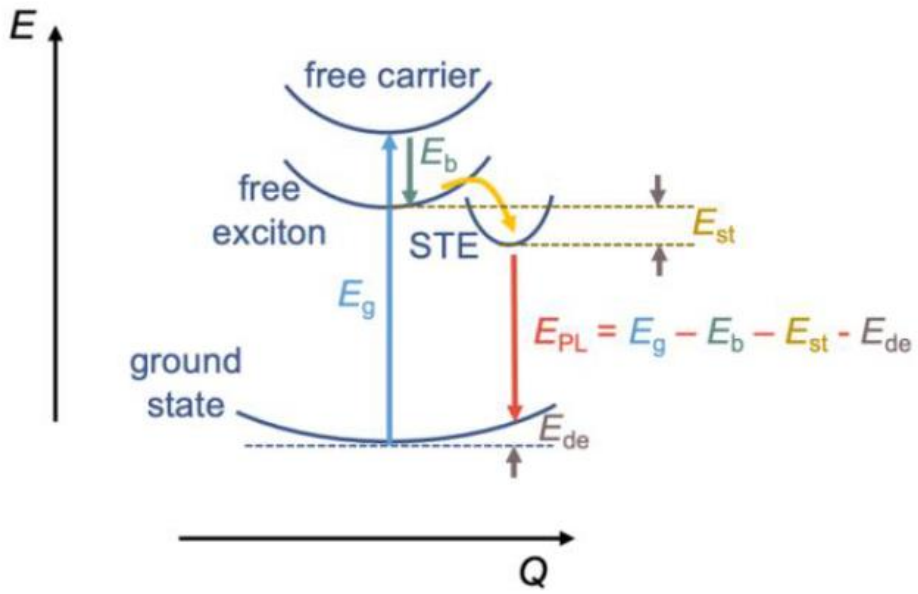

Figure 17. Configuration coordinate diagram showing the formation of excitons and self-trapped excitons (STE), and the energy changes involved. (STE, self-trapped exciton state; Eg, bandgap energy; E_b, exciton binding energy; E_{st}, self-trapping energy; E_{de}, lattice deformation energy; E_{PL}, emission energy). Reproduced with permission under Creative Common CC BY License from Applied Physics Letters, AIP Publishing, ***119****,22, (2021).* [31] *Copyright 2021.*

The exciton binding energy (E_b), which is the difference between the energy of the excitonic state and the electronic band gap of the material as shown in Figure 17 is a critical parameter than determines the dissociation and hence transport properties of the material. It can be estimated from the hydrogenic formula as shown in Equation 31:

$$E_b = \frac{\mu}{n^2 {\varepsilon_r}^2} R_H \qquad (31)$$

Where n is the principal quantum number (i.e., 1st excitonic level, 2nd excitonic level, etc.), $\varepsilon_r$is the effective dielectric constant, R_H is the hydrogen Rydberg constant (13.6 eV), and μ is the effective reduced mass of the exciton given by Equation 27:

$$\frac{1}{\mu} = \frac{1}{m_h} + \frac{1}{m_e} \qquad (32)$$

Where m_h is the hole effective mass relative to the free electron mass m_0 and m_e is the electron effective mass relative to the free electron mass m_0.

When E_b is smaller or equal to kT, as is the case in 3D lead-halide perovskites[115-117], the exciton could be readily dissociated to free carriers through thermal energy. When E_b is high, a driving force is needed for exciton dissociation. According to the Saha equation, a thermal equilibrium is established between the photoexcited bound excitons and the unbound electron hole plasma (Equation 33):

$$\frac{{n_{e,h}}^2}{n_{EX}} = (\frac{2\pi\mu k_B T}{h^2})^{\frac{3}{2}} e^{\frac{-E_b}{k_B T}} \quad (33)$$

Where $n_{e,h}$ is the density of unbound electron-hole plasma, n_{EX} is the density of photoexcited bound excitons, μ is the exciton effective reduced mass, E_b is binding energy of the excitons, k_B is the Boltzmann constant, and h is the Planck constant.

Research has shown that both Bi- and Sb- based vacancy-ordered triple perovskites have high exciton binding energies and hence is a factor in limiting their performance to well below their radiative limits[118-120]. Correa-Baena *et al.*[71]extracted the exciton binding energy of $A_3Sb_2I_9$ (A = Cs, Rb, and K), by fitting the thermal quenching of excitonic emission:

$$I(T) = \frac{I_0}{1 + A\, e^{\frac{-E_b}{k_B T}}} \quad (34)$$

Where $I(T)$ is the intensity from the PL data, I_0 and A are constants, and E_B is the exciton binding energy. They reported exciton binding energies of 184 ± 46, 95 ± 5, and 137 ± 24 meV for the $Cs_3Sb_2I_9$ (0D), $Rb_3Sb_2I_9$ (2D), and $K_3Sb_2I_9$ (2D) respectively.

Rieger *et al.*[112] calculated a theoretical and experimental exciton binding energy of ~230 meV and 295 meV for $Cs_3Bi_2I_9$ respectively. Similarly, an exciton binding energy of ~290 meV have been calculated via DFT for $Cs_3Bi_2Br_9$ by Wang *et al.*[121]. Interestingly, there is some conflict in literature regarding the exciton binding energy for $Cs_3Sb_2Br_9$: it has been reported to be as high as ~ 530 – 580 meV[122] by some and as low as ~200 meV[123] by others, all obtained from PL data calculations. These values are much higher than the lead-halide perovskite exciton binding energy which have been reported to be range from 2 meV to 50 meV[124].

2.3.6 Carrier-phonon coupling in lead-halide and vacancy-ordered perovskites

Both lead-halide perovskites and vacancy-ordered perovskites are polar materials containing heavy elements. This gives rise to Fröhlich interactions, as described previously in section 2.1.3. due to the differences between ε_∞ and ε_0. $MAPbI_3$, for example, has a limited carrier mobility of ~200 $cm^2\ V^{-1}\ s^{-1}$ due to Fröhlich coupling producing polarons with nanometre long radii[125].

Self-trapping may also occur in these materials. However, this is dependent on the dimensionality of the system. Self-trapping occurs less easily in 3D materials due to an energy barrier between localised and free carriers[126]:

$$W \sim \frac{\omega^4}{\mu^3 \gamma^4} \qquad (35)$$

Where μ is the reduced effective mass of the exciton, γ is the exciton–phonon coupling constant, and ω is the characteristic frequency of the optical phonons. Hence, in 3D structures, free and self-trapped excitons can co-exist. For 2D materials, self-trapping is dependent on the coupling constant g_{ac}, where high g_{ac} enables self-trapping for acoustic phonons. As high deformation potential leads to high g_{ac}, self-trapping is more prevalent in soft materials.

For lead-halide perovskites, both experimental and theoretical evidence suggest that Fröhlich interactions is the most significant factor limiting carrier mobility[100, 125, 127-129]. First principles calculations have suggested that acoustic-phonon deformation potential scattering is too weak for $MAPbI_3$ to lower carrier mobility further[129]. Meanwhile, $MAPbBr_3$ has a lower carrier mobility than $MAPbI_3$, which could be attributed to $MAPbBr_3$ having stronger Fröhlich interactions due to the higher ionicity of the Pb-Br bond compared to the Pb-I bond[130].

Carrier-phonon coupling interactions have also been studied in PIMs, such as $Cs_2AgBiBr_6$. Early works found Fröhlich interactions do be dominant[31, 131-133]. Temperature-dependent pulse-radiolysis time-resolved microwave conductance (PRTRMC) measurements by Bartesaghi *et al.*[134] showed an increase in carrier as temperature decreases, which is consistent with reduced phonon scattering. Measurements of the carrier scattering time exhibited a $T^{-0.5}$ dependence, which is typical for large polaron-dominated transport[131]. However, despite a similar Fröhlich coupling constant α_{op}

obtained for both $Cs_2AgBiBr_6$ and $MAPbI_3$[28, 130, 135], $Cs_2AgBiBr_6$ has a more limited carrier mobility of only 11.81 $cm^2\ V^{-1}\ s^{-1}$[136]. This suggests that carrier–phonon coupling is not limited to Fröhlich coupling in $Cs_2AgBiBr_6$. Calculations by Wu *et al.* reported the deformation potentials of $Cs_2AgBiBr_6$ to be 13.7 and 14.7 eV in the valence and conduction band extrema, respectively, which is larger than those of $CsPbBr_3$ (2.2 and 6.3 eV for the valence and conduction band extrema, respectively), which would lead to a larger acoustic coupling constant[137]. Transient reflectance spectroscopy has shown an initial ultrafast drop in the density of excited-state carriers, followed by a much slower decay[137, 138], which has been suggested as evidence of hot carriers thermalizing via LO phonons on a sub-picosecond timescale before coupling to acoustic phonons on a <10 ps timescale and then interacting with defects on longer timescales[137].

2.3.7 Silver bismuth halides

Compounds within the AgI–BiI_3 phase space have also come into focus as a lead-free alternative to perovskites. They have a calculated SLME exceeding 20%[2] for conventional outdoor light harvesting and exceeding 50% for indoor light harvesting [2, 11]. In 2016, Turkevych *et al.* reported a 4.3% PCE [139] and Kim *et al.* reported a 1.22% PCE [140], so there is still much room for improvement. The Ag-Bi-I compounds also exhibit tuneable structural and optoelectronic properties through compositional engineering[141]. While Cu-Bi-I is a similar compound that is less expensive and avoids the toxicity to aquatic life of Ag-compounds, they have been reported to be less stable[142, 143]. And although study has found that mixing Cu and Ag together could form quaternary compounds that retain the stability of Ag-based compounds while reducing the quantity Ag[144-147], these materials are still in the preliminary stages of development, and many relationships between their structures and properties remain unclear.

2.3.7.1. Crystal structure and bulk properties

The stoichiometry of Ag-Bi-I affects the crystal structure of the resulting compound. Bi-rich compounds such as $AgBi_2I_7$ and $Ag_2Bi_3I_{11}$ have been reported to adopt a 3D defect-spinel structure ($Fd\bar{3}m$) while Ag-rich compounds such as Ag_2BiI_5 and Ag_3BiI_6 have a 3D rhombohedral $NaVO_2$-type structure ($R\bar{3}m$)[145, 148-151]. $AgBiI_4$ have been reported to adopt both the 3D defect-spinel structure and a 2D $CdCl_2$-type structure ($R\bar{3}m$)[141, 148, 152]. As shown in Figure 18 all Ag-Bi-I compounds have a cubic

close-packed (ccp) iodide sub-lattice with two tetrahedral holes and one octahedral hole per anion. Both Ag^+ and Bi^+ occupy the octahedral holes in the lattice due to their very similar ionic radii of 129 pm and 117 pm respectively[153]. In $AgBiI_4$, the probability for an octahedral hole to be occupied by Ag^+ or Bi^3 is the same, but as stoichiometry changes, vacancies also occupy these holes in order to maintain charge neutrality[148, 154]

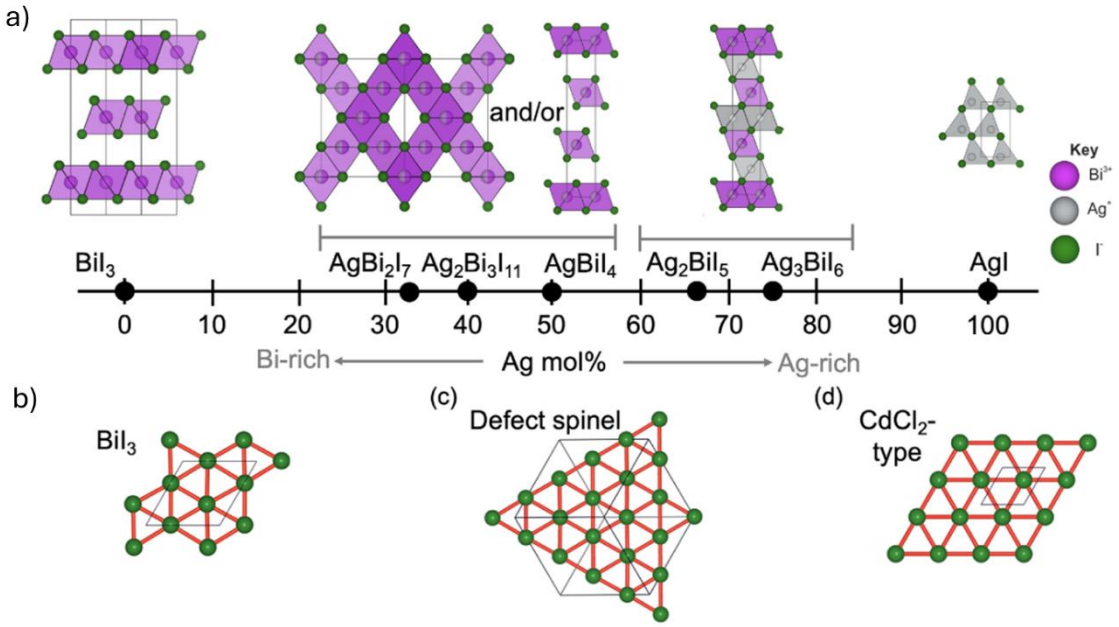

Figure 18. (a) Influence of stoichiometry on the structure of $Ag_aBi_bI_{a+3b}$ compounds, Iodide sub-lattice of (b) BiI_3, (c) $AgBiI_4$ (defect-spinel structure), and (d) $AgBiI_4$ ($CdCl_2$-type structure). Crystal structure of compounds in the Ag-Bi-I family of compounds. Reproduced with permission from International Materials Reviews, 69(1), (2024).[141] Copyright © 2024, Sage Publications.

Buizza *et al.*[146] and Ghosh *et al.*[143] both determined the exciton binding energy (E_b) of Ag-Bi-I materials through Elliott model fitting of their optical absorption data. But while the former obtained an E_b of 27 meV for $AgBiI_4$ and came to the conclusion that most charge carriers are free, the latter obtained a drastically different value of 260 meV which implied that excitons are dominant. Therefore, the nature of charge carriers in Ag-Bi-I are for debate and require more investigation. Furthermore, there is strong carrier-phonon coupling present in Ag-Bi-I compounds leading to the wave function of the carrier being confined to a unit cell or smaller and severely limiting its mobility[141].

Different stoichiometry of Ag-Bi-I compounds also results in different types of defects. The Ag-rich compounds show p-type conductivity, implying the presence of acceptor-like point defects. Unreacted

AgI have been reported to accompany these compounds[148, 155, 156] and so Ag vacancies are a probable cause. Bi-rich compounds show n-type conductivity and as unreacted BiI_3 has been observed in these materials, iodide vacancies are likely to be the present.

Macroscopic structure defects such as grain boundaries and pinholes also exist in Ag-Bi-I thin films, limiting photovoltaic performance. Kulkarni *et al.* also reported the formation of voids at the interface of TiO_2 ETL when growing Ag_3BiI_6 thin films via solution processing with chlorobenzene antisolvent, which act as non-radiative recombination sites and hence limits electron extraction and device performance[156]. They found that removing the antisolvent eliminated the presence of the voids and posited that the chlorobenzene antisolvent removed excess DMSO solvent, especially at the bottom interface, which led to the formation of voids.

A difficulty in synthesizing Ag-Bi-I compounds is that AgI is insoluble in commonly used polar solvents for halide compound processing, such as dimethylformamide (DMF) and dimethyl sulfoxide (DMSO)[140, 148]. Turkevych *et al.* found that when DMSO is heated to 110 °C, the mixture of AgI and BiI_3 could be dissolved[148]. They attributed the AgI dissolution to the formations of $[BiI_{3+x}]^{x-}$ complex ions. Photovoltaic devices with 4.3% PCE were achieved with this method. Shao *et al.* added HCl to DMF at 70 °C to improve AgI dissolution and achieved dense films with large grains[157], but device performance for the $Ag_2Bi_3I_{11}$ they synthesized was poor at 0.78% due to low short-circuit current densities (2.30mA cm^{-2}). Similarly, Jung *et al.* added a small quantity of HI to a DMF/DMSO solution[158] to dissolve pre-synthesized Ag_2BiI_5 powder and achieved 2.31% PCE even though the films were unable to completely cover the substrate. Groups have also tried to use primary alkylamines instead of polar aprotic solvents to dissolve AgI. Both Kim *et al.*[140] and Zhu *et al.*[159] used n-butylamine and achieved 1.22% PCE and 2.1% PCE respectively.

As morphology has a significant impact on device performance, investigation into improving Ag-Bi-I thin film morphology has been made. Anti-solvent dripping, which uses solvent with poor solubility for the precursors is used to wash away the original solvent during thin film spinning, is an often-used approach to improve lead-halide perovskite morphology and hence also investigated for Ag-Bi-I. This method induces rapid supersaturation and the formation of high density of nuclei, and hence reduces the number of pinholes in the resulting thin film. Because the precursors are polar compounds,

antisolvents with dielectric constants below 20 (toluene, chlorobenzene and isopropanol) were considered. Zhai *et al.*[160] compared toluene, chlorobenzene and isopropanol and reported isopropanol as the antisolvent that produced $AgBiI_4$ thin films with the lowest pinhole density. Although PCE of $AgBiI_4$ solar cells increased from 0.64% to 1.26% using this method, it still failed to reach that as reported by Turkevych *et al.* for Ag_3BiI_6 using a toluene antisolvent, which was 4.3%[148].

Hot casting is another approach that could be used to improve morphology. In this method, both the precursor solution and substrate to be pre-heated before spin coating to enhance evaporation rate of the solvent and induce supersaturation. For example, Ghosh *et al.*[143] combined hot casting with antisolvent dripping and increased their $AgBiI_4$ device PCE from 1.2% to 2.2%. However, hot casting conditions are difficult to consistently reproduce in the lab as the temperature of the solution and substrate cannot be measured during spin coating, and the time it takes for solution to be deposited after both it and substrate are removed from heat source may vary due to human error.

2.3.7.2 Photovoltaic development of Ag-Bi-I

Many groups have investigated the potential Ag-Bi-I compounds as standard outdoor solar cells since 2016, as shown in Table 1. Currently, the best PCE achieved was 4.38% by Pai *et al.*[161] with $Ag_3Bi_2I_6$ in 2019. Adding S additives to $Ag_3Bi_2I_6$ could further increase this to 5.56% [161] due to a lower bandgap. SLMEs for $AgBiI_4$ and Ag_2BiI_5 under one sun illumination were found to be 26% and 24% respectively[2].

Table 1. Photovoltaic performance of Ag-Bi-I absorbers. The average values and uncertainties for each performance parameter, along with the performance of the champion device, are shown where available.

Year	Composition	Fabrication method	Device structure	Max PCE (%)	Mean PCE (%)	Max V_{oc} (V)	Max J_{sc} (mA cm^{-2})	Max FF	Mean FF	Ref.
2016	Ag_3BiI_6	SPC-HC:DMO, 110 °C	FTO/c-m-TiO_2/RDF/PTAA/Au	4.3	-	0.63	10.7	0.64	-	[148]
2016	$AgBi_2I_7$	SPC:BA, 25 °C	FTO/c-m-TiO_2/RDF/P3HT/Au	1.22	1.09 ± 0.07	0.56	3.3	0.67	0.65 ± 0.03	[140]
2017	Ag_3BiI_6	SPC-HC:DMSO, 80 °C	FTO/c-m-TiO_2/RDF/sp:LiTFSI-[Co]-TBP-ACN/Au	1.08	0.91	0.65	2.36	0.7	0.75	[162]

2017	Ag_3BiI_6	SPC-HC:DMSO, 80 °C	FTP/NiO/RDF/PCBM-BCP/Ag	0.32	0.14	0.41	1.29	0.59	0.42	[162]
2017	Ag_2BiI_5	SPC:BA, 25 °C	FTO/c-m-TiO_2/RDF/P3HT/Au	2.1	1.5	0.49	6.8	0.63	-	[159]
2017	$AgBiI_4$	SPC:BA, 25 °C	FTO/c-m-TiO_2/RDF/P3HT/Au	0.4	-	0.46	1.6	0.56	-	[159]
2018	$AgBiI_4$	SPC:DMF:DMSO, 25 °C +AST:CB	FTO/c-m-TiO_2/RDF/PTAA/Au	1.2	-	0.63	3.7	0.51	-	[143]
2018	Ag_2BiI_5	SPC:DMF:DMSO, 25 °C +AST:CB	FTO/c-m-TiO_2/RDF/PTAA/Au	1.6	-	0.63	4.42	0.58	-	[143]
2018	$AgBiI_4$	SPC:DMF:DMSO, 100 °C +AST:CB	FTO/c-m-TiO_2/RDF/PTAA/Au	2.2	-	0.67	5.24	0.62	-	[143]
2018	Ag_2BiI_5	SPC:DMF:DMSO, 100 °C +AST:CB	FTO/c-m-TiO_2/RDF/PTAA/Au	2.6	-	0.69	6.04	0.62	-	[143]
2018	$Ag_3Bi_2I_9$	SPC:DMF:DMSO:HI, 25 °C + AST:Ether	FTO/c-m-TiO_2/RDF/sp/Au	2.04	-	0.6	5.64	0.61	-	[158]
2018	$Ag_{11}Bi_9I_{38}$	SPC:DMF:DMSO:HI, 25 °C + AST:Ether	FTO/c-m-TiO_2/RDF/sp/Au	2.31	-	0.61	6.33	0.59	-	[158]
2018	Ag_2BiI_5	SPC:DMF:DMSO:HI, 25 °C + AST:Ether	FTO/c-m-TiO_2/RDF/sp/Au	1.74	-	0.59	4.9	0.6	-	[158]
2018	$AgBiI_4$	SPC:DMF:DMSO:HI, 25 °C + AST:Ether	FTO/c-m-TiO_2/RDF/sp/Au	1.91	-	0.59	5.59	0.58	-	[158]
2018	$AgBiI_4$	SPC:DMF:DMSO:HI, 25 °C + AST:MB	FTO/c-m-TiO_2/RDF/PTAA/Ag	2.1	2.1 ± 0.4	0.53	7.63	0.52	-	[163]
2018	$AgBiI_4$	SPC:DMF:DMSO:HI, 25 °C + AST:MB	FTO/c-m-TiO_2/RDF/PTAA/Ag	0.53	-	0.45	2.68	0.44	-	[163]
2018	$AgBiI_4$	SPC-HC:DMF:HCl, 70 °C	FTO/c-SnO_2/m-TiO_2/RDF/sp:LiTFSI-[Co]-TBP-ACN/Au	0.47	0.41	0.62	1.82	0.41	0.45	[157]
2018	$Ag_4Bi_5I_{19}$	SPC-HC:DMF:HCl, 70 °C	FTO/c-SnO_2/m-TiO_2/RDF/sp:LiTFSI-[Co]-TBP-ACN/Au	0.47	0.42	0.66	1.51	0.47	0.41	[157]

2018	$Ag_2Bi_3I_{11}$	SPC-HC:DMF:HCl, 70 °C	FTO/c-SnO_2/m-TiO_2/RDF/sp:LiTFSI-[Co]-TBP-ACN/Au	0.5	0.4	0.71	1.69	0.41	0.41	[157]
2018	$Ag_2Bi_3I_{11}$	SPC-HC:DMF:HCl, 70 °C	FTO/c-SnO_2/m-TiO_2/RDF/sp:LiTFSI-[Co]-TBP-ACN/Au	0.78	0.67	0.72	2.39	0.46	0.4	[157]
2018	$Ag_4Bi_7I_{25}$	SPC-HC:DMF:HCl, 70 °C	FTO/c-SnO_2/m-TiO_2/RDF/sp:LiTFSI-[Co]-TBP-ACN/Au	0.66	0.6	0.71	2.57	0.36	0.46	[157]
2018	$AgBi_2I_7$	SPC-HC:DMF:HCl, 70 °C	FTO/c-SnO_2/m-TiO_2/RDF/sp:LiTFSI-[Co]-TBP-ACN/Au	0.61	0.52	0.65	2.51	0.38	0.33	[157]
2018	$Ag_4Bi_9I_{31}$	SPC-HC:DMF:HCl, 70 °C	FTO/c-SnO_2/m-TiO_2/RDF/sp:LiTFSI-[Co]-TBP-ACN/Au	0.66	0.56	0.66	2.6	0.38	0.38	[157]
2018	$AgBi_2I_7$	SPC-HC:DMF:HCl, 50 °C	FTO/c-SnO_2/m-TiO_2/RDF/sp:LiTFSI-[Co]-TBP-ACN/Au	0.83	0.67	0.69	2.76	0.44	0.43	[164]
2018	$AgBi_2I_7$	SPC-HC:DMF:HCl, 50 °C	FTO/c-SnO_2/m-TiO_2/RDF/sp:LiTFSI-[Co]-TBP-ACN/Au	0.55	0.37	0.69	1.76	0.45	0.46	[164]
2019	Ag_3BiI_6	SPC:DMF:DMSO:HI, 25 °C	FTO/c-m-TiO_2/RDF/PTAA/Au	4.38	4.33 ± 0.05	0.61	11.20	0.65	0.64	[161]
2019	Ag_2BiI_5	SPC:DMF:DMSO:HI, 25 °C	FTO/c-m-TiO_2/RDF/PTAA/Au	3.16	3.11 ± 0.03	0.52	8.90	0.68	0.68	[161]
2019	$AgBiI_4$	SPC:DMF:DMSO:HI, 25 °C	FTO/c-m-TiO_2/RDF/PTAA/Au	2.36	2.33 ± 0.02	0.56	8.07	0.52	0.52	[161]
2019	$AgBi_2I_7$	SPC:DMF:DMSO:HI, 25 °C	FTO/c-m-TiO_2/RDF/PTAA/Au	2.09	2.06 ± 0.03	0.60	5.80	0.60	0.60	[161]
2019	$AgBi_2I_7$	SPC:DMSO, 25 °C + AST:CB	FTO/c-m-TiO_2/RDF/P3HT/Au	2.12	-	0.62	4.83	0.70	-	[165]
2019	$AgBi_2I_7$	SPC:BA, 25 °C + AST:CB	FTO/c-m-TiO_2/RDF/P3HT/Au	0.33	-	0.52	1.45	0.43	-	[165]
2019	$AgBiI_4$	SPC:DMF:DMSO, 25 °C+ AST:CB	FTO/c-SnO_2/RDF:LiTFSI/PTAA/Au	2.8	-	0.83	5.07	0.67	-	[166]
2019	$AgBiI_4$	SPC:DMF:DMSO,	TO/c-SnO_2/RDF:Ag	0.67	-	0.83	2.13	0.38	-	[166]

		25 °C+AST:CB	TFSI/PTAA/Au							
2019	$AgBiI_4$	SPC:DMF:DMSO, 25 °C+AST:CB	TO/c-SnO_2/RDF:TFSI/PTAA/Au	0.7	-	0.81	2.55	0.34	-	[166]
2019	$AgBiI_4$	SPC:DMF:DMSO, 25 °C+AST:CB	TO/c-SnO_2/RDF:LiI/PTAA/Au	1.26	-	0.6	6.05	0.35	-	[166]
2019	$AgBiI_4$	SPC:DMF:DMSO, 25 °C+AST:CB	TO/c-SnO_2/RDF/PTAA/Au	1.61	-	0.66	4.26	0.59	-	[166]
2020	$Ag_3Bi_2I_9$	SPC:DMSO, 25 °C+AST:TL	FTO/c-m-TiO_2/[0.5$Cs_3Bi_2I_9$-RDF]/BHJ/PDBD-T/Au	3.59	2.73 ± 0.30	0.78	7.65	0.6	0.54 ± 0.02	[167]
2020	$Ag_3Bi_2I_9$	SPC:DMSO, 25 °C+AST:TL	FTO/c-m-TiO_2/RDF/PDBD-T/Au	1.97	1.01 ± 0.32	0.7	4.9	0.58	0.51 ± 0.06	[167]
2020	Ag_3BiI_6	SPC:BA, 25 °C	ITO/NiO/RDF/PCBM:C_{60}/Au	0.16	0.06 ± 0.01	0.77	0.62	0.33	0.25 ± 0.03	[168]
2020	Ag_3BiI_6	SPC:BA, 25 °C	ITO/NiO/RDF/PCBM:C_{60}/Au	1.08	0.80 ± 0.16	0.82	1.73	0.76	0.62 ± 0.07	[168]
2020	$AgBi_2I_7$	SPC:DMF:DMSO, 25 °C	FTO/c-m-TiO_2/RDF/PTB7/MoO_3/Au	0.31	-	0.67	0.91	0.51	-	[169]
2020	$AgBiI_4$	SPC:DMF:DMSO, 25 °C	FTO/c-m-TiO_2/RDF/PTAA/Ag	1.05	0.95± 0.07	-	-	-	0.49	[170]
2020	Ag_2BiI_5	SPC:DMF:DMSO:HI, 25 °C	FTO/c-m-TiO_2/RDF/sp/Au	0.44	-	0.42	3.5	0.3	-	[171]
2020	Ag_2BiI_5	SPC:DMF:DMSO:HI, 25 °C	FTO/c-m-TiO2/[RDF:MWCNT]BHJ/sp/Au	1.61	-	0.62	5	0.52	-	[171]
2020	Ag_2BiI_5	SPC:DMF:DMSO:HI, 25 °C	FTO/c-m-TiO2/[RDF:RGO]BHJ/sp/Au	1.32	-	0.53	4.4	0.57	-	[171]
2020	Ag_3BiI_6	SPUT:Cu:Bi+$I_{2(V)}$, 150 °C, 60 min	FTO/c-TiO_2/RDF/NiO/Au	0.08	0.05 ± 0.01	0.65	0.36	0.33	0.35 ± 0.02	[172]
2020	$AgBi_3I_{10}$	IM3L:BA, , 25 °C	FTO/c-[m-TiO_2/m-Al_2O_3/m-NiO/Carbon-RDF]BH	2.73	2.56±0.25	0.68	6.68	0.6	-	[173]
2021	Ag_2BiI_5	SPC:DMF:DMSO, 25 °C + AST:EatEt	FTO/c-m-TiO_2/RDF/PTAA/Ag	2.04	-	0.6	6.04	0.56	-	[174]
2021	Ag_2BiI_5	SPC:DMF:DMSO, Ba + Cs_2	ITO/SnO_2/RDF/PTAA/Ag	0.38	-	0.68	1.21	45.97	-	[175]

2022	$AgBiI_4$	SPC-HC:DMF:DMSO, 100 °C	ITO/c-SnO_2/RDF/PTAA/Au	0.82	0.64 ±0.16	-	-	-	0.50 ± 0.07	[160]
2022	$AgBiI_4$	SPC-HC:DMF:DMSO, 100 °C +AST:CB	ITO/c-SnO_2/RDF/PTAA/Au	-	0.94 ±0.25	-	-	-	0.52 ± 0.09	[160]
2022	$AgBiI_4$	SPC-HC:DMF:DMSO, 100 °C +AST:TL	ITO/c-SnO_2/RDF/PTAA/Au	-	1.11 ±0.14	-	-	-	0.58 ± 0.06	[160]
2022	$AgBiI_4$	SPC-HC:DMF:DMSO, 100 °C +AST:IPA	ITO/c-SnO_2/RDF/PTAA/Au	1.61	1.26 ±0.14	-	-	-	0.56 ± 0.06	[160]
2022	$Ag_3Bi_{0.9}I_{5.7}$	SPC:DMSO, 25 °C + AST:CB	FTO/c-m-TiO_2:Sn/RDF/PTAA: LiTFSI-ACN/Ag	-	1.85 ± 0.13	-	-	-	0.69 ± 3.25	[176]
2022	Ag_3BiI_6	SPC:DMSO, 25 °C + AST:CB	FTO/c-m-TiO_2:Sn/RDF/PTAA: LiTFSI-ACN/Ag	2.1	1.98 ± 0.15	-	-	-	0.67± 3.55	[176]
2022	$Ag_3Bi_{1.1}I_{6.3}$	SPC:DMSO, 25 °C + AST:CB	FTO/c-m-TiO_2:Sn/RDF/PTAA: LiTFSI-ACN/Ag	2.60	2.36 ± 0.17	-	-	-	0.62± 3.37	[176]
2022	$Ag_3Bi_{1.3}I_{6.9}$	SPC:DMSO, 25 °C + AST:CB	FTO/c-m-TiO_2:Sn/RDF/PTAA: LiTFSI-ACN/Ag	-	2.01 ± 0.15	-	-	-	0.59± 4.87	[176]
2022	$Ag_3Bi_{1.5}I_{7.5}$	SPC:DMSO, 25 °C + AST:CB	FTO/c-m-TiO_2:Sn/RDF/PTAA: LiTFSI-ACN/Ag	-	1.39 ± 0.18	-	-	-	0.53 ± 6.99	[176]
2023	Ag_3BiI_6	TADB:DMSO, 120 °C	FTO/c-m-TiO_2/RDF/PTAA/Ag	2.06	-	0.62	5.56	0.59	-	[177]
2023	Ag_3BiI_6	TADB:DMSO, 120 °C	FTO/c-m-TiO_2:Sn/RDF/PTAA: LiTFSI/Ag	2.77	-	0.7	6.44	0.62	-	[177]

RDF: ternary and quaternary compounds in the AgI–BiI3phase space; SPC: spin coating; SPC-HC: spin coating with hot casting; AST: antisolvent treatment; SA: solvent annealing; TADB: thermal-assisted doctor blade coating; IM3L: infiltration into mesoscopic three-layer structure; SPUT: sputtering; I2(V): iodine vapor treatment; BHJ: bulk-heterojunction; c-m-TiO2: compact + mesoporous TiO2; DMSO: dimethylsolfoxide; DMF: N,N-dimethylformamide; BA: n-butylamine; CB: chlorobenzene; TL: toluene; IPA: isopropyl alcohol; MB: methylbenzene; EtEt: ethyl ether; Ether: a non-specified ether; TBP: 4-tert-butylpyridine; ACN: acetonitrile; LiTFSI: lithium bis(-trifluoromethanesulfonyl) imide; [Co]: cobalt(III) complex tris[2-((1H-pyrazol-1-yl)-4-tert-butylpyridine)cobalt(III)tris(bis(trifluoromethylsulfonyl)imide)]; sp: spiro-OMeTAD–2,2′,7,7′-tetrakis(N,N-di-p-methoxy phenylamino)-9,9-spirobifluorene; sp(TFSI)2: 2,2′,7,7′-tetrakis(N,N-di-p-methoxy phenylamino)-9,9-spirobifluorene bis(trifluoromethane) sulfonimide; PTAA: Poly[bis(4-phenyl)(24,6-trimethylphenyl) amine; P3HT: poly(3-hexylthiophene); PTB7: poly [[4,8-bis[(2-ethylhexyl)oxy]benzo[1,2-b:4,5-b']dithiophene-2,6-diyl][3-fluoro-2-[(2-ethylhexyl)carbonyl]thieno[3,4-b]thiophenediyl]]; PDBD-T: poly [(2,6-(4,8-bis (5-(2-ethylhexyl)thiophen-2-yl)-benzo [1,2-b:4,5-b']dithiophene))-alt-(5,5-(10,30-di-2-thienyl-50,70-bis(2-

ethylhexyl)benzo [10,20-c:40,50-c′] dithiophene-4,8-dione))]; PCBM: phenyl-C61-butyric acid methyl ester; BCP: bathocuproine

Many stability tests have been conducted on Ag-Bi-I devices in ambient air, ranging from 10[140] to 77 days[178]. These devices were stored in a designated testing environment and measured performance under 1 sun illumination at regular time intervals. A decrease of 5%-15% in PCE was reported from these tests. Lu *et al*.[163] observed $AgBiI_4$ to be photovoltaically stable than lead-halide perovskites: when the films exposed to 1 sun illumination under an inert gas environment for up to 3 h, $AgBiI_4$ showed no phase degradation, whereas the lead-halide perovskite formed a PbI_2 impurity peak after 1 h. However, Zhang *et al*.[179] observed that the PCE of their Ag-Bi-I device decreased by approximately 40% under continuous operation for 50 s, even though only a <5% decrease was observed when repeated measurements (non-continuous operation) were made over a period of 500 h in air. They suggested that the drastic loss in PCE may be due to heat, ion migration or changes to the device at the interfaces during operation.

Table 2. Performance of Ag–Bi–I and Cu–Ag–Bi–I IPVs compared with LHP IPVs. The light source used in these reports was WLED. Please note that not all devices were measured under the same illumination conditions, and the standards for indoor photovoltaic measurements had not been published when these reports were made.

Year	Compound	Device structure	Illuminance (lux)	P_{out} (μW cm^{-2})	PCE (%)	Max V_{oc} (V)	Max J_{sc} (mA cm^{-2})	FF (%)	Ref.
2021	LHP (triple cation)	FTO/TiO_2/LHP/Lycopene/spiro-OMeTAD/MoO_x/Ag	1000	111.7	40.2	0.85	248	53	[180]
2023	LHP ($CsPbI_3$)	FTO/TiO_2/4AIN/LHP/spiro-OMeTAD/Ag	1062	130±7	39±2	1.05±0.01	150±10	83±1	[181]
2021	$AgBiI_4$	FTO/c-TiO_2/RDF/spiro-OMeTAD/Au	1000	1.76	5.19	0.66	5.7	0.56	[148]
2022	Cu_2AgBiI_6 (with HI)	FTO/c-TiO_2/RDF/spiro-	1000	17±1	3.7±0.3	0.54±0.04	62±7	63±1	[182]

		OMeTAD/ Au							
2022	Cu_2AgBiI_6 (w/o HI)	FTO/c-TiO_2/RDF/ spiro-OMeTAD/ Au	1000	6±2	1.3±0.5	0.46±0.05	25±6	57±4	[182]
2022	$ATBiI_4$	FTO/c-TiO_2/RDF/ PTAA/Ag	1000	156	0.52	0.71	4.35	50.6	[183]
2022	$ATBiI_4$	FTO/c-TiO_2/RDF/ PTAA/Ag	500	0.82	0.54	0.68	2.55	47	[183]
2023	$Cu_2Ag(BiSb)I_6$	FTO/c-m-TiO_2/RDF/ spiro-OMeTAD/ Au	1000	n.r.	8.3±0.6	0.55±0.01	116±4	68.5±0.7	[184]

LHP: lead-halide perovskite.RDF: rudorffite, spiro-OMeTAD: 2,2,7,7-tetrakis(N,N-di-p-methoxyphenyl-amine)9,9-spirobifluorene; 4A1N:4-aminoaphthalene-1-sulfonate.

As mentioned in Section 1, there has been increasing focus on IPVs as an alternative power source for IoT devices. Ag-Bi-I materials has promising potential in this field due to its optimal bandgap for indoor light harvesting of ~1.9 eV. The indoor spectroscopic limited maximum efficiency (i-SLME) based on measured optical absorption spectra for $Ag_3Bi_2I_6$ has been calculated to reach up to 56.2% under 1000 lux white light-emitting diode (WLED) illumination. However, the highest reported photoconversion efficiency shown is 5.17% by Turkevych *et al.*[139] with a power output of 1.76 μW cm^{-2} measured under WLED light of 1000 lux. Other silver-bismuth-halide IPV device efficiencies are shown in Table 2 against LHP IPV device performance. It was suggested that the low PCE despite high i-SLME may be in part due to the short carrier diffusion length and the usage of E (ETA) structure was proposed to overcome this problem. This method would significantly reduce the absorber thicknes, lowering the carrier travel distance before separation and hence increasing charge carrier collection probability.

Another area of consideration is that hysteresis was observed in Ag-Bi-I IPV performance[141]. Al-Anesi *et al*.[185] achieved hysteresis reduction of Cs_2AgBiI_6 through Sb alloying, which may be due to a reduction in defect density. It has also been proposed that interface passivation or inhibiting ionic motion from alternative ETL/HTLs could be used to reduce hysteresis affects.

Although current literature has reported many techniques for morphology improvements, there has not been a systematic study on how different processing parameters influence the morphology of the thin films. This work aims to elucidate the mechanisms on how the different synthesis steps affect morphology, using machine learning to aid in quantifying improvement in the resulting thin films.

3 Experimental methods

3.1 Sample preparation

3.1.1 Thin film deposition

Vacancy-ordered triple perovskites were prepared inside an N_2-filled glovebox by mixing the AX source (caesium iodide [99.9% purity, Alfa Aesar], caesium bromide (99.98% purity, Alfa Aesar)) precursors with BX_3 (bismuth bromide (99,9% purity, Sigma Aldrich), antimony bromide (99.998% purity, Sigma Aldrich), bismuth iodide (99.9% purity, Alfa Aesar), antimony iodide (99.9% purity, Sigma Aldrich)) precursors in 3:2 ratio to form the desired $A_3B_2X_9$ powdered mixtures in glass vials. The precursors were dissolved in dimethyl sulfoxide (DMSO) (Sigma-Aldrich, anhydrous, 99.99%) to form 0.5 mmol/L solutions. Solutions containing bromide were stirred for an hour at room temperature, whereas solutions containing iodide were stirred for an hour at 70 ^{o}C before cooled and filtered through a 0.2 μm pore polytetrafluoroethylene (PTFE) filter (Fisher Scientific). 40 μL of solution was spin coated at 1000 rpm for 2 s and 4000 rpm for 60 s on to a clean glass substrate, then annealed for an hour at 100 ^{o}C. Glass substrates were cleaned via sonication in de-ionized (DI) water, acetone and isopropanol and then treated with UV-ozone (ATG Scientific, UVC1014) for 15 mins for each step.

$AgBiI_4$ thin films were prepared inside a N_2-filled glovebox by mixing silver iodide powder (99.98% purity, Sigma Aldrich) with bismuth iodide (99.9% purity, Alfa Aesar) in 1:1 molar ratio and dissolved in DMSO. The solution was stirred overnight at 70 ^{o}C and then filtered with same PTFE filter as above. The solution and the substrates were heated to 110 ^{o}C by placing on hotplate for 10 minutes. 200 μL of the solution was pipetted onto substrate and spin coated at 1000 rpm for 2 s and then 6000 rpm for 30 s. 1 mL of antisolvent, chlorobenzene (Merck, anhydrous, 99.8%) isopropyl alcohol (IPA, Sigma Aldrich, 99.5%) or toluene (Sigma-Aldrich, anhydrous, 99.8%), was dripped onto the substrate 20 seconds into the second stage of spin coating with a 1 mL pipette. The thin film was annealed at 70 ^{o}C for 5 mins then 150 ^{o}C for 30 mins.

Compact titanium dioxide was prepared in a fume hood. 350 μL of titanium (IV) isopropoxide (TTIP, 0.24 M, Sigma-Aldrich, 97% purity) in 2.5 mL ethanol in one vial, and 35 μL of hydrochloric acid (2 M) in another vial containing 2.5 mL of ethanol. The solution containing HCl was added drop by drop

into the solution containing TTIP under mixing with a stir bar. It was then stirred for an hour before filtering with a 0.2 μm pore-size PTFE filter. 150 μL of the resulting solution was spin coated onto a substrate that was cleaned with same steps as glass substrate above at 1500 rpm for 45 s. Then it was annealed at 150 ^{o}C for 5 mins, 250 ^{o}C for 10 mins, 350 ^{o}C for 10 mins, 450 ^{o}C for 10 mins, then 500 ^{o}C for 30 mins.

Mesoporous titanium oxide was obtained inside fume hood by first mixing TiO_2 paste (Greatcell Solar Materials, 18NR-T) in ethanol in a 1:3.5 weight ratio and stirred overnight at 700 rpm for a uniform suspension. 200 μL was spin coated at 4000 rpm for 10s and then annealed at 100 ^{o}C for 5 mins, 200 ^{o}C for 10 mins, 300 ^{o}C for 10 mins, 400 ^{o}C for 10 mins, then 500 ^{o}C for 30 mins.

PTB7 (Poly[[4,8-bis[(2-ethylhexyl)oxy]benzo[1,2-b:4,5-b']dithiophene-2,6-diyl][3-fluoro-2-[(2-ethylhexyl)carbonyl]thieno[3,4-b]thiophenediyl]]) (1-Material) thin films were obtained in a N_2 glovebox by dissolving 10 mg of PTB7 powder in 1 mL chlorobenzene and then spin coated onto the absorber layer at 4000 rpm for 30 s.

3.1.2 Device fabrication

Fluorine tin oxide-coated (FTO) substrates (Ark Metrica, 7 Ω sq^{-1} sheet resistance) with a resistivity of 15 Ω cm^{-1} were cleaned via sonication in de-ionized (DI) water, acetone and isopropanol and then treated with UV-ozone (ATG Scientific, UVC1014) for 15 mins for each step. A compact titanium oxide layer is deposited first, followed by a mesoporous TiO_2 layer, then $AgBiI_4$, then PTB7, as shown in Figure 19.a. Then the thin film was scratched off with razor in configuration shown in Figure 19.b to ensure contact between gold top electrode and FTO substrate. 100nm thick gold top electrodes were deposited on top of the PTB7 layer via thermal evaporation (SPECTROS™ 150, Kurt J Lesker) with a vacuum of 10^{-7} mbar. All thin films were fabricated as laid out in 3.1.1. The resulting fabricated devices had 6 0.25 cm^2 pixels and were measured under 1 sun illumination with a scar rate of 1mV/s.

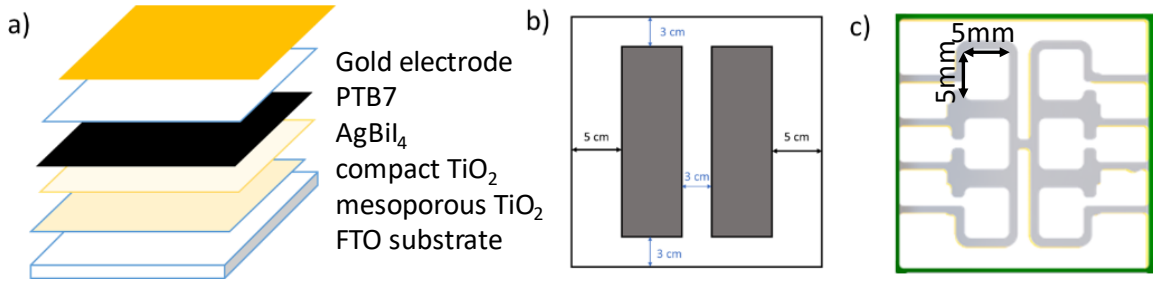

Figure 19. a) Device layout of $AgBiI_4$ PV cell and b) schematic of cell preparation needed before electrode deposition with grey area being untouched thin film layers and white area being area to be scratched off c) mask for gold electrode deposition (white area is area of deposition)

3.2 Material characterisation

X-ray diffraction (XRD) was used to investigate the crystalline structure of the thin film samples. The instrument used was a Bruker D8 Advance powder X-ray diffractometer equipped with a 2.2 kW Cu K_α X-ray tube with a wavelength of 1.5406 Å. The set used a Göbel mirror and a V-Groove crystal to collimate, compress and filter the incident beam. The Göbel mirror is a 60 mm multilayer X-ray mirror constructed on a high-precision parabolic surface and optimized for the Cu-$K\alpha_1$ wavelength. It has a reflectivity of around 955 and acts as both the X-ray collimator and monochromator. The V-Groove is a germanium single crystal with a V-shaped groove precisely etched and polished into its surface. It serves to compress the incident beam through asymmetric (022) reflections so that only the Cu-$K\alpha_1$ wavelength is present in the controlled beam. The final beam produced has a divergence angle of less than 0.007°, and dimensions approximately 0.3 mm by 11 mm.

The films were deposited onto silicon substrates cleaned via same steps as described previously in section 3.1. These measurements are made based on constructive interference of X-rays scattered from crystalline samples, which satisfies Bragg's law: $n\lambda = 2dsin\,\theta$ where n is an integer, λ is the X-ray wavelength, d is the spacing between a set of crystal planes, and θ is the incident angle of the X-ray to the plane. The measurements were performed in the Bragg-Brentano geometry, in which the angle of the X-ray source and detector to the sample surface were the same, such that the scattering vector was kept perpendicular to the surface of the sample.

Highscore Plus software (Version 4.9) was used to perform the data refinements. Due to the high preferred orientation of thin-films, Pawley fitting was chosen to fit the XRD data instead of Rietveld. In Pawley fitting, each diffraction peak is represented by a mathematical function (typically Gaussian

or Lorentzian), and the fitting process adjusts the peak parameters (such as position, intensity, and shape) to match the observed diffraction pattern. It does not rely on a predefined crystal structure, refining lattice parameters and peak profiles independently. The Rietveld method is a full-pattern fitting technique that requires a complete crystallographic model, including atomic positions and lattice parameters. This method refines the parameters by minimizing the difference between the observed and calculated diffraction patterns. It refines peak intensities from structure factors $F(hkl)$, which are calculated from model structure parameters and describes the amplitude and phase of the diffracted X-ray beam corresponding to a particular set of crystal planes indexed by the Miller indices (hkl).

Raman spectroscopy was performed on samples deposited on glass substrates in a JY Horiba LabRAM ARAMIS Imaging Confocal Raman Microscope. A 50x objective employed to focus a continuous 532nm wavelength laser onto the sample. Scattered light was filtered using filter wheel to eliminate the Rayleigh scattering and dispersed using a 2400 lines/mm grating onto a cooled CCD detector. The spectral resolution was 0.75 cm^{-1}, and calibration was achieved using the 520.7 cm^{-1} peak of a silicon wafer.

The incident photons from the laser may scatter elastically (Rayleight scattering) or inelastically via energy exchange with the molecular vibrations of the sample material. The Raman effect is the shift in energy of scattered photons due to inelastic scattering (Stokes and Anti-Stokes scattering) and is specific to vibrational modes and therefore could be used to identify molecular structures. Only vibrational modes that cause a change in polarizability are Raman active.

Profilometry experiments were performed on samples on glass substrates to measure the thickness of thin films. Part of the films were completely scratched off the substrate with a razor blade to create a step edge. A Dektak profilometer was used to measure the height difference between the thin film and the substrate. Background tilt was corrected, and an average thickness was obtained from three different sections for each sample.

Scanning electron microscopy (SEM) and Energy-dispersive X-ray spectroscopy (EDX) were carried out on Zeiss Merlin - Analytical. The samples were prepared by spin-coating the sample solution onto glass/FTO/m-TiO_2 substrate. An electron energy of 10 kV and 20 kV were used for SEM and EDX measurements respectively, and the chamber pressure was maintained at ~ 10^{-5} Pa throughout.

Depending on experiment, some samples were grounded via carbon tape/silver paste. Charge accumulation and slight sample drift was observed in ungrounded samples. No conductive coating was sputtered onto samples before SEM.

Absorption spectroscopy (ABS) was carried out on Agilent Cary 60 UV-Vis-NIR Spectrometer in ambient air. The samples investigated were prepared by spin-coating the sample solution onto glass substrate. The measurements were made after taking the baseline with clear glass.

Photothermal Deflection Spectroscopy (PDS) is an absorption measurement technique that detects the heating of the samples due to the nonradiative relaxation of absorbed photons. It has the advantage of being ultrasensitive, being able to detect absorbance signals 5-6 orders of magnitude weaker than the band edge absorption, and is insensitive to reflection and scattering. Samples were prepared on quartz substrates. The samples were immersed in the inert liquid FC-72 Fluorinert ® (3M Company), which has a high refractive index change per unit change in temperature to enhance the refractive index gradient around the sample surface produced from the thermal gradient. A white light source is used, and this passed through a monochromator so that only one wavelength at a time is illuminated on the samples. A thermal gradient is created near the sample surfaces due to non-radiative relaxation induced heating from photon absorption. A fixed wavelength cw laser probe beam was illuminated onto the sample in the inert liquid, and this probe beam deflected due to the thermal gradient around the sample, with a deflection magnitude proportional to the absorbed light. This deflected beam is detected by a photodiode and lock-in amplifier set-up. Complete absorption spectra were obtained by scanning through various monochromated pump wavelengths.

Transient absorption spectroscopy (TAS) was used to reveal the carrier dynamics of a sample after photoexcitation. A common TAS set-up includes a pump-probe system. The first 'pump' laser pulse excites the sample, then after a controlled time delay (t) the second 'probe' laser pulse with a broadband white light will arrive at the sample. The change in the transmittance (ΔT), is recorded. The final TA signal is recorded as $\Delta T/T$, which can be calculated by the following equation:

$$\frac{\Delta T}{T} = \frac{T_{\text{pump on}} - T_{\text{pump off}}}{T_{\text{pump off}}} \qquad (36)$$

where $T_{\text{pump on}}$ and $T_{\text{pump off}}$ are the transmittance measurements of the probe light with and without the presence of the pump on the samples respectively. Charge-carrier dynamics on different time scales can be monitored by choosing pump pulses with different time durations and pump-probe delays.

TA signals can be categorized into three main types: Ground state bleach (GSB), stimulated emission (SE) and photo-induced absorption (PIA). GSB signifies the carrier depopulation process from the ground state (or valence band, VB) due to the pump excitation. The amount of absorption of the probe light at the corresponding wavelength is reduced and so the $T_{\text{pump on}}$ becomes larger than the $T_{\text{pump off}}$. Therefore, GSB is a positive $\Delta T/T$ signal and usually occurs around the bandgap energy of the sample. SE occurs when electrons that occupy the S_1 state after excitation is stimulated to S_0 by the probe pulse and will also generate a positive $\Delta T/T$ signal. PIA can be seen when excited electrons are promoted into higher excited states that are present near S_1, which is an extra absorption and hence will be seen as a negative $\Delta T/T$ signal.

Therefore, by analysing the resulted overall TA spectra, a change of signal intensity over time at different wavelengths can be obtained which reflects the charge-carrier transitions. However, multiple TA signals may mix together at the same wavelength range, and different mechanisms can possibly lead to similar signal features, so it may prove difficult to attribute the charge-carrier transitions for different materials. Therefore, other complementary spectroscopy techniques may be required to draw definitive conclusions on the charge-carrier dynamics of a material.

Temperature-dependent photoluminescence spectroscopy (cryo-PL) was also used to study charge-carrier dynamics. The PL setup used an intensified Charge-Coupled Device (iCCD)**,** which are charge-coupled device (CCD) cameras with an intensifier unit that multiplies the number of incoming photons and allows electronic gating of the signal. The iCCD camera system Andor iStarDH740 CCI-010 was connected to a grating spectrometer (Andor SR303i). A beta barium borate (BBO) crystal (Eksma Optics) generated femtosecond laser pulses for excitation via second harmonic generation (SHG) from the fundamental output (pulse energy 1.55 eV, pulse length 80 fs) of a Ti:Sapphire laser system (Spectra Physics Solstice). The laser pulses had an energy of 3.1 eV due to frequency doubling from the BBO crystal: due to the $\chi(2)$ nonlinearity of the crystal, a nonlinear polarization wave at twice the fundamental frequency is generated. This setup was placed inside a closed helium compressor (Oxford

Instruments) to obtain PL spectra at different temperatures (lowest temperature possible was 5K). The samples were deposited on quartz substrates, which were placed on a metal plate directly connected to the helium gun to ensure good thermal contact. A thermocouple was connected to the metal plate to read the temperature and ensure that no fluctuations were present when experiments were run.

In this setup, the incoming photons pass through an electronically controlled shutter, and are then converted to photoelectrons through a photocathode. The photoelectrons are intensified by a microchannel plate with high voltage acceleration which ionises the channel wall to increase number of photoelectrons. The photoelectrons are then absorbed into a phosphor coating layer and re-converted into photons to enter the CCD (charged-coupled device) camera. Spectral information can thus be obtained at different shutter time delay, the smallest measurement resolution being around 4 ns, as determined by measuring instrument response to a 100 fs laser pulse.

3.3 Use of machine learning to understand and predict effect of processing conditions on thin film morphology.

I produced and sent SEM images of $AgBiI_4$ synthesized under different processing parameters to Prof. Shijing Sun's group at University of Washington for further analysis of the effect of processing conditions on the film morphology by machine learning. Before image analysis, adaptive histogram equalization (AHE) was used to enhance image contrast, unsharp masking was used to sharpen the image, and bilateral filtering was used to reduce noise. Pixel values in all images were rescaled by a factor of 1/255 so that the input data range was normalized to [0,1]. Three models, Daisy 1.0, Daisy 2.0 and Daisy 3.0 were developed for image analysis. The parameters for the dataset given are as shown in Table 3.

Table 3. $AgBiI_4$ synthesis parameters given for machine learning

Variable	Precursor solution concentration (wt%)	Spincoating speed	Substrates preheated temperature (°C)	Solution preheated temperature (°C)	Substrate size	Composition	Antisolvent used	Antisolvent preheated temperature (°C)	Antisolvent volume	Antisolvent dripping time	Thin film annealing procedure
Antisolvent	35%	1000rpm 2s, 6000rpm 30s	110	110	1"x1"	$AgBiI_4$	chlorobenzene	RT	1 mL	20s	150°C for 30 mins
	35%	1000rpm 2s, 6000rpm 30s	110	110	1"x1"	$AgBiI_4$	toluene	RT	1 mL	20s	150°C for 30 mins
	35%	1000rpm 2s, 6000rpm 30s	110	110	1"x1"	$AgBiI_4$	isopropanol	RT	1 mL	20s	150°C for 30 mins
	35%	1000rpm 2s, 6000rpm 30s	110	110	1"x1"	$AgBiI_4$	none used	N/A	1 mL	N/A	150°C for 30 mins
Composition	40%	6000rpm 30s	RT	RT	1x1 cm	$AgBiI_4$	none used	N/A	1 mL	N/A	150°C for 30 mins
	40%	6000rpm 30s	RT	RT	1x1 cm	Ag_2BiI_5	none used	N/A	1 mL	N/A	150°C for 30 mins
	40%	6000rpm 30s	RT	RT	1x1 cm	Ag_3BiI_6	none used	N/A	1 mL	N/A	150°C for 30 mins
Spinspeed 4000 vs 6000	35%	1000rpm 2s, 4000 rpm 30s	110	110	1"x1"	$AgBiI_4$	none used	N/A	1 mL	N/A	150°C for 30 mins
	35%	1000rpm 2s, 6000rpm 30s	110	110	1"x1"	$AgBiI_4$	none used	N/A	1 mL	N/A	150°C for 30 mins
	35%	1000rpm 2s, 4000 rpm 30s	110	110	1"x1"	$AgBiI_4$	isopropanol	RT	1 mL	20s	150°C for 30 mins
	35%	1000rpm 2s, 6000rpm 30s	110	110	1"x1"	$AgBiI_4$	isopropanol	RT	1 mL	20s	150°C for 30 mins
Temperature	35%	6000rpm 30s	50-150	50-150	1"x1"	$AgBiI_4$	none used	N/A	1 mL	N/A	150°C for 30 mins

Daisy 1.0 was used to train the AI to classify defects. Three different neural network architectures were tested for accuracy: VGG16, Reset50 and U-Net.

The VGG16 model was pre-established in prior works with weights pre-trained on an ImageNet dataset. The original model contains 13 convolutional layers and 3 fully connected layers. The top classification layers were removed for the purposes of this investigation and replaced with custom layers). A fully connected layer with 1025 neurons and ReLU activation was implemented and dense layer with 2 neurons and SoftMax activation was used to perform classification. L2 regularization and dropout layer (20% dropout rate) was used to prevent overfitting.

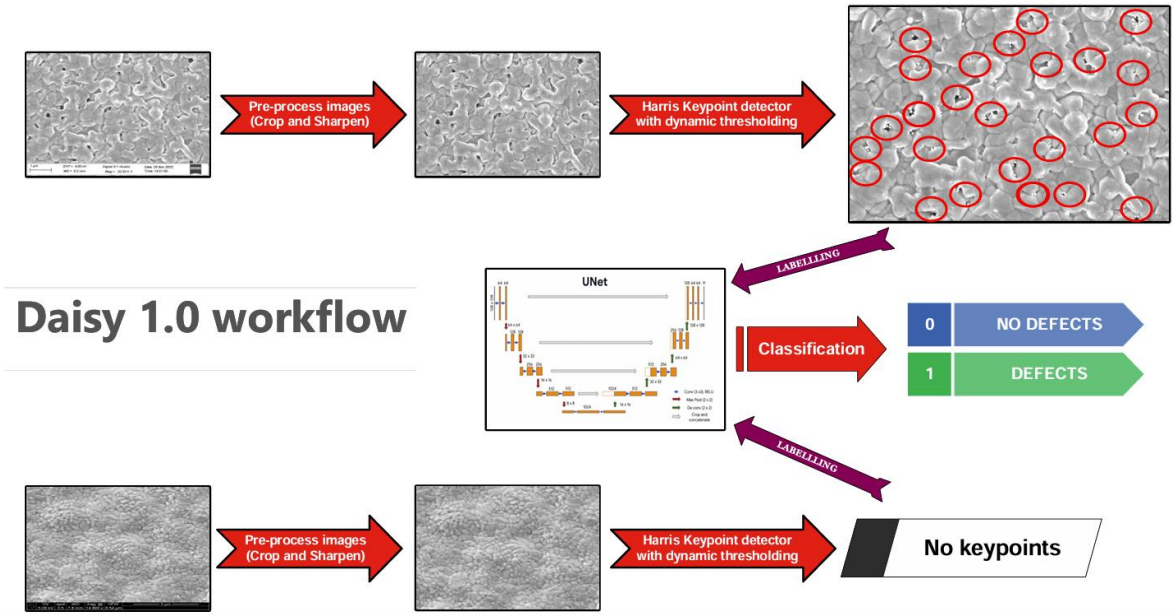

Figure 20. Workflow of Daisy 1.0. The images are pre-processed for image analysis, then classified as defects or no defects by model using Harris Keypoint detect for identifying presence of defects in image.

The ResNet model was another pre-established model, which 50 convolutional layers that allows residual function learning and mitigate the problem of vanishing gradients. For this study, the pre-trained weights were retained, and the last 20 layers were fine-tuned to the image dataset.

The U-Net model was a pre-established network designed for image segmentation. It included an encoder-decoder architecture that captures features at multiple scales through convolutional and max-pooling layers, which the decoder then reconstructs. For this study, a 'skip connections' layer was implemented to retain feature resolution. Custom layers were added at end of decoder so that the model could perform classification on the images: fully connected layer with 1024 neurons and ReLU activation, a dropout layer (50% dropout rate) to mitigate overfitting, and a final output layer with 2 neurons and SoftMax activation.

The three models were compared based on accuracy, precision, recall and F1-score (harmonic mean of precision and recall score). These were determined by comparing model classification of defects against manual labels.

Dairy 2.0 was used to determine the images with best morphology. Initial mask generation used a Segment Anything Model (SAM) for image region separation and identification. The images were taken as input and applied to a pre-trained neural network to be segmented into different regions. Visual characteristics such as texture, colour and intensity were identified for these regions, which were then delineated. Crude masks were produced that provide approximate segmentations of the images that marked out grain-containing and defect-containing regions. A secondary SAM generator was used to refine these masks by adjusting key parameters to improve accuracy and stability. Points per side parameter was adjusted to control density of points in the segmentation process. Increasing point density increases mask detail. Intersection-over-Union (IoU) thresholds determined overlap between predicted masks. Changes to this parameter can enhance distinction and accuracy of image segments. Stability scores measured mask consistency and dynamic filtering removed excessively large masks (>10% of total image area) after mask refinement so that only relevant segments were retained for analysis.

U-Net model was then used to classify the images into either a ‘no defects’ or a ‘defects’ category. The former images had masks that generated primarily mark grain clusters, which were then used to analyse the quality of material based on grain structures. The latter had an additional k-means clustering step to separate defects from clusters by labelling masks based on their mean intensity. In cases where the masks overlap, the mask with the largest area was prioritized. The coverage percentage of both defect and grain masks were calculated to quantify the extent of defects in the image. For grain masks, the area and circularity of the grains were calculated as an indicator of morphology quality.

The labelled masks were then visualised to provide representation of results.

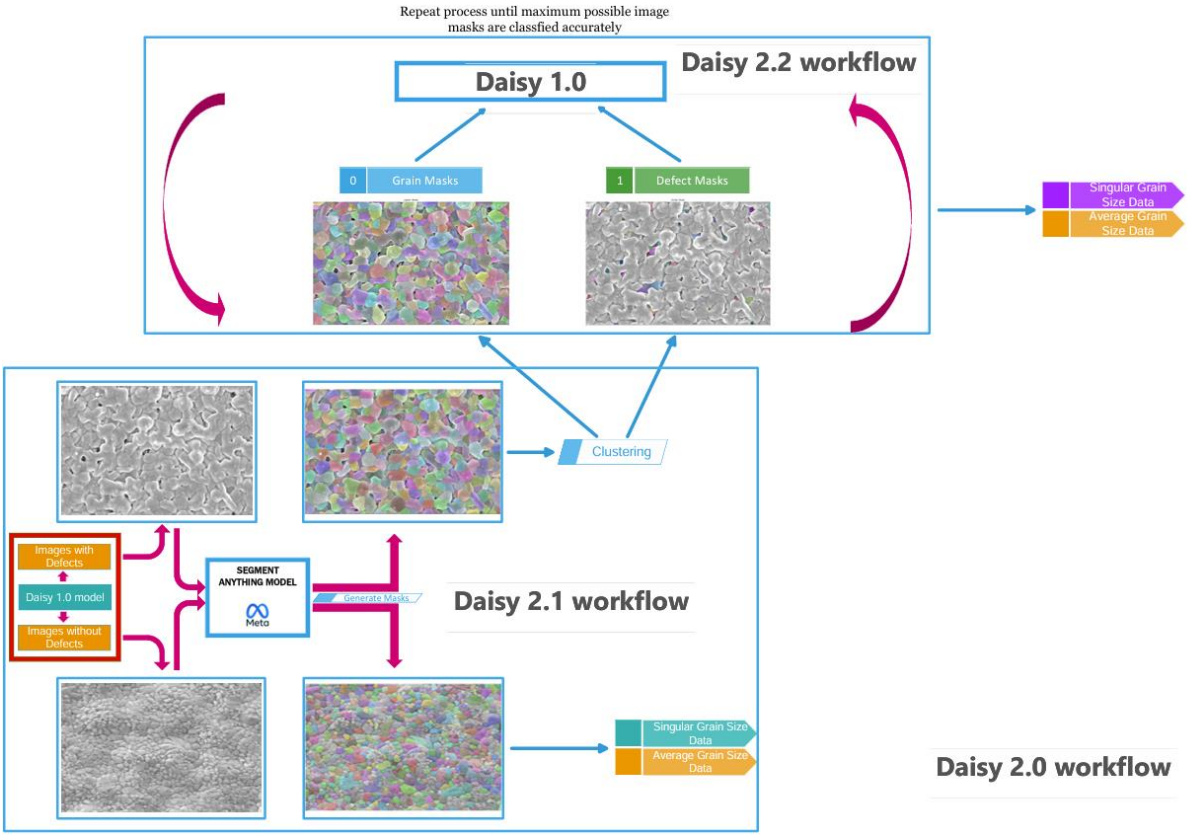

Figure 21. Daisy 2.0 workflow. Images labelled 'no defects' from Daisy 1.0 are given grain masks to calculate average grain size. Images labelled 'defects' are given defect masks to calculate defect coverage percentage as well as a grain mask.

Daisy 3.0 was used to determine the best combinations of the process parameters. Two processes were explored: the Reinforcement Learning (RL) process and the Random Forest (RF) process.

To carry out the RL process, the data set was loaded with parameter combinations provided by myself and the corresponding outcomes from Daisy 2.0 (defective coverage percentage and average grain size). Each processing parameter feature (e.g. spincoating speed) was converted into numerical values using label encoding and custom environment was creased using processed data and labelled encoders. The environment checked the existence of selected parameter combination in the dataset and retrieved the outcomes. If combination existed in the dataset, higher rewards were assigned for lower defect coverage percentages and average grain sizes, while parameter combination not in dataset were given negative rewards. Through multiple iterations the RL agent was trained to favour actions that yielded higher rewards.

The RF process used polynomial features generated from categorical features. This way, the model was able to capture more complex relationships between input parameters rather than computing the combination set as a whole. The data was split into training and testing sets for both targets (80-20 split and a grid of hyperparameters for the model was defined. 5-fold cross-validation was performed to identify best hyperparameters (the data was split into 5 groups, 1 taken as a test data set while the other for are used as training data set and fitted with model to evaluate on test set to evaluate the model) and the best models for least defect coverage and largest grain sizes were trained using the identified hyperparameters. A combined score was then calculated by subtracting normalized 'coverage percentage' from normalized 'average size scale sized'. The parameter combination with the highest score could then be extrapolated by the model.

4 Understanding influence of dimensionality and composition on carrier localisation in $Cs_3Sb_xBi_{2-x}Br_yI_{9-y}$

Vacancy-ordered triple perovskites $A_3B_2X_9$ have recently emerged as a promising class of materials for solar absorbers. These materials are comprised of elements which are not restricted for use in consumer electronics, and, as discussed in Section 2.3 the stabilities demonstrated surpass those of methylammonium lead iodide perovskites. Whilst many compounds within this family of materials have 0D structural dimensionality, this can be increased to 2D structural dimensionality by tuning the composition, leading to important changes in the optoelectronic properties. These include the exciton binding energy, and the propensity for self-trapping to occur. These properties critically determine the photovoltaic performance of these materials, since they affect the charge-carrier transport length and quasi-Fermi level splitting. Although 0D-structured materials have strong propensity to form self-trapped excitons, it not well established whether this could be addressed by tuning the chemistry of the pnictogen species in 0D and 2D compounds.

Therefore, this chapter aims to understand how carrier localisation is affected by compositional changes to $Cs_3Sb_xBi_{2-x}Br_yI_{9-y}$. The effect of varying the pnictogen species, bismuth and antimony, is studied, while the structural dimensionality of these compounds are tuned by adjusting the halogen species.

4.1. Introduction

The vacancy-ordered triple perovskites (general formula $A_3B_2X_9$) considered here have Cs^+ as the A-site species, Sb^{3+} or Bi^{3+} as the B-site species, and Br^- or I^- as the X-site species. These materials are considered to have potential for indoor photovoltaic applications because of their photo-stable bandgaps close to the optimal value of 1.9-2.0 eV, absence of toxic elements that are regulated, and promising thermal and environmental stability [2]. However, a critical limitation of these materials is their low structural dimensionality. Early work on $A_3B_2X_9$ for photovoltaics focused on $Cs_3Bi_2I_9$[186, 187] and the isostructural $MA_3Bi_2I_9$[186, 188, 189]. However, these materials have 0D structural dimensionality, in which BiI_6 octahedra occur in face-sharing pairs (*i.e.*, $Bi_2I_9^{3-}$) that are isolated from each other. Although the A-site cation surrounds these dimers, these do not contribute to the electronic density of states at band extrema, which are instead dominated by hybridization between I and Bi valence orbitals. Therefore, the electronic dimensionality is also 0D, and this leads to localization of the electron/hole wavefunctions to the inorganic dimers, hence higher exciton binding energies, as well as a high tendency for self-trapping. As explained in Section 2.3.4 and 2.3.5, both factors reduce photovoltaic performance due to reduced carrier mobility.

Importantly, as we change the species at the B and X sites for small species (Bi^{3+} for Sb^{3+}, and I^- for Br^-), the structural dimensionality of the compound is changed. As mentioned in Section 2.3.3, Br-based compounds have a 2D layered structure, and I- based compounds have a 0D structure. The exception is $Cs_3Sb_2I_9$ which is able to form a 2D phase at high processing temperatures. However, the effects of this structural dimensionality tuning on carrier localization is not well understood across the entire family of $Cs_3Sb_xBi_{2-x}Br_yI_{9-y}$ materials.

If we look to the related family of vacancy-ordered double perovskite materials, there has been substantial work on understanding carrier localization in $Cs_2AgBiBr_6$. Both Fröhlich coupling and charge-carrier coupling to acoustic phonons occur in this material. Fröhlich coupling arises because of the polar nature of the material, enabling interactions between charge-carriers and the local dipoles that form when a longitudinal optical (LO) phonon propagates through the structure. However, the Fröhlich coupling constant of $Cs_2AgBiBr_6$ is 2.54 and 2.00 for electrons and holes respectively[190] which is in

the intermediate range (*i.e.*, not strong enough to give rise to carrier localisation) and is similar to the values found in 3D lead-halide perovskites (2.4 and 2.7 for electrons and holes respectively)[191], which have delocalized charge carriers. Wu *et al.* proposed that localisation in $Cs_2AgBiBr_6$ mainly arises from charge-carrier coupling to acoustic phonons. This occurs due to the large deformation potential of $Cs_2AgBiBr_6$ (13.7 and 14.7 eV at VBM and CBM respectively) compared to lead based perovskites such as $CsPbBr_3$ (2.2 and 6.3 eV at VBM and CBM respectively)[192]. As explained in Section 2.1.3, when the deformation potential is high, there will be strong acoustic phonon coupling. Furthermore, although $Cs_2AgBiBr_6$ has 3D structural dimensionality, it has 0D electronic dimensionality. This is because the band-extrema are comprised of hybridisation of Ag and Bi valence orbitals with Br valence orbitals. However, there is an alternation of $AgBr_6$ and $BiBr_6$ octahedra. Since Ag 4d and Bi 6s orbitals are not at the same energies, there are discontinuities in the orbitals at the band-extrema with each alternating octahedron, leading to 0D electronic dimensionality. Such low electronic dimensionality would give rise to no barrier to carrier localisation, as explained in Section 2.1.3. Indeed, Wright *et al.*[138] provided direct experimental proof of self-trapping in $Cs_2AgBiBr_6$ from optical pump terahertz probe (OPTP) spectroscopy measurements, which showed several signatures of self-trapping: 1) a rapid decay in the photoconductivity on a picosecond timescale, 2) this localization not being temperature-dependent (indicating an energetically-barrierless process, consistent with a 0D electronic dimensionality), and 3) an increase in the mobility of the localized state with temperature, which is consistent with localised states and is the opposite trend to the behaviour of large polarons. Li *et al.* also fabricated $Cs_2AgBiBr_6$ into thin film transistors, and also demonstrated the mobility to increase with temperature[193]. From these investigations into vacancy-ordered double perovskites, we propose that changing the electronic dimensionality of vacancy-ordered triple perovskites from 0D to 2D would reduce the propensity for self-trapping. However, this also depends on the acoustic coupling constant (which depends on the deformation potential and stiffness of the structure), since strong acoustic coupling in an electronically 2D material would still lead to self-trapping.

Therefore, in this chapter, I compare the compounds $Cs_3Bi_2I_9$, $Cs_3Sb_2I_9$, $Cs_3Bi_2Br_9$, and $Cs_3Sb_2Br_9$ compounds. $Cs_3Bi_2I_9$, as the reference compound is structurally 0D, but reducing the size of the pnictogen (replacing with Sb^{3+}) and halogen (replacing with Br^-) could change the materials to 2D.

Whilst past work has focussed only on Bi-based compounds or only on Sb-based compounds, it is important to compare and contrast these two pnictogens, since they change the electronic and mechanical properties of the materials, which can also influence carrier localisation. Practically, mixing Bi with Sb in the pnictogen site further lowers the bandgap through bandgap-bowing, leading to materials with bandgaps closer to 1.9 eV, and therefore better-suited for indoor photovoltaics applications.

These compounds were synthesized as thin films by spin-coating, as described in Chapter 3. XRD was used to confirm their phase purity. UV-Vis spectroscopy and photothermal deflection spectroscopy (PDS) were used to investigate the their optical electronic properties. Temperature-dependent photoluminescence spectroscopy (cryo-PL) and transient absorption spectroscopy (TAS) were used to characterise excitonic behaviour in these materials, and the strength of carrier-phonon coupling.

4.2. Tuning the structural dimensionality of the vacancy-ordered triple perovskites through composition

The effect of halide and pnictogen species on dimensionality was investigated by XRD. Thin films of $Cs_3Bi_2I_9$, $Cs_3Bi_2Br_9$, $Cs_3Sb_2I_9$, and $Cs_3Sb_2Br_9$ were made on silicon wafers as described in Section 3.1. At the start of the project, attempts were made to create phase pure samples containing mixed pnictogen and halide species, but all XRD results showed a 2D/0D mixture as shown below in Figure 22. This is in accordance with previous literature[85] that suggests that this is due to iodide ions localising to this pnictogen vacancy sites to alleviate the strain of the size mismatch. Hodgkins *et al.* were able to create powdered phase pure samples up to maximum of two-thirds iodide content for powdered samples but attempts to prepare mixed halide samples also resulted in multiphase thin films[85]. Therefore, this research will focus on pure phased, non-mixed compounds for clarity of comparisons.

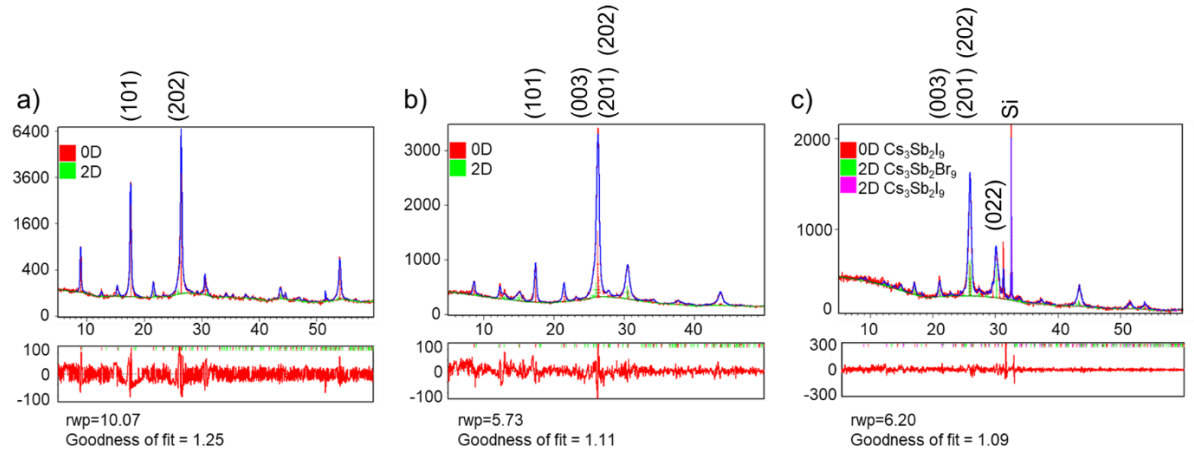

Figure 22. XRD patterns of a) $Cs_3Bi_2Br_3I_6$ b) $Cs_3BiSbBr_3I_6$ and c) $Cs_3Sb_2Br_3I_6$, fit using the Pawley method. The residuals and agreement indices are shown

As shown in Figure 23, the films containing bromide matched 2D reference patterns with a $P\bar{3}m1$ space group where $[Bi/SbBr_6]^{3-}$ octahedra are corner-sharing with other octahedra to form 2D layered perovskites. Films containing iodide have a 0D $P6_3/mmc$ space group where $[Bi/Sb_2I_9]^{3-}$ anions are formed from face-sharing Bi/SbI_6 octahedra. Although $Cs_3Sb_2I_9$ has a 2D polymorph, the formation of the 0D phase is preferred at lower synthesis temperatures[87, 94].

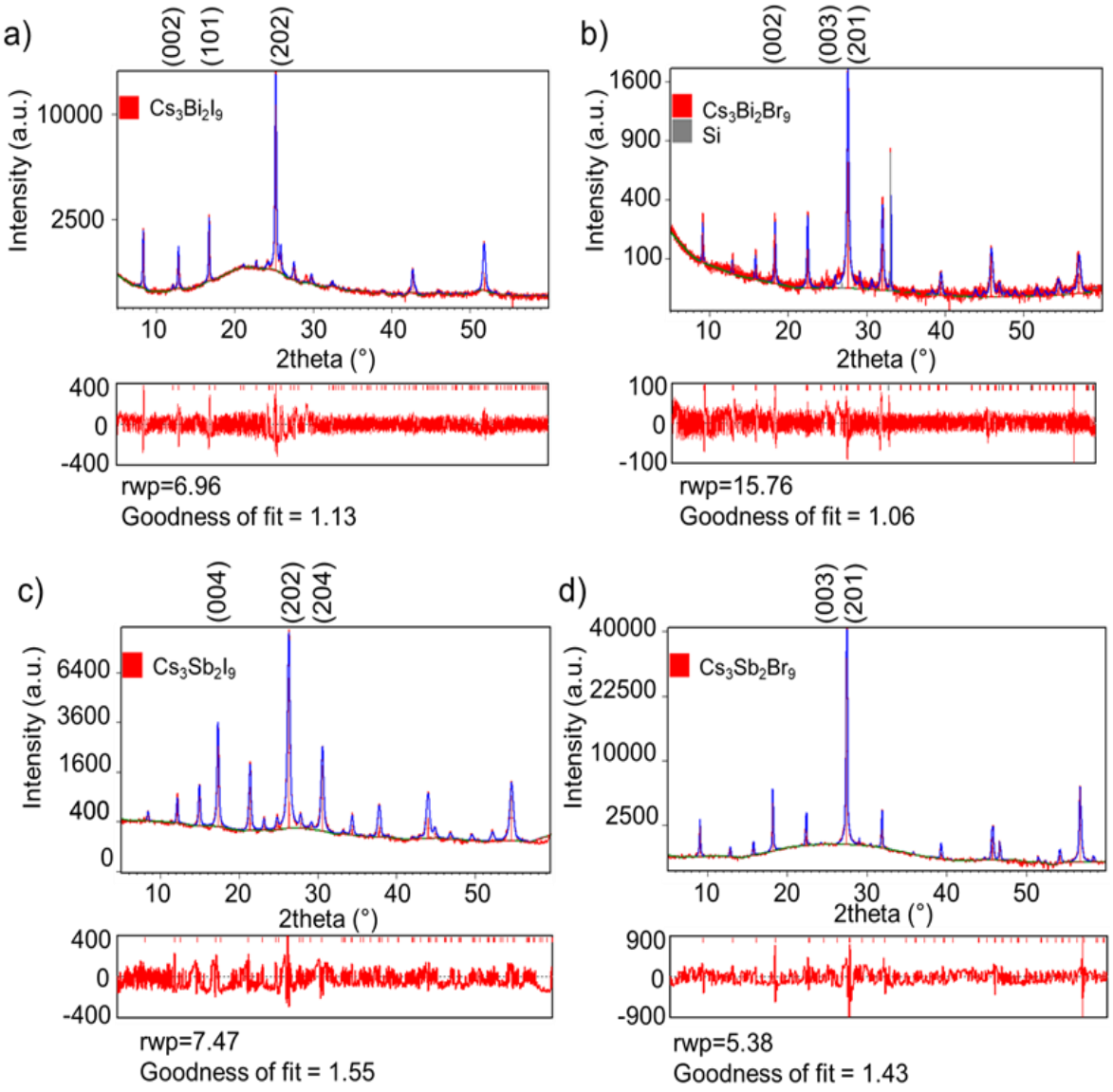

Figure 23. XRD patterns of a) $Cs_3Bi_2I_9$ b) $Cs_3Bi_2Br_9$ c) $Cs_3Sb_2I_9$ and d) $Cs_3Sb_2Br_9$ thin films deposited onto silicon substrates, fit using the Pawley method. The residuals and agreement indices are shown.

The fitted XRD patterns of $Cs_3Bi_2I_9$, $Cs_3Bi_2Br_9$, $Cs_3Sb_2I_9$, and $Cs_3Sb_2Br_9$ are further fitted against 2D.

0D, 2D and 0D reference patterns respectively in Figure 24 to confirm their dimensionalities.

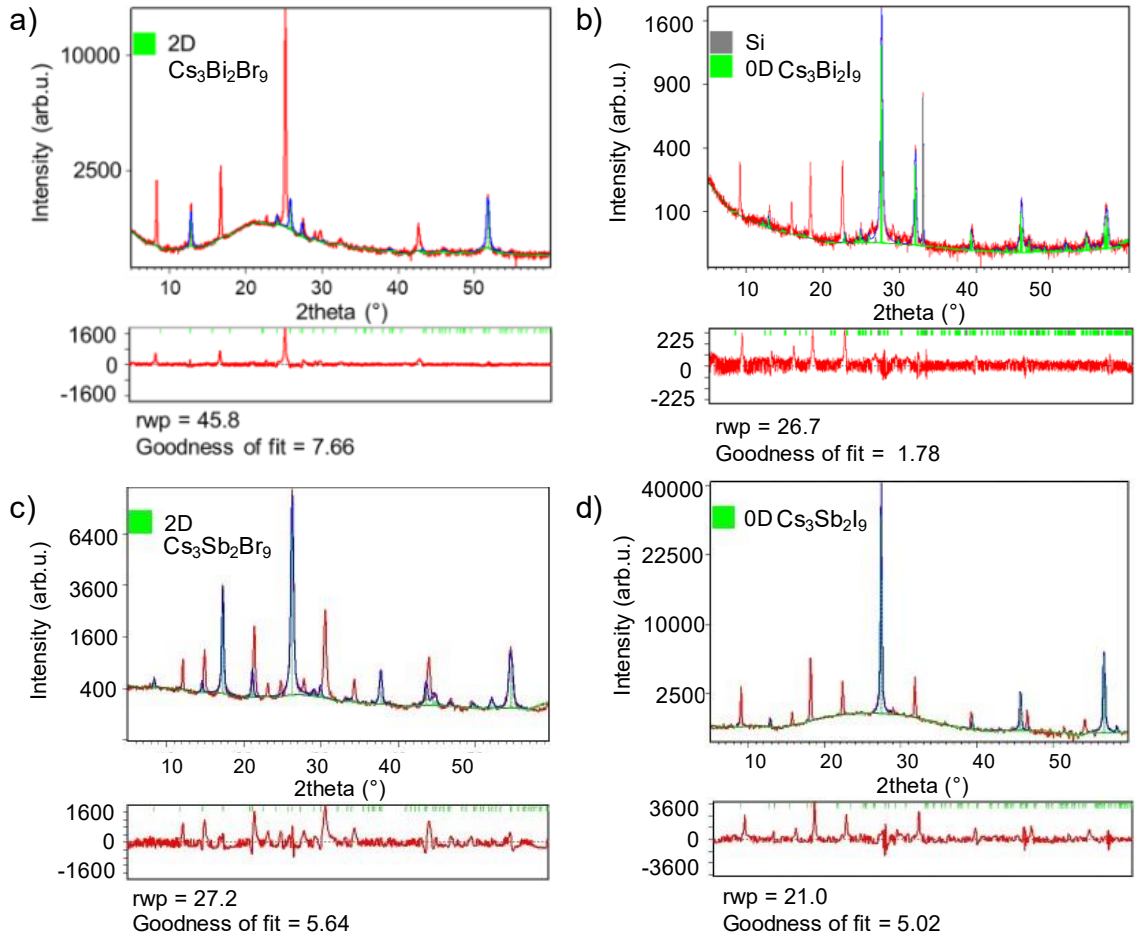

Figure 24. XRD fitting of a) $Cs_3Bi_2I_9$ b) $Cs_3Bi_2Br_9$ c) $Cs_3Sb_2I_9$ and d) $Cs_3Sb_2Br_9$ against 2D. 0D, 2D and 0D reference patterns respectively add goodness of fit

All thin films exhibited preferred orientation, as shown in Table 4. Texture coefficients were calculated by determining the ratio of intensities of peaks with respect to the highest intensity reflection of the reference profile. Calculation of texture coefficients are shown in Table 5. Views of the structure of these materials along the axes of preferred orientation are shown in Figure 25.

Table 4. Preferred orientation of vacancy-ordered triple perovskites

Sample	Orientation
$Cs_3Bi_2I_9$	(0 0 6)
$Cs_3Bi_2Br_9$	(2 0 1)
$Cs_3Sb_2I_9$	(0 0 4)
$Cs_3Sb_2Br_9$	(0 0 3)

Table 5. Texture coefficient calculations for $Cs_3Bi_2I_9$, $Cs_3Bi_2Br_9$, $Cs_3Sb_2I_9$, and $Cs_3Sb_2Br_9$,

Sample	h	k	l	2θ	Relative Intensity	S	Measured Intensity (Arb. U.)	TC (hkl)	Orientation
$Cs_3Bi_2I_9$	2	2	0	42.99	100.00	8	245.59	0.03	(0 0 6)
	0	0	6	25.13	77.26	36	10349.27	1.89	
	0	0	2	8.32	13.80	4	966.80	0.99	
	0	0	4	16.68	17.62	16	1361.12	1.09	
	2	0	2	25.85	19.13	8	419.73	0.31	
	1	0	1	12.84	5.37	2	602.16	1.58	
$Cs_3Bi_2Br_9$	0	2	2	31.69	100.00	8	125.04	0.28	(2 0 1)
	2	2	0	45.59	90.82	8	84.16	0.21	
	2	0	1	27.35	51.00	5	665.26	2.95	
	1	0	2	22.13	38.63	5	95.07	0.56	
	0	0	2	18.01	18.98	4	150.78	1.80	
	0	0	1	8.96	18.13	1	112.54	1.40	
$Cs_3Sb_2I_9$	2	2	0	43.31	100.00	8	306.68	0.04	(0 0 4)
	0	0	6	25.53	99.64	36	5999.40	0.88	
	2	0	4	30.03	59.99	20	1614.42	0.39	
	0	0	4	16.94	12.70	16	2278.20	2.62	
	0	0	12	52.46	79.66	144	838.96	0.15	
	1	0	2	14.88	4.68	5	609.90	1.91	
$Cs_3Sb_2Br_9$	0	0	3	27.52	67.34	9	31064.20	3.49	(0 0 3)
	0	0	6	56.96	67.75	36	4610.51	0.51	
	0	0	2	18.25	12.23	4	18.25	0.01	
	0	0	1	9.12	9.09	1	1180.71	0.98	
	2	0	2	31.89	7.27	8	831.29	0.86	
	2	2	0	45.85	85.83	8	719.46	0.06	

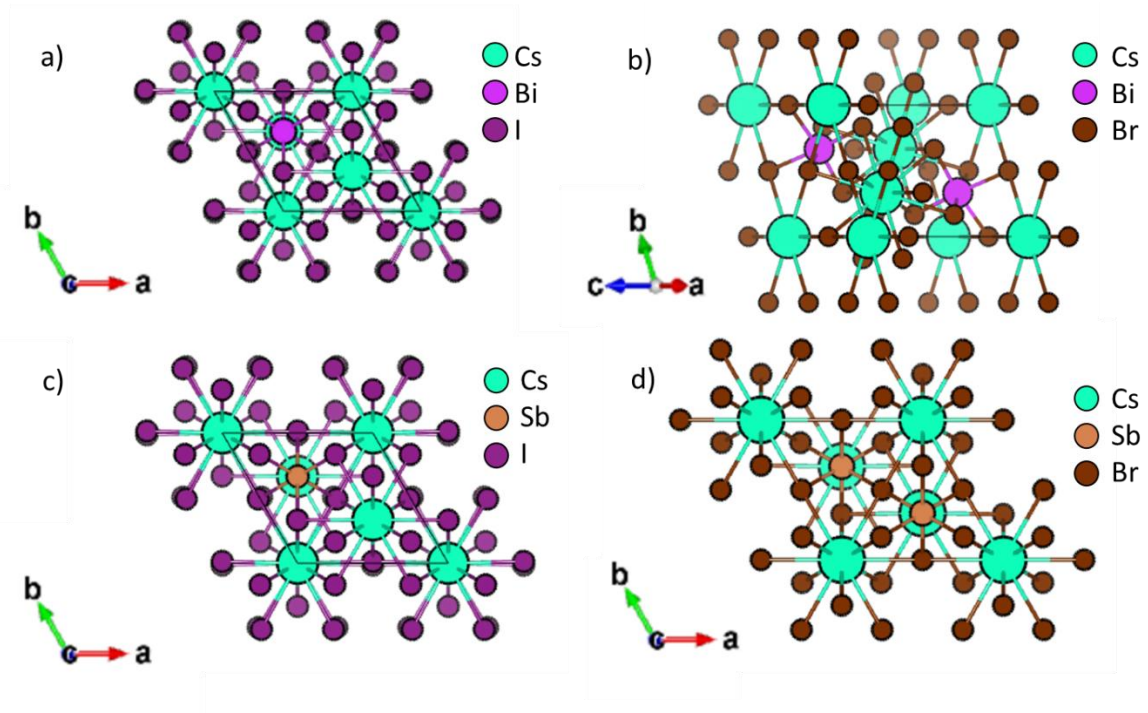

Figure 25. Crytal structure of a) $Cs_3Bi_2I_9$ along projection vector [006], b) $Cs_3Bi_2Br_9$ along projection vector [201], c)$Cs_3Sb_2I_9$ along projection vector [004], and d)$Cs_3Sb_2Br_9$ along projection vector [003].

The Raman spectra of the films were also measured, as shown in Figure 25, using excitation from a 532 nm wavelength continuous wave laser was used to characterise the samples.

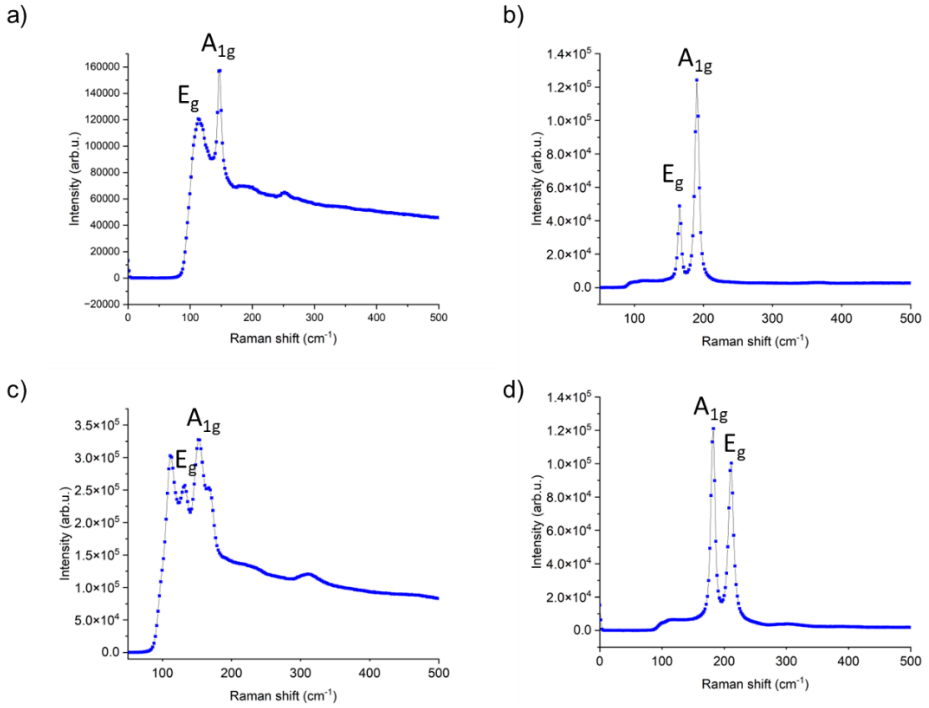

Figure 26. Raman spectra of a) $Cs_3Bi_2I_9$, b) $Cs_3Bi_2Br_9$, c) $Cs_3Sb_2I_9$, and d) $Cs_3Sb_2Br_9$

$Cs_3Bi_2I_9$ and $Cs_3Sb_2I_9$ have D_{6h} symmetry[194] while $Cs_3Bi_2Br_9$ and $Cs_3Sb_2Br_9$ have D_{3d}[195] symmetry. For all the samples, the only Raman-active modes are A_{1g} and E_g. The peaks are in agreement with previous literatures[93, 196-199] and have been assigned to stretching modes of pnictogen-halide octahedra [Bi/Sb – Br_3/I_3]. The $Cs_3Bi_2I_9$ Raman bands at ~150 cm^{-1} and ~ 130 cm^{-1} were assigned to v_sA_{1g} and v_aE_g due to terminal Bi-I stretch respectively[196]. Lower frequency Bi-I bending and Cs-I vibrational modes were also reported below 100 cm^{-1}[196, 197]. For $Cs_3Bi_2Br_9$, the strongest Raman bands of A_{1g} symmetry at ~190 cm^{-1} and E_g symmetry at ~170 cm^{-1} were assigned to the symmetrical and asymmetrical terminal Bi-Br stretch modes respectively[198]. Literature has observed Raman bands below 80 cm^{-1} but could not assign more precisely than attributing them to the deformation modes of the Br–Bi arrangements and the translational modes of caesium cations. $Cs_3Sb_2I_9$ have v_sA_{1g}, v_aE_{2g} and v_aE_{1g} modes due to terminal Sb-I stretch at ~164 cm^{-1}, ~145 cm^{-1} and ~130 cm^{-1} respectively, with Sb-I bridge stretch and as well as unassigned bending modes at lower frequencies[196, 199]. For $Cs_3Sb_2Br_9$ literature found three typical peaks at 77 cm^{-1},185 cm^{-1}, and 213.8 cm -1 assigned E_g, A_{1g}, and E_g, respectively[93], the latter two of which matches with the experimental data. It should be noted that due to instrument limitations there is a low wavenumber cut-off at 100 cm^{-1} and the lack of data below this range does not mean that low-energy phonon modes are not present.

4.3. Influence of dimensionality on exciton binding energy, bandgap, and luminescence

The optical absorption of materials provides important information into the bandgap and species present at steady-state, including free carriers vs. excitons, and defect states. Two complementary techniques were used: UV-visible spectrophotometry (UV-Vis) and photothermal deflection spectroscopy (PDS). UV-Vis is suitable for measuring the absolute optical density, and resolving the above-bandgap absorption features, but is not sufficiently sensitive to resolve sub-bandgap features. Furthermore, sub-bandgap features are convoluted with optical interference effects for thin film samples because of the refractive index mismatch between the thin film (1.9 -3.7)[123, 200, 201], air (1.0) and the glass substrate (1.5). PDS, on the other hand, measures optical absorption differently (as described in Section 3.2), and is sensitive to absorption features below the optical bandgap, but saturates above the bandgap when

the optical density is high. Therefore, to obtain a complete picture for the optical absorption of the thin film materials, I measured PDS and UV-Vis on all samples, and stitched together the PDS data with the UV-vis. That is, at the inflection point of the absorption onset from UV-Vis, I replace the absorption data below that point with the PDS data, which was scaled to match the absolute values of absorbance obtained from UV-Vis (Figure 26).

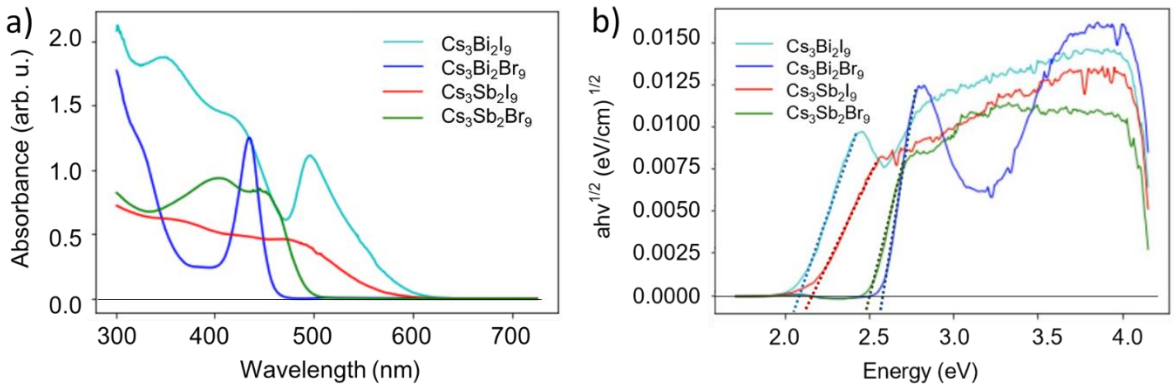

Figure 27. (a) Absorbance spectra of $Cs_3B_2X_9$ series compiled from UV Vis and PS data, and (b) Tauc plots

To perform these measurements, $Cs_3Bi_2I_9$, $Cs_3Bi_2Br_9$, $Cs_3Sb_2I_9$, and $Cs_3Sb_2Br_9$ were all deposited on glass substrates, as described in Section 3.1.1. The energy of absorption onset of $Cs_3Bi_2I_9$, $Cs_3Bi_2Br_9$ $Cs_3Sb_2I_9$ and $Cs_3Sb_2Br_9$ were calculated via fitting to Tauc plot to be ~2.05 eV, ~2.47 eV, 2.11 eV and 2.56 eV respectively (Figure 26.b). Elliott model could not be fitted due to background of UV-Vis spectra.

$Cs_3Bi_2I_9$ and $Cs_3Bi_2Br_9$ have similar spectra in that there is an absorption peak (at ~2.5 eV and ~2.85 eV respectively) before full absorption onset (~2.6 eV and ~3.2 eV respectively). The shift to higher energy for both the peak and full absorption onset was expected due to the smaller lattice constant of the bromide resulting in a higher bandgap. As discussed in Section 2.3.5, some literature have assigned these peaks to the narrow sub-bands of the vacancy-ordered triple perovskite, while others assign these peaks to excitons[202]. Given that the Sb-samples have much more continuous spectra despite having very similar density of states to the Bi- samples[113, 203], the presence of the peaks are more likely to be due to the presence of excitons. Furthermore, Bi- samples are known to have low dielectric constant and high effective mass of charges[31] which results in high exciton binding energies (300 meV and 278

meV for $Cs_3Bi_2I_9$ and $Cs_3Bi_2Br_9$ respectively)[112, 121], and hence it there is likely strong exciton localization around the bismuth sites in the lattice.

4.4. Temperature dependent Photoluminescence (PL)

Temperature dependent PL measurements were taken for $Cs_3Bi_2I_9$ and $Cs_3Sb_2I_9$ thin films deposited on quartz substrates. Due to time and equipment constraints bromide samples were unable to be measured for temperature-dependent PL. Beta barium borate (BBO) crystal (Eksma Optics) was used to generate femtosecond laser pulses (fundamental pulse energy 1.55 eV, pulse length 80 fs) The laser pulses had an excitation energy of 3.1 eV due to frequency doubling via second-harmonic generation. The range was 500 – 900nm, and the rise in PL at high energies as seen in Figure 29 is the laser edge. The samples were measured at 100 µW fluence, with 0.1 s exposure time and 20 accumulations.

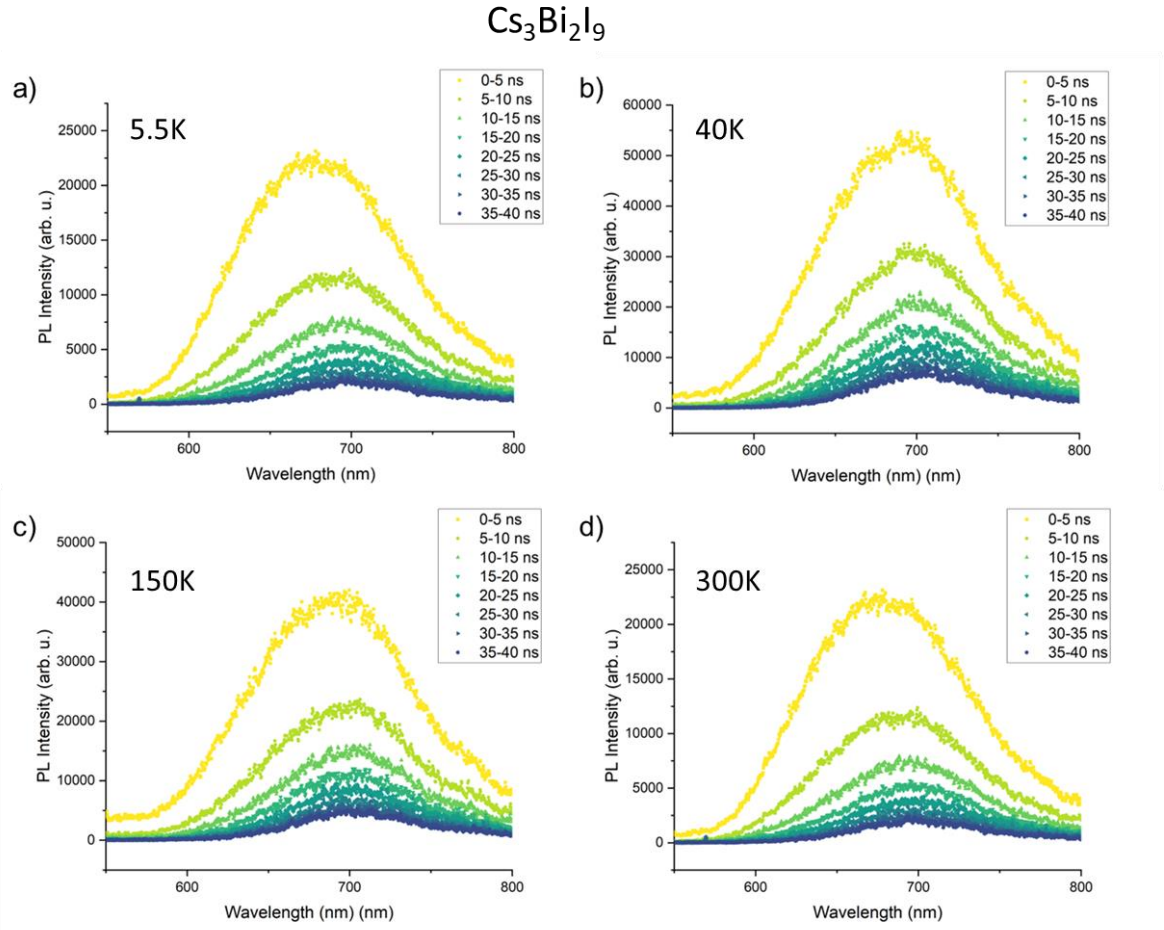

Figure 28. PL decay spectra with of $Cs_3Bi_2I_9$ at a)5.5K, b) 40K, c) 150K and d) 300K from 0-40ns after excitation with 400nm laser at 100 µW at 5ns intervals.

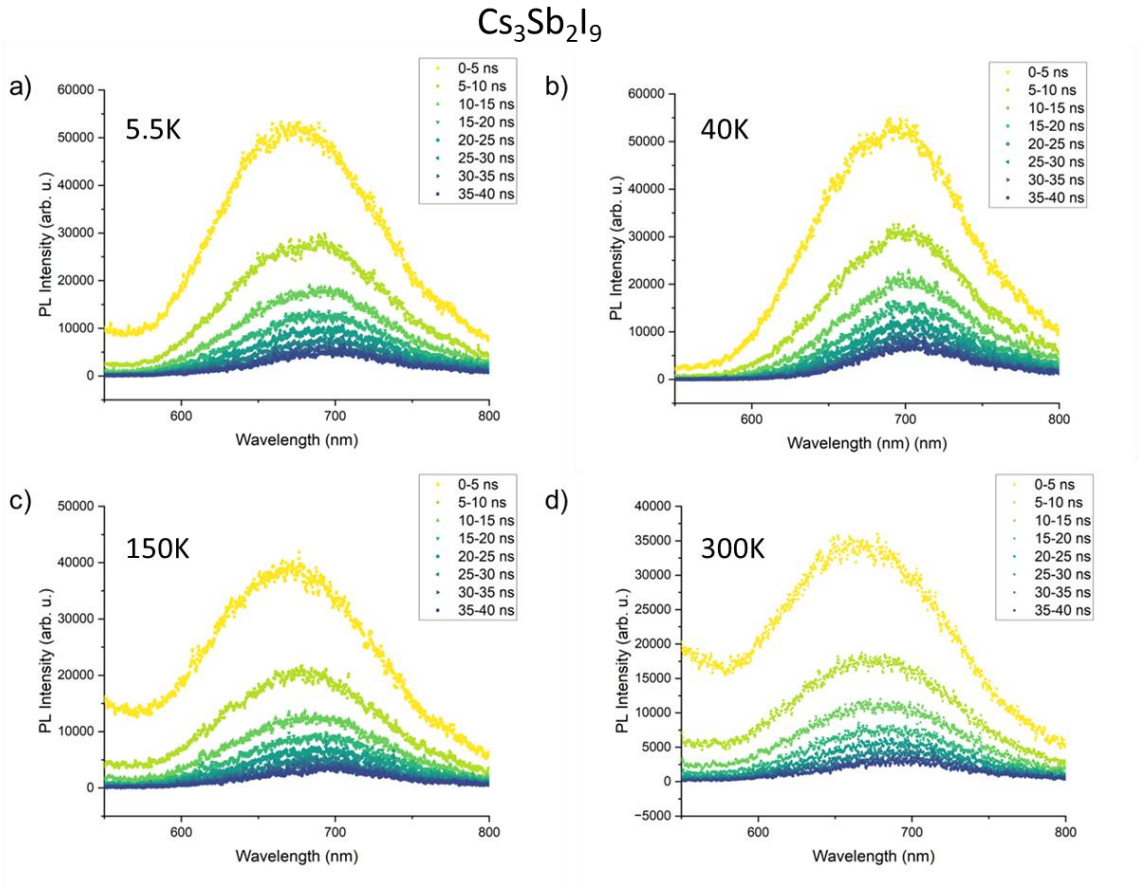

Figure 29. PL decay spectra of $Cs_3Sb_2I_9$ at a)5.5K, b) 40K, c) 150K and d) 300K from 0-40ns after excitation with 400nm laser at 100 µW at 5ns intervals.

The emission peak at both $Cs_3Bi_2I_9$ and $Cs_3Sb_2I_9$ are centred at approximately ~690 nm and ~670 nm respectively, indicating that there is a Stokes shift compared to that of the absorption spectra peaks which were at ~500 nm and ~490 nm respectively. The broad spectra and large Stokes shift suggest the presence of self-trapped excitons (STEs)[204] and hence strong carrier-phonon interactions. The blue-shift in the emission peak with decreasing temperature is likely due to the lattice parameter decreasing due thermal contraction, which leads to the increase of bonding and anti-bonding orbital gap and hence increase in band gap. As shown in Figure 30, there is no significant change in PL decay lifetime with decreasing temperature, which indicates immediate formation of STEs from free excitons. This is in accordance with literature as discussed in Section 2.3.6 that there is no barrier to STE formation in 0D-electronic structured materials.

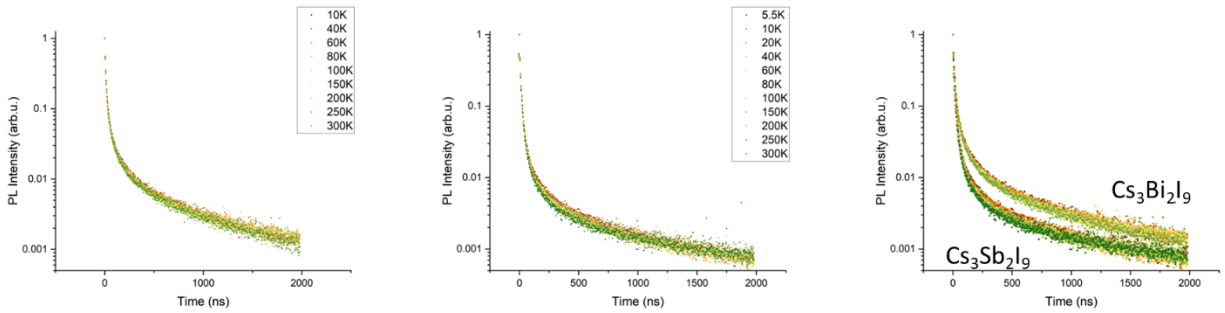

Figure 30. PL decay kinetics at different temperatures of a) $Cs_3Bi_2I_9$, b) $Cs_3Sb_2I_9$ and c) of $Cs_3Bi_2I_9$ and $Cs_3Sb_2I_9$ combined as comparison.

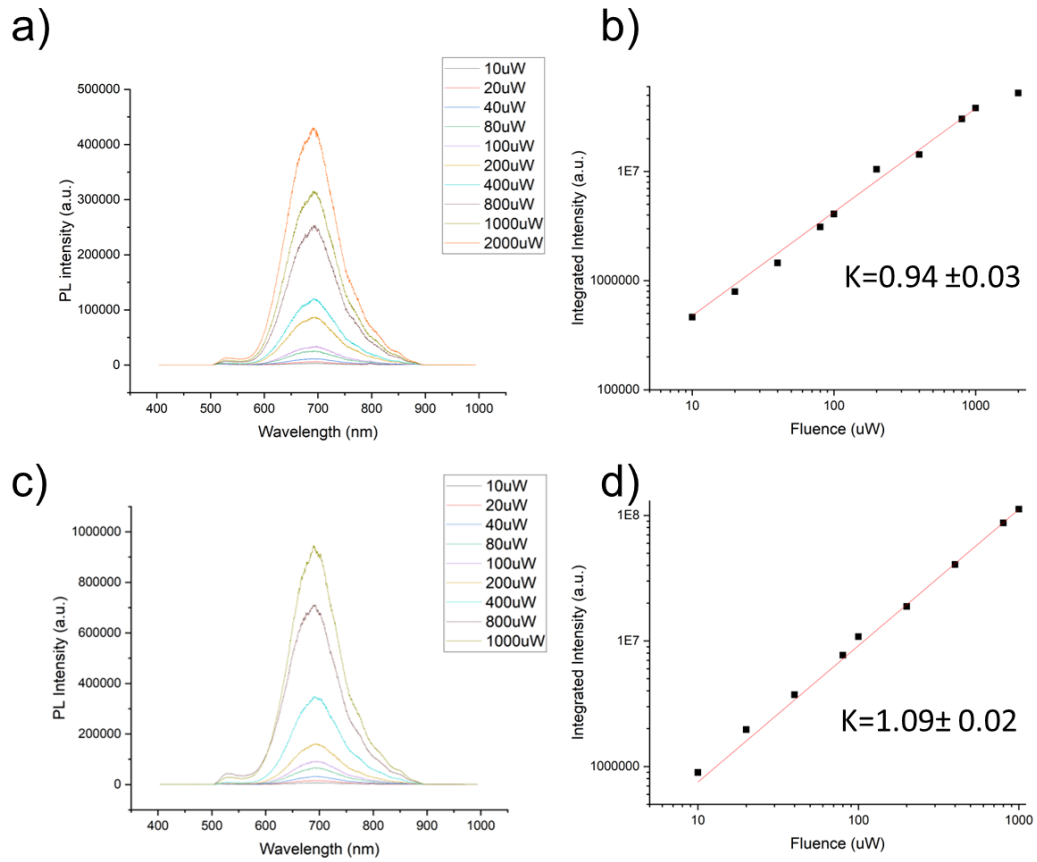

Figure 31. Fluence dependence of PL of $Cs_3Bi_2I_9$ (top) and $Cs_3Sb_2I_9$ (bottom)

In semiconductors, assuming that excitation power P is approximately proportional to the injected carrier density for a fixed spot size of pumping laser, the PL intensity (I) could be expressed as:

$$I \propto P^K \quad (37)$$

Where K indicates the recombination process. If $K <$ 1, free-to-bound/donor-acceptor pair recombination occurs. If K ~ 1, then the process is an exciton-like transition. If K > 1, free and bound-

exciton emission occurs[205]. Figure 31 shows that both $Cs_3Bi_2I_9$ and $Cs_3Sb_2I_9$ have K ~ 1 and therefore are dominated by exciton emission.

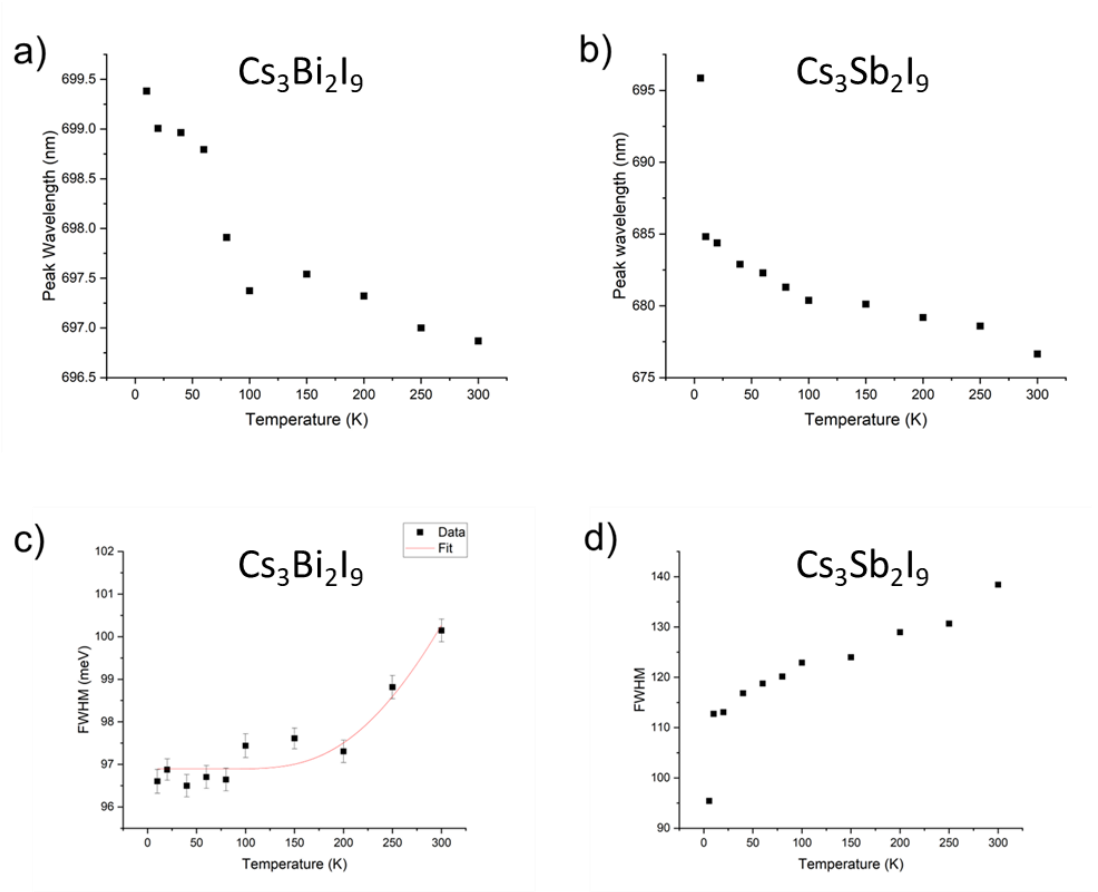

Figure 32. PL peak wavelength vs temperature of a) $Cs_3Bi_2I_9$ and b) $Cs_3Sb_2I_9$ and the FWHM vs temperature plot of c) $Cs_3Bi_2I_9$ and d) $Cs_3Sb_2I_9$

According to literature, the PL spectra of $Cs_3Bi_2I_9$ is comprised of at least four overlapping peaks[196] that do not differ significantly with changes in temperature or fluence. An approximate analysis was made by viewing the central large peak as one single peak at ~696-699 nm. A linear relationship between PL intensity and fluence indicates donor–acceptor pair (DAP) recombination or free-to-bound transition. The PL spectra of $Cs_3Sb_2I_9$ have broad near band-edge emission at ~675-695nm. Although both materials have broad spectra that can be attributed to strong electron–phonon coupling as the charge localization and emission of phonons results in change in photon energy, only the full width at half maximum (FWHM) vs temperature of $Cs_3Bi_2I_9$ follows the strong phonon-coupling model as given by Toyozawa:

$$FWHM(T) = 2.36\sqrt{S}E_{ph}\sqrt{coth\left(\frac{E_{ph}}{2k_BT}\right)} \quad (38)$$

Where S is the Huang-Rhys factor, E_{ph} is the optical phonon energy, and k_B is the Boltzmann constant. The fitting of FWHM vs temperature of $Cs_3Bi_2I_9$ against this equation gave a Huang-Rhys factor of 87.22±2.81, which implies strong electron-phonon coupling in the sample. The $Cs_3Sb_2I_9$ could not be fit with this model. It is possible that this is due to the series of phase transitions at ~80K (as discussed in Section 2.3.3) that previous literature found but could not identify[96] that caused a deviation in FWHM trend.

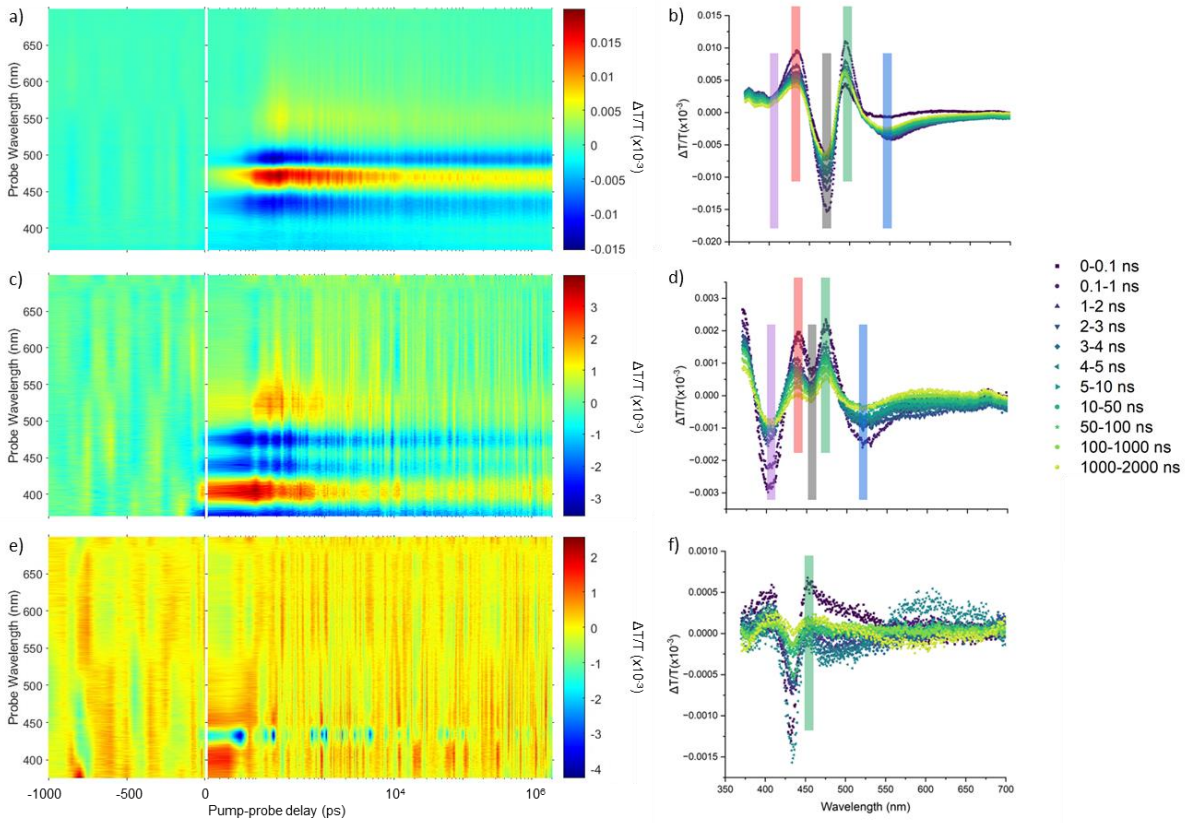

Figure 33. TA Spectra of a)b) $Cs_3Bi_2I_9$, c)d) $Cs_3Sb_2I_9$ and e)f) $Cs_3Bi_2Br_9$ taken with 350 nm pump wavelength and 100 µW fluence

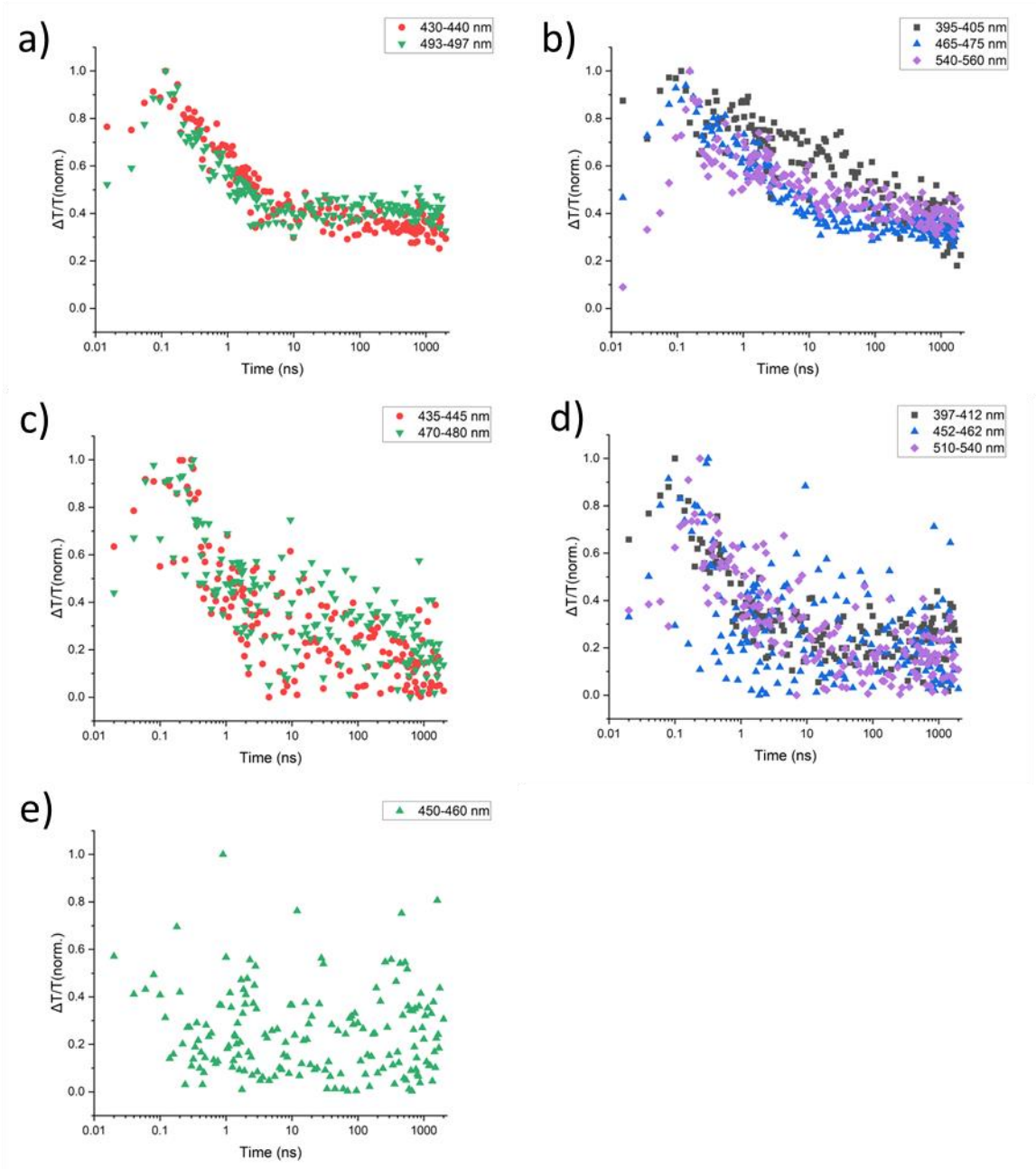

Figure 34. TA kinetics comparison of a) GSB of $Cs_3Bi_2I_9$, b) PIA of $Cs_3Bi_2I_9$, c) GSB of $Cs_3Sb_2I_9$, d) PIA of $Cs_3Sb_2I_9$ and e) GSB of $Cs_3Bi_2Br_9$

To further investigate the nature of excitons in vacancy ordered triple perovskites, transient absorption spectroscopy (TAS) was performed by Dr. Junzhi Ye for $Cs_3Bi_2I_9$, $Cs_3Bi_2Br_9$ and $Cs_3Sb_2I_9$ at 100 µW with spot size of 320 µm and a wavelength λ_{pump} of 350 nm. The resulting fluence was 248.7µJ/cm^2. Attempts were made to perform TAS on $Cs_3Sb_2Br_9$ samples, but beam damage made measurements impossible.

The TA spectra of $Cs_3Bi_2I_9$ and $Cs_3Sb_2I_9$ share very similar features: one broad negative signal at ~530-550 nm, two positive peaks, and a sharp negative signal at higher energy. For $Cs_3Bi_2I_9$ the sharp photo-

bleach peak matches the steady-state absorption peak from the UV-Vis and PDS data, and therefore is assigned to ground state bleach (GSB) from band-to-band transition. The second photo bleach at ~ 430 nm corresponds to the second absorption onset in the steady-state spectrum and is likely due to transition to the higher energy sub-bands, but a trap state is also likely. The broad negative photo absorption (PA) at 500 nm is assigned to excited-state absorption (ESA) and is characteristic of band-edge exciton formation during hot-exciton relaxation[206]. The sharp PA peak is attributed to the absorption arising from the lowest exciton state. The two peaks of $Cs_3Sb_2I_9$ at ~470 and ~450 nm are assigned to band-to-band transition and second excitonic transition/trap bleach respectively. The large dip at 400 nm is assigned to be a continuation of the 500 nm broad ESA signal.

The positive peak at 430 nm for $Cs_3Bi_2Br_9$ is assigned to band-to-band transition. The broad PA appears to be mostly cancelled out by the small positive signal at ~470 nm which correlates to the indirect bandgap of $Cs_3Bi_2Br_9$ of ~2.6 eV. The sharp negative signal that is attributed to discrete exciton transition is notably absent in the spectra.

4.5 Conclusions and future work

In this chapter, I investigated the structural and electronic dimensionality of vacancy-ordered triple perovskites ($Cs_3B_2X_9$, where B = Bi^{3+} or Sb^{3+} and X = I^- or Br^-) and their impact on carrier localization, excitonic behaviour, and optoelectronic properties.

XRD and Raman spectroscopy confirm that the substitution of smaller cations (Br^- for I^- and Sb^{3+} for Bi^{3+}) successfully tunes the structural dimensionality from 0D in $Cs_3Bi_2I_9$ and $Cs_3Sb_2I_9$ to 2D in $Cs_3Bi_2Br_9$ and $Cs_3Sb_2Br_9$. This transition from isolated face-sharing octahedra to corner-sharing octahedral layers is expected to affect electronic dimensionality and carrier mobility. However, achieving pure phase materials for mixed halide compositions remains challenging. Precursor solution concentrations need to be as low as 0.25mol/L for consistent phase pure thin films to be produced.

UV-Vis and photothermal deflection spectroscopy (PDS) revealed presence of excitonic peaks in the absorption spectra of the Bi-based compounds, but not in the Sb-based compounds, suggesting stronger exciton localization around the Bi^{3+} sites, attributed to higher exciton binding energies (278–300 meV). However, PL of all samples displayed broad emission spectra with significant Stokes shifts, indicating

presence of excitons. The lack of temperature dependence in PL lifetimes of $Cs_3Bi_2I_9$ and $Cs_3Sb_2I_9$ confirms immediate formation of STEs in these 0D electronic structures, with no energy barrier for STE formation. The similar behaviour of both materials suggests that the change in pnictogen species does not significantly alter self-trapping tendencies in the 0D compounds despite lack of excitonic peak in the absorption spectra of Sb-based compounds.

Further studies into the exciton presence in bromide compounds are recommended as temperature-dependent PL measurements were not completed due to time constraints. This will provide comparison and insight into the STE and possible sub-bandgap excitation mechanisms of the vacancy ordered perovskites.

Furthermore, density functional theory (DFT) and molecular dynamics simulations could assist in confirming the strength of acoustic phonon coupling and carrier mobility and self-trapping are affected. Although computational studies exist in literature, a combined study of all four materials is lacking.

Addressing these areas will enable a more complete understanding of the relationship between dimensionality and charge-carrier behaviour in vacancy-ordered triple perovskites could potentially lead to finding methods of suppressing STE to achieve better carrier mobilities and hence improve photovoltaic device performance.

5 $AgBiI_4$ thin films for indoor photovoltaics

Silver bismuth halides have gained interest for indoor PV (IPV) applications. In 2016, Turkeyvch et al. reported a 5.17% power conversion efficiency (PCE) for $AgBiI_4$ IPV measured under 1000 lux white light emitting diode (WLED) illumination[148]. Furthermore, calculations of the theoretical optical limit in efficiency (i.e., spectroscopic limited maximum efficiency (SLME)) was more than 20% under AM 1.5G illumination, and up to 56.2% under 1000 lux white light emitting diode illumination for the related compound, Ag_3BiI_6 based on its measured absorption spectra, and other Ag-Bi-I compounds are expected to have similar SLMEs because of their similar absorption profiles[11]. However, reaching these optical limits in performance requires firstly devising synthesis routes to achieve pinhole-free thin films, since a high shunt resistance is crucial for operation under indoor light conditions. In this chapter, I investigate this in detail for the case of $AgBiI_4$. I firstly employ experimental approaches to control the morphology of solution-processed films, before feeding this morphological information to a deep neural network model to independently identify the optimal set of processing parameters. Having achieved dense and compact films, I find that $AgBiI_4$ have poor IPV performance, suggesting that these materials are limited by fundamental factors that restrict the efficiency of charge-carrier extraction and quasi-Fermi level splitting.

5.1. Introduction

As discussed in Section 2.3.6, the Ag-Bi-I family is comprised of several materials, with different structures, from defect-spinel (Ag-poor compounds) to $CdCl_2$ ($AgBiI_4$) and $NaVO_2$ structured materials (Ag-rich compounds). $AgBiI_4$ itself could adopt a defect-spinel or $CdCl_2$ structure. The parameter space can become extremely broad if I consider multiple fabrication methods and stoichiometries. I therefore focus specifically on spin-coated $AgBiI_4$ thin films. This is because just before starting my project, a report appeared on $AgBiI_4$ IPVs with 5.17% PCE under white LED illumination of 1000 and 500 lux[139]. Since then, to my knowledge, there have been no improvements in performance, with other reports achieving lower efficiencies as shown in Table 2 in Section 2.3.7[180-184]. It is therefore critical to understand whether $AgBiI_4$ is limited by poor morphology, or more fundamental factors. Spin-coating is also the most commonly used method in the early investigation of Ag-Bi-I compounds (as shown in Table 22 in Section 2.3.7) because of its simplicity and tunability.

In spin coating, the morphology of the films is determined by supersaturation, Ostwald ripening and grain growth, and surface energy of the substrate, among many other factors. These are influenced by 1) the materials films are grown onto, 2) whether there is any surface treatment, 3) the use of antisolvents and when these are deployed, 4) the temperature during spin coating, and 5) the post-annealing process. A systematic investigation of these factors on the morphology of $AgBiI_4$ is necessary in order to obtain compact thin films.

To test these factors, I made use of i) antisolvent dripping during film spinning, investigating the polarity of the antisolvent used, ii) comparing cold-casting vs. hot casting, and iii) DMSO: DMF solvent ratio. Having obtained compact thin films, the device performance as IPVs was investigated.

Furthermore, I compared these traditional human-driven efforts with the use of deep neural networks to identify the optimal set of parameters. SEM images of $AgBiI_4$ thin films produced with varying parameters were fed into a machine learning model, which then identified films with best morphology and was then trained to identify parameters that gave better morphology. Sections 5.2 – 5.4 detail human-driven experimentation, while Section 5.6 details the use of machine learning.

5.2 Phase purity and stability of $AgBiI_4$ films

$AgBiI_4$ thin films were synthesized as per the solution-processed method described in Section 3.1. XRD fitting as shown in Figure 35 confirms that the $AgBiI_4$ thin films made via this method has a $R\bar{3}mH$ space group, which has a $CdCl_2$-type structure, rather than a 3D defect spinel structure ($Fd\bar{3}m$). This structure is 2D, with layers alternating between having all octahedral holes occupied with Ag^+ and Bi^{3+}, versus none of the octahedral holes occupied. There is cation disorder in this structure, in that the Ag^+ and Bi^{3+} have very similar ionic radii (129 and 117 pm respectively[153]), and therefore occupy the same crystallographic lattice site. The small, unfitted peak ~12° in Figure 35 is a spectral line.

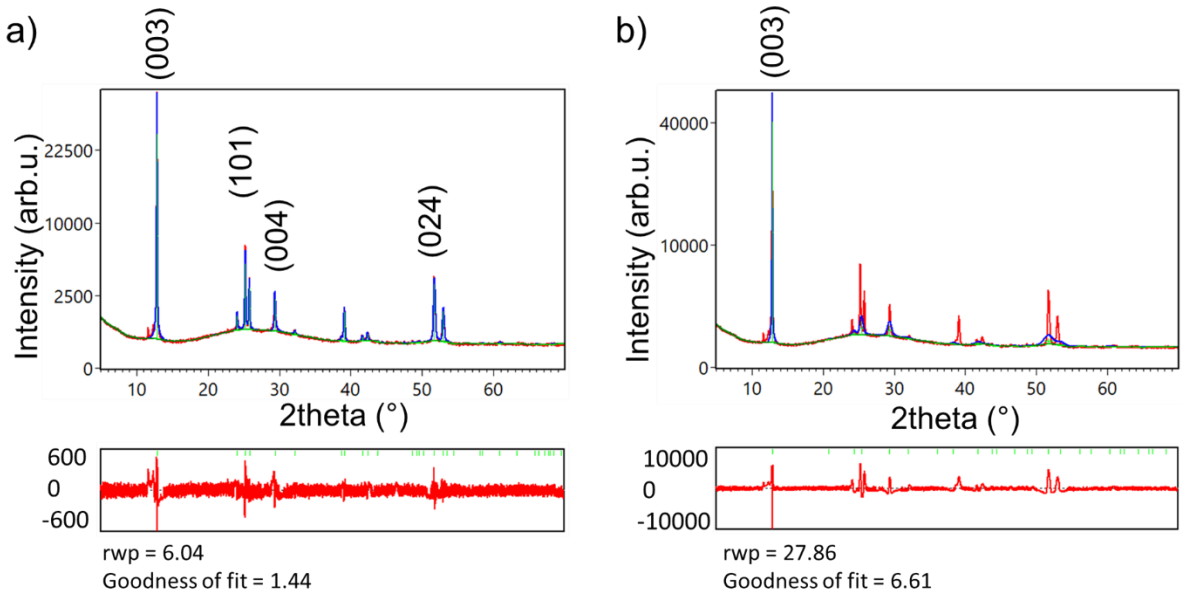

Figure 35. XRD of $AgBiI_4$ fitted against a) $R\bar{3}mH$ reference and b) $Fd\bar{3}m$ reference.

Stability tests were performed on $AgBiI_4$ thin films. One was exposed to ambient air directly while the other was coated with a layer of spiro-OMeTAD . Over three weeks both samples, under ambient humidity and temperature but no illumination, suffered heavy degradation. Visually the films turned from black to light brown, and SEM images (Figure 36) shows the morphology significantly changing. The original crystalline micro-islands shrank over time, forming larger voids on the substrate. XRD patterns as shown in Figure 37 show the presence of BiOI and BiI_3 impurities growing stronger over time, which suggests that the degradation is due to oxidation of the thin film. This differs from previous literature that reported stable $AgBiI_4$ films[152, 163]. However, the starting morphology is not defect-free

and voids may act as entry points for oxygen and moisture . It is possible that if voids were not present in morphology, then devices may be more stable.

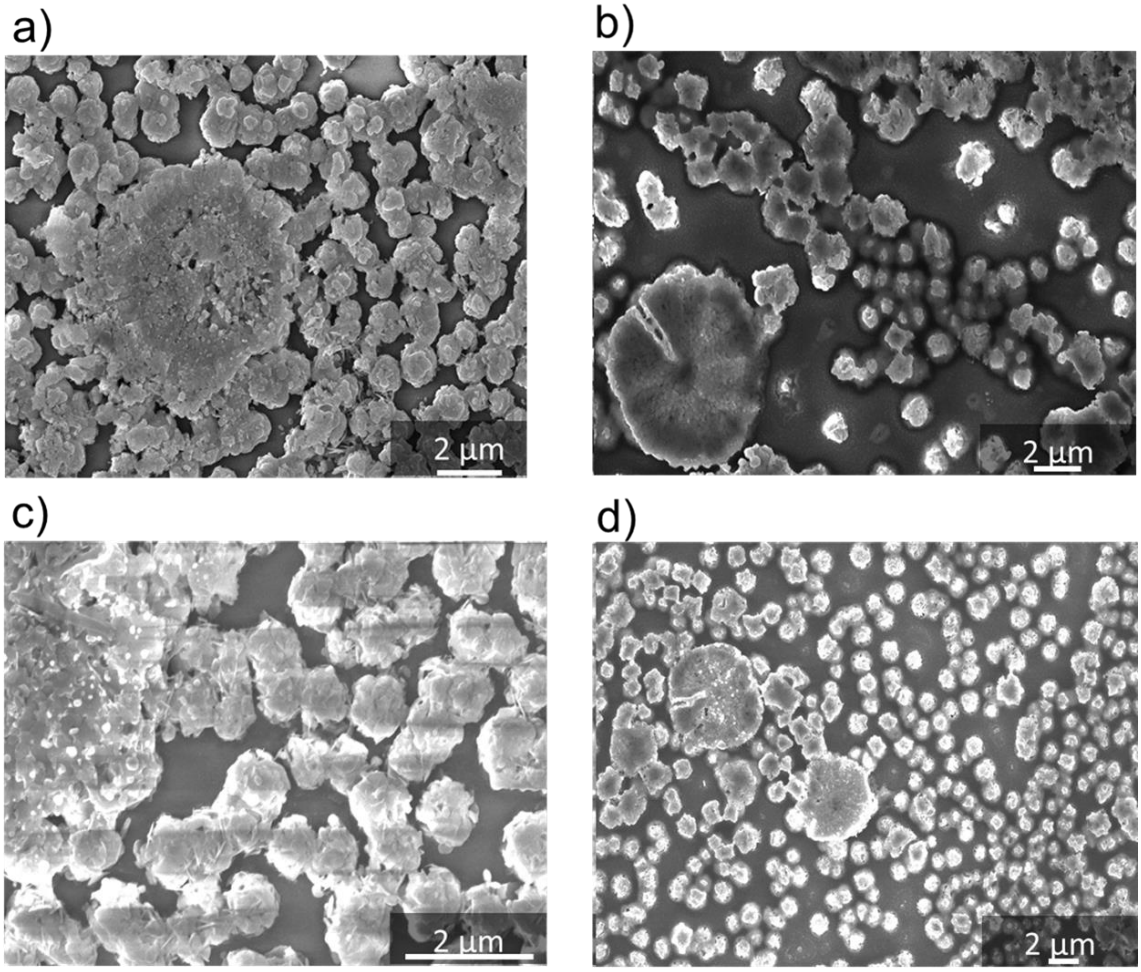

Figure 36. SEM of $AgBiI_4$ a) uncoated on day of synthesis, b) uncoated 23 days after synthesis, c) coated with spiro on day of synthesis, and d) coated with spiro 23 days after synthesis.

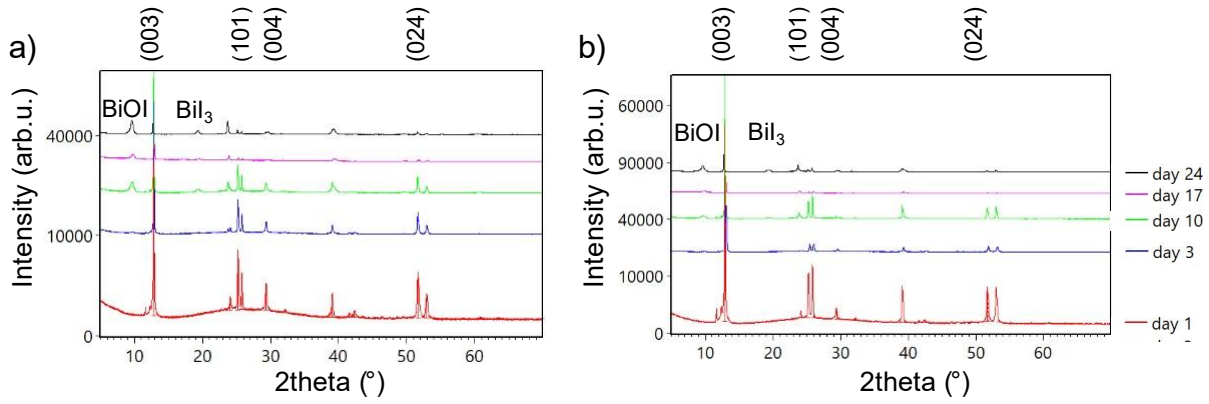

Figure 37. XRD of a) uncoated $AgBiI_4$ left in ambient air b) $AgBiI_4$ coated with spiro-OMeTAD left in ambient air.

5.3 Optimisation of thin film morphology

Various parameters in the fabrication of $AgBiI_4$ thin films were tuned to optimise thin film morphology.

5.3.1. Hot casting

Hot casting method was investigated at various temperatures. Although reports of morphology improvement with this method have been made previously[143, 148], the reason for temperature choices were not given. Clean substrates and $AgBiI_4$ solution were both heated from room temperature to 150 °C at 10 °C intervals before spin coating. The results as shown by Figure 38 indicated that the best temperature for $AgBiI_4$ fabrication is in the 110 - 120 °C range. The supersaturation due to the high temperature of the solution along with the high temperature of the substrate leads to rapid nucleation and thus lowers the defect density of the thin film. At temperatures below 110 °C, the grain sizes are noticeably smaller and there is a greater presence of pinholes. At temperatures above 120 °C, it was observed that the solution underwent rapid evaporation during spin coating and underwent annealing during the spin-coating step due to the high temperature. Bright impurities could be seen on these samples. However, it should be noted that hot casting is heavily dependent on the time taken for precursor solution to be deposited on substrate after both are taken off the heat source. As shown in Figures 38 and 39, the hot casting process is difficult to be reliably reproduced by hand and batch to batch variation exists, especially at high temperatures. This difference is due to the variation of transfer time of solution and substrate from hotplate to spin coater combined with their fast-cooling rate of the resulting in a large enough variation of their actual, undeterminable temperature at start of spin coating to lead to a difference in morphology,

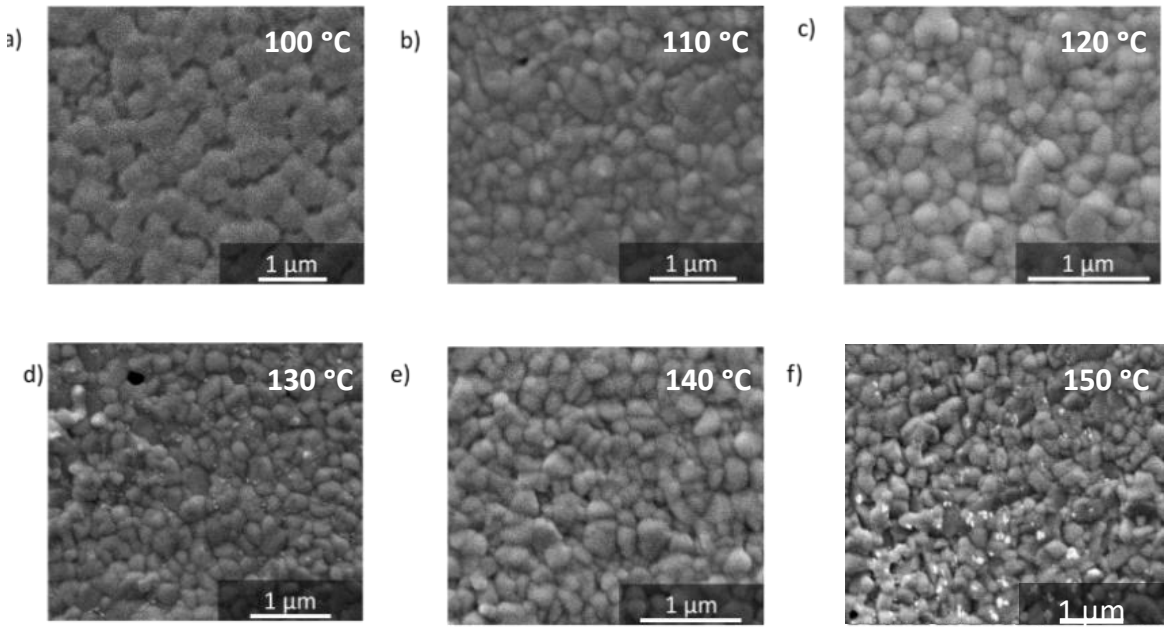

Figure 38.. SEM images of $AgBiI_4$ synthesized with hot-casting method at a) 100 °C b) 110 °C, c) 120 °C, d) 130 °C, e) 140 °C and f) 150 °C. The temperatures specified are the set temperature of the hotpate for both the substrate and precursor solution prior to spin coating

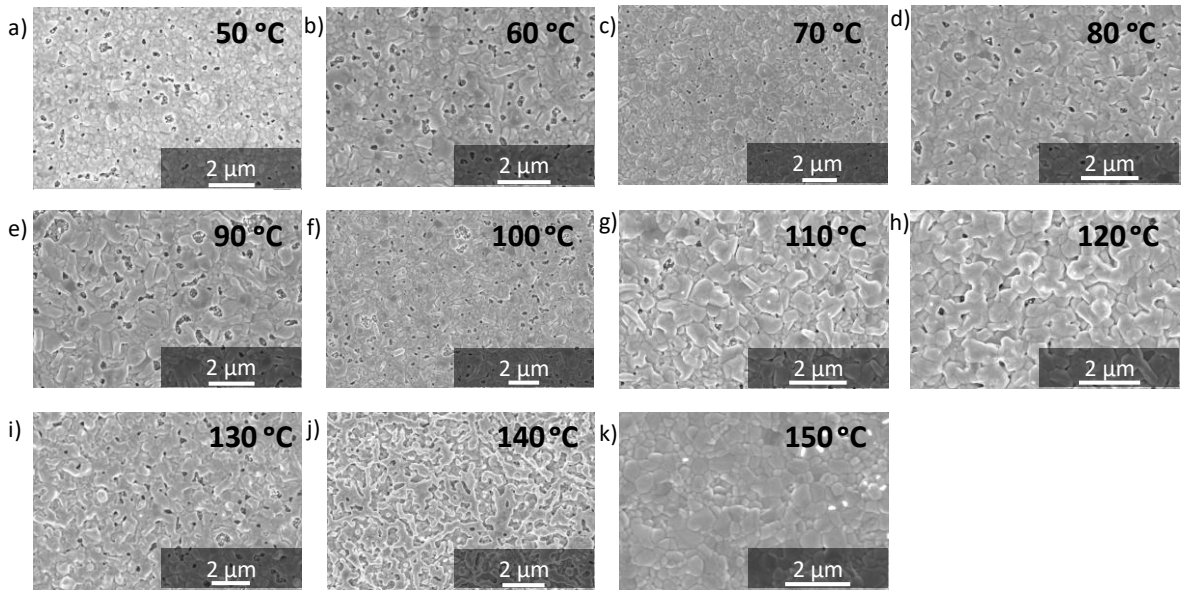

Figure 39. SEM images of $AgBiI_4$ synthesized with hot-casting methods, Labelled temperatures are that of the hotplate for both the substrate and precursor solution prior to spin coating

5.3.2 Anti-solvent treatment

IPA, chlorobenzene and toluene were investigated as potential anti-solvents to improve $AgBiI_4$ morphology as shown in Figure 40. These antisolvent were dropped onto the spinning film during thin film deposition by spin-coating. By dropping these antisolvents, the original 'good' solvent that highly solubilised the precursors were quickly replaced with the anti-solvent, which has substantially lower solubility for the precursors, rapidly increasing the supersaturation of the precursors. The polarity of the anti-solvents may have a small effect on the morphology of the thin film. The antisolvents were chosen due to their low polarities[207], as shown in Table 6 along with that of DMSO and DMF solvents, ensure poor solubility. The results, as shown in Figure 40, show that the chlorobenzene- treated samples had the best morphology, with no pinholes observed.

Table 6. Properties of solvents used to dissolve the original precursors (DMSO and DMF) and antisolvents [208-210]

Solvent	Polarity index	Dipole moment (D)	Gutmann number (kJ/mol)
DMSO	7.2	3.96	125
DMF	6.4	3.74	111
IPA	4	1.66	21.1
Chlorobenzene	2.7	1.5	3.3
Toluene	2.4	0.31	0.1

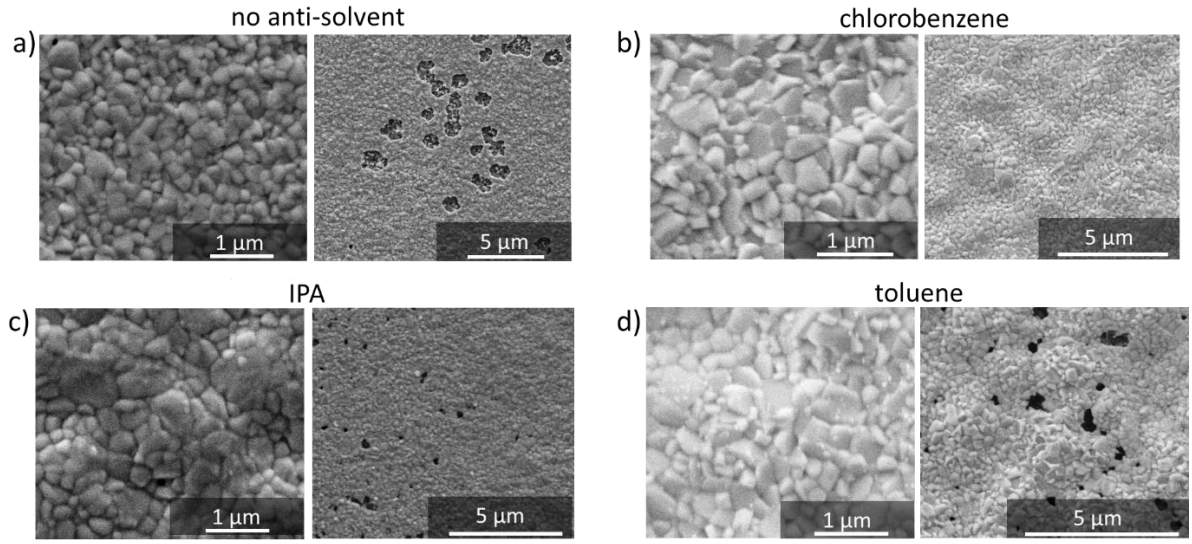

Figure 40. SEM images of $AgBiI_4$ synthesized with hot-casting method at 110 °C with anti-solvent dripping at 22s. a) no anti-solvent used, b) chlorobenzene, c) IPA, d) toluene

5.3.3 Solvent engineering

Previous literature[211] has reported improvement in thin film morphology via solvent engineering by mixing DMF with DMSO. Zhang *et al.*[211] found that DMF increases rate of crystallisation due to extremely fast volatilization and lower solubility compared to DMSO, and by using a mixture of DMSO and DMF as solvent, the crystallisation rate could be varied and hence result in different morphology. Therefore, $AgBiI_4$ solutions dissolved in pure DMSO, 10:1, 5:1, 3:1 and 1:1 DMSO:DMF ratio, spin coated with and without antisolvent treatment were investigated, and the thin film morphology produced are shown in Figure 41. It is apparent that without anti-solvent treatment, solutions containing more DMF such as 1:1 and 3:1 DMSO:DMF ratios gave better morphologies. The 1:1 DMSO:DMF sample also has significantly smaller grain sizes, which agrees with aforementioned literature that DMF enables faster crystallisation compared to DMSO. However, films with antisolvent treatment all appear to be similar except for 10:1 DMSO:DMF ratio. Given that there is no discernible trend, this sample morphology is put down to batch-to-batch variation. It is possible that the anti-solvent is introduced too late into the spin-coating process and therefore disrupted the rapid crystallisation that was already happening in the DMF-containing samples, therefore negating its effects entirely.

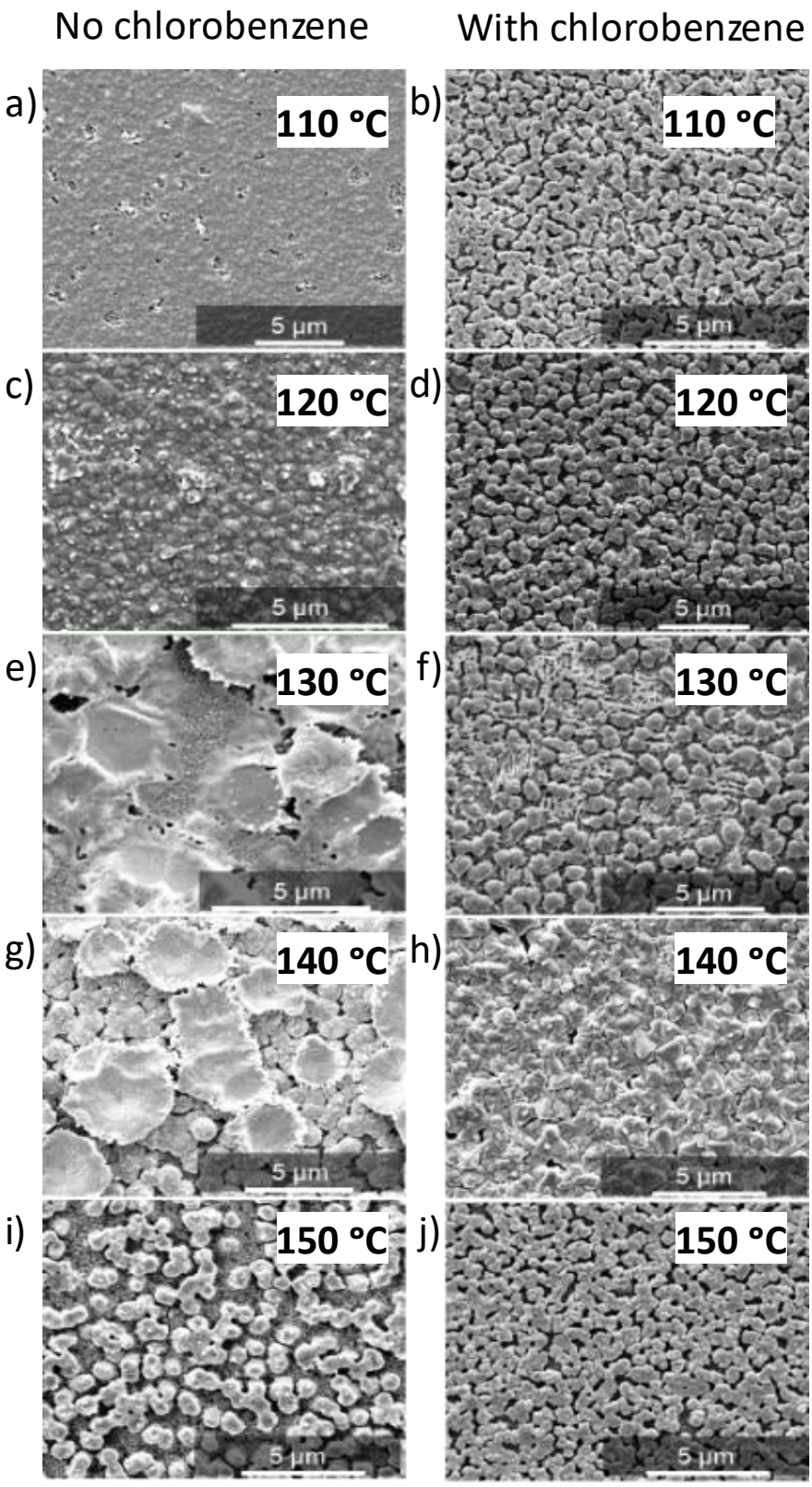

Figure 41. SEM images of $AgBiI_4$ synthesized with hot-casting method at 110 °C with a DMSO vs DMF ratio of a) 1:1 b) 1:1 with chlorobenzene dripping at 22s c) 3:1 d) 3:1 with chlorobenzene dripping at 22s e) 5:1 f) 5:1 with chlorobenzene dripping at 22s g) 10:1 h) 10:1 with chlorobenzene dripping at 22s i) pure DMSO and j) pure DMSO with chlorobenzene dripping at 22s

5.4 Photovoltaic development

Having investigated the effects of thin film processing parameters on the properties of the thin films, $AgBiI_4$ devices were made and tested for photovoltaic performance under 1 sun illumination. To account for hysteresis, the device performance was measured through forward and reverse sweeps.

Firstly, the effect of antisolvents was investigated. Devices made with chlorobenzene, toluene and IPA treatment was compared against device without any antisolvent treatment. The results are as shown in Figure 42. The device with best performance was synthesized using chlorobenzene antisolvent, which corresponded to Figure 40 where chlorobenzene dripping gave the best thin film morphology.

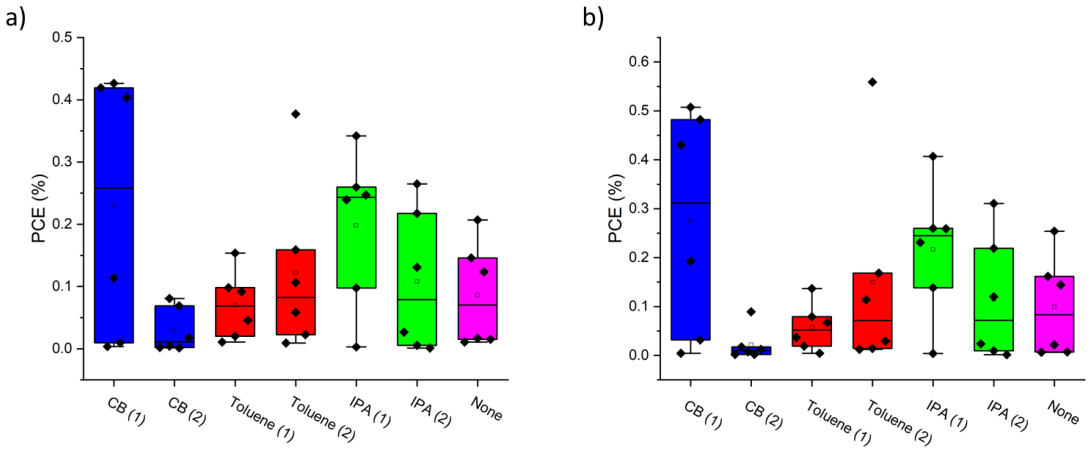

Figure 42. PCE of $AgBiI_4$ devices synthesized with different antisolvent treatments under a) forward bias and b) reverse bias

Then $AgBiI_4$ devices were spin coated with different volumes of chlorobenzene (300µL – 2mL). It should be noted that Figure 42 ab) and cd) were done in different batches and hence there is a variation in PCE. In both batches the devices with 1mL chlorobenzene gave the best PCEs.

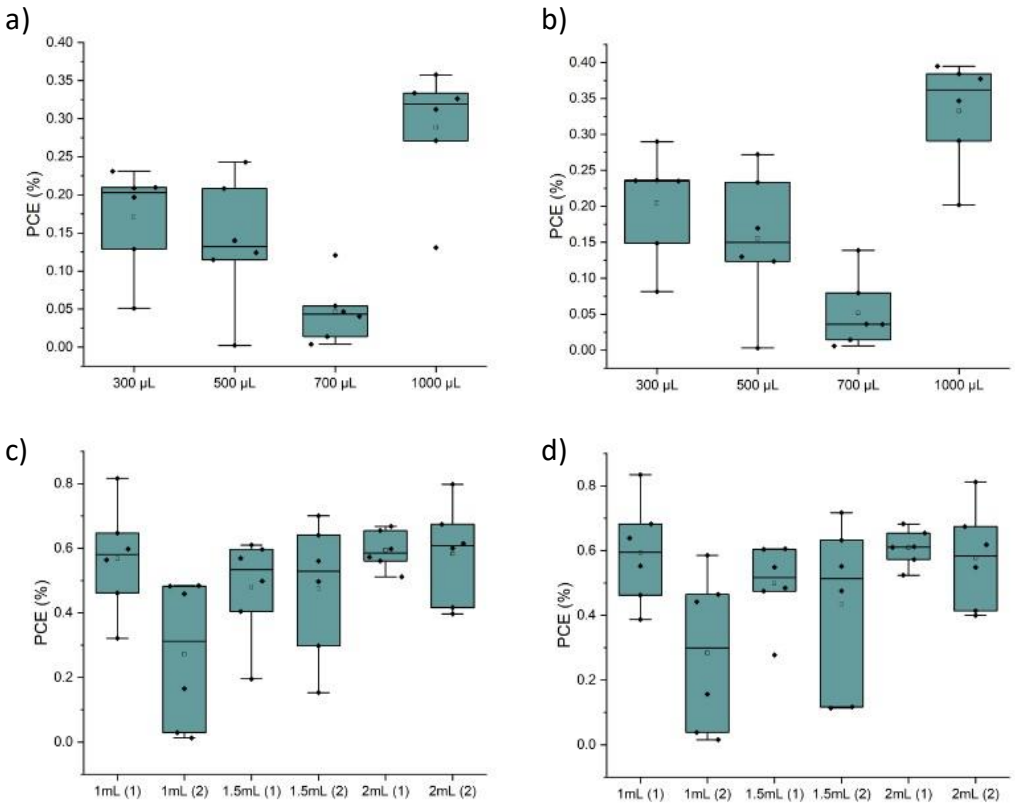

Figure 43. Forwards a) c) and backwards b) d) PCE of $AgBiI_4$ devices spin coated with different volumes of chlorobenzene antisolvent dripping

Devices made with different ratios of DMSO:DMF solvents were tested to see if performance would be impacted. Unable to draw conclusion due to overlap of device performance. This possible due to devices being made with antisolvent treatment, as shown in Figure 41, gave similar morphology.

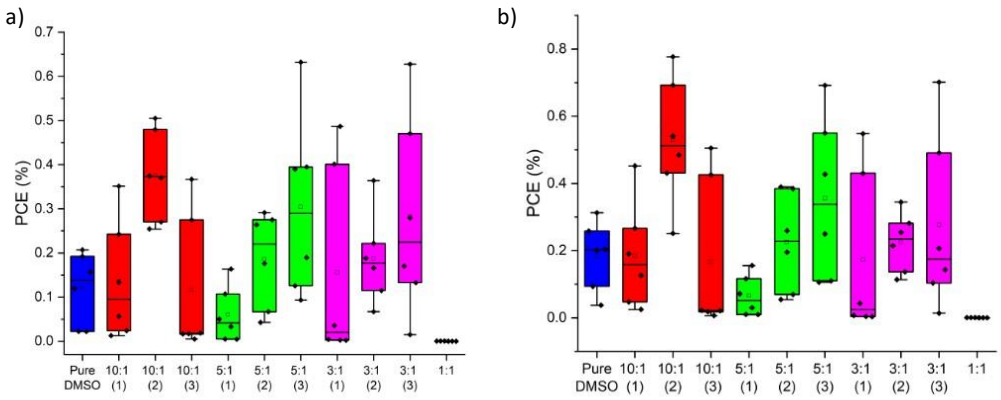

Figure 44. PCE of $AgBiI_4$ devices dissolved in different DMSO:DMF ratios under a) forward bias and b) reverse bias

The best working devices had a PCE of 0.83% and had the parameter of: 35 wt% $AgBiI_4$ dissolved in pure DMSO, heated to 110 °C prior to spin coating of 1000 rpm for 2s then 4000 rpm for 30s, with chlorobenzene antisolvent treatment 20s into the second spin coating step and annealed at 150 °C for half an hour. This corresponded to a pinhole free morphology from Figure 40. As can be in in Figure 45, the I-V curves of the best working devices showed no significant signs of shunting, whereas the failed devices with 0% PCE show complete shunt. Therefore, the low PCE of the best working devices cannot be attributed to shunting and a more intrinsic limitation exists for device performance.

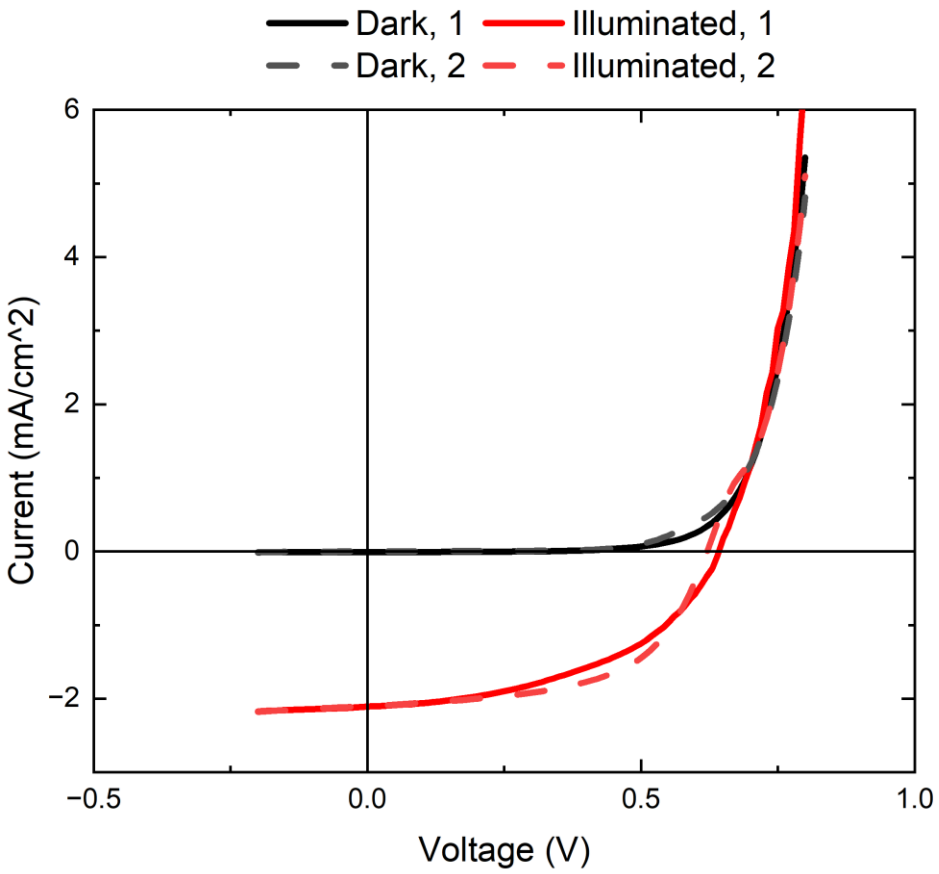

Figure 45. Dark and illuminated IV curves of best $AgBiI_4$ device under forward (solid line) and reverse bias (dashed line)

5.5 Use of machine learning to understand and predict effect of processing conditions on thin film morphology

Machine learning was employed to a) find set of parameters from the previous data that gave the best morphology and b) extrapolate possible parameters that may lead to improved thin film morphology. As described in Section 3.3, two machine learning models were used to find the best parameters for $AgBiI_4$ synthesis, Reinforcement Learning (RL) and Random Forest (RF). For RL, its core mechanism is directly looking up selected parameter combinations in the dataset and calculating rewards based on defect coverage percentage. To enable extrapolation, hot casting temperature was made into a continuous variable from 25 – 150 °C with a discretization of 5 °C to be calculated along with each parameter set. The RF model was able to consider squared terms and pairwise interactions between features due to the input of polynomial features and generate feature importance scores, as shown in Figure 46, and thus was able to extrapolate new parameters outside of given dataset (temperature was made into a continuous variable from 25 – 150 °C with a discretization of 5 °C). It individually optimizes each feature as compared to RF which looks at the parameter set as a whole.

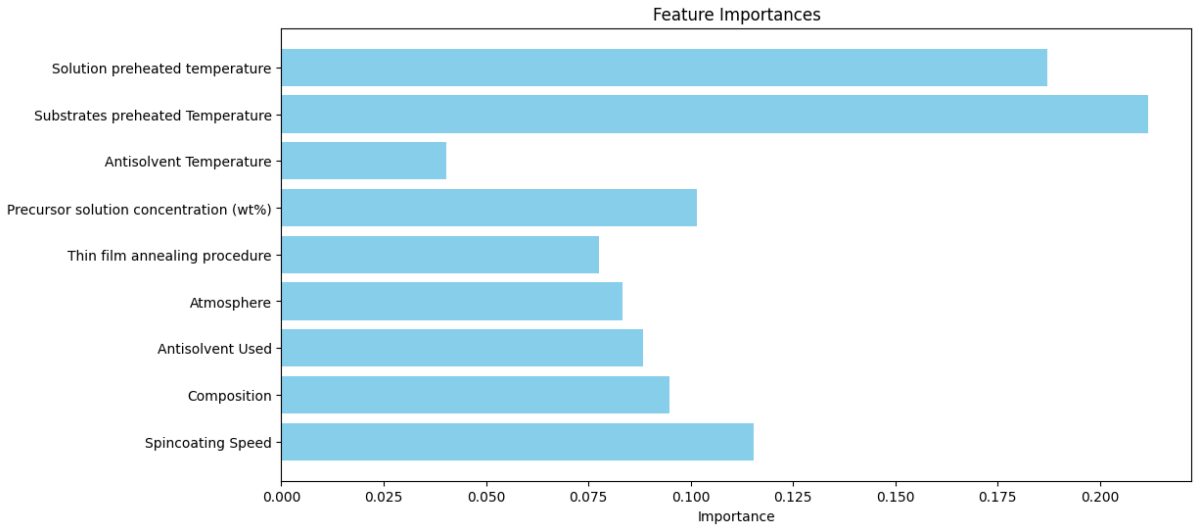

Figure 46. Parameter weights of the RF model

The best processing conditions for optimal morphology of $AgBiI_4$ generated by the RL and the RF model are as shown in Table 7. New samples were made as per the parameters given from the two models and SEM images were taken. As shown in Figure 47, the morphology produced from RL parameters were as expected, whereas the morphology from RF is drastically different. The difference

in morphology is due to the high hot casting temperature of 150 °C given by the RF parameters. At such high temperatures, when the solution is dripped onto the substrate fast enough after removal from hotplate nuclei crystallisation will begin immediately during spin coating, as seen in Figure 47.a. When more time was given for the solution to cool down due to human error, a smoother morphology will form as per Figure 47.b. This batch-to-batch variation was present in the data fed into the machine learning model, but the AI could not account for it due to the model assumption that the optimal parameter settings in the given dataset will generalize into all future settings. Furthermore, it could not capture all possible interactions between each parameter in the dataset, and therefore produced the resulting 150 °C parameter due to its high weight importance and discarded the importance of anti-solvent treatment.

Table 7. Table showing best parameters predicted by the RL and RF model

Model	Spin Coating Speed	Antisolvent Used	Thin film annealing procedure	Precursor solution concentration (wt%)	Antisolvent Temperature (° C)	Hot casting temperature (° C)
RL	1000 rpm 2s, 4000rpm 40s	CB	150 °C for 30 mins	34	25	100
RF	6000 rpm 30s	NA	150 °C for 30 mins	35	NA	150

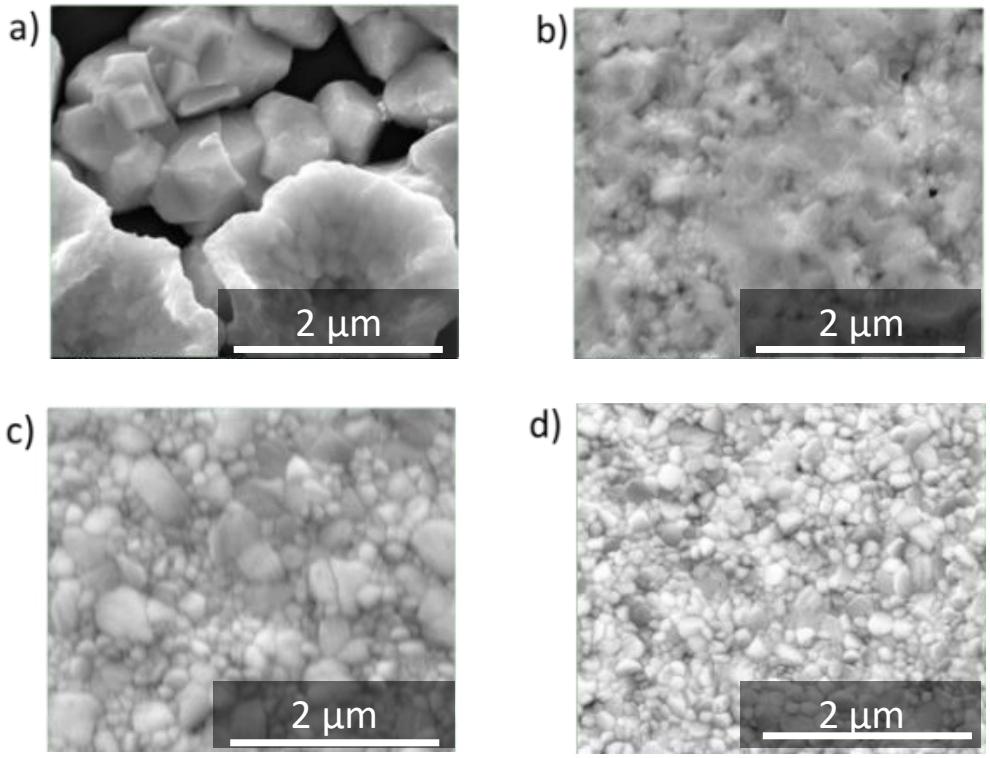

Figure 47. SEM image of samples made according to a,b) RF predicted parameters and c,d) RL predicted parameters, as specified in Table 7 above.

Conclusions and future work

$AgBiI_4$ morphology can be improved by two key parameters: hot casting and antisolvent treatment. Hot casting induces supersaturation in the solution, which results in rapid nucleation and hence lowers defect density. However, at high temperatures (> 120 °C) clustering may appear due to rapid crystal growth during spin coating step before nuclei could be spread out across substrate. Hence, the cooling time of solution between removal from hotplate and spin coating is crucial for good thin film morphology at such temperatures but is hard to quantity and prone to batch-to-batch variation due to human error. Antisolvent treatment induces rapid nucleation via solvent removal. Nucleation centres are given time to spread out during spin-coating step before anti-solvent treatment, and hence give more consistent results. However, batch to batch variation remains high at high hot casting temperatures due to the fast cooling rate combined with human fallibility in the synthesis process. The best parameters found by machine learning was spin coating a 34 wt% $AgBiI_4$ solution onto substrate (both pre-heated to 100 °C) at 1000 rpm for 2s, then 4000 rpm for 30s with 1mL chlorobenzene dripping 20s into the second spin-coating step. However, despite achieving compact film morphology, the device efficiency

of $AgBiI_4$ under 1 sun illumination remains low (<1%). Investigations into the nature of charge-carriers and charge-carrier transport to identify possible intrinsic limiting factors such as carrier localisation is needed to produce viable photovoltaic devices.

On the machine learning side, current models can be used to objectively judge optimal morphology, but more training could be done to extrapolate better synthesis parameters. The RL model gives accurate results but is limited by the need of a large database from experimental to find the true optimum parameters which is both time and money consuming. The RF model shows promise, but needs improvement into recognising and accounting for batch-to-batch variation and how different parameters are weighed when producing parameters for morphology optimisation.

6 Overall conclusions and future areas of research

This thesis has provided a detailed exploration of novel halide-based materials, with a focus on silver-bismuth iodides for indoor photovoltaics (IPVs) and vacancy-ordered triple perovskites. Through extensive experimentation and analysis, key insights into the structural, morphological, and electronic properties of these materials were obtained, revealing their potential and limitations for photovoltaic applications.

The investigation into vacancy-ordered triple perovskites, showed the presence of excitons in iodide-based compounds and carrier-phonon coupling in $Cs_3Bi_2I_9$ but there is not enough data currently to determine presence of carrier-phonon coupling in $Cs_3Sbi_2I_9$. However, the large Stokes shift suggest the possibility of self-trapping occurring in all four compositions. Therefore, temperature dependent PL should be carried out on the bromide-based compounds to check for presence of carrier-phonon coupling. If STEs also exist in the bromide-based compounds, research into overcoming the phenomenon should be done. Given that carrier-phonon coupling is heavily influenced by lattice structure, investigations may be done on changing 2D layer thickness to see if carrier localisation could be affected. Furthermore, although phase pure mixed-halide vacancy ordered triple perovskites were unable to be produced, it is possible that the lattice mismatch will have interesting effects on phonon coupling. It may also be beneficial to extend the study of vacancy ordered triple perovskites to other applications such as light-emitting diodes (LEDs) or photodetectors, where excitonic behaviour or self-trapping may prove beneficial rather than detrimental.

The investigation into $AgBiI_4$ revealed that the thin film morphology is highly sensitive to the crystallisation rate of nuclei during spin-coating. A set of synthesis parameters was found to give consistent pinhole free morphology, but resulting devices still show low efficiencies, and my analysis of the device performance indicates that these are not limited by shunting. My work therefore shows that future efforts should focus on understanding what factors could be limiting charge-carrier transport in these materials. DFT calculations could be performed to determine the exciton binding energy for Ag-Bi-I compounds to see if a high exciton binding energy is limiting carrier transport. If the exciton binding energy is indeed high, investigation into minimising charge transport lengths via extremely thin

absorber device structure or heterojunctions could be made to improve device efficiency. Ultrafast charge-carrier localisation in Ag-Bi-I compounds observed by Lal *et al.*[212] could also be possible reason for low efficiency, and further research into reducing localisation via increasing electronic dimensionality could reduce this phenomenon. Research into scalable synthesis techniques such slot-die coating or chemical vapour deposition may reduce the effect of human error and improve device morphology reproducibility.

Machine learning has demonstrated its ability to extrapolate optimal parameters for synthesis, and it was found that more continuous variables gave better results for extrapolation. The RL model was only able to extrapolate from continuous variables and analysed the non-continuous parameters in the sets that there were given. The model could be improved further with investigation into improving ability to comparing results for non-continuous variables. The RF model did not work as well as the RL model due to its complexity in trying to weigh all parameters separately but not giving enough importance to samples with defects. More work on how the RF model weighs feature importance as well as its ability to analyse possible relations between different parameters could greatly improve its extrapolation ability.

Appendices

Table 8. XRD fitting values of $AgBiI_4$ left in ambient air over 23 days

SAMPLE	DAYS LEFT IN AIR	R EXPECTED	WEIGHTED R PROFILE	GOODNESS OF FIT
WITHOUT SPIRO-OMETAD LAYER	0	4.213	5.168	1.710
	2	4.111	15.210	3.700
	9	3.489	8.837	2.533
	16	4.671	7.202	1.542
	23	4.308	6.986	1.622
WITH SPIRO-OMETAD LAYER	0	3.611	8.993	2.490
	2	4.226	9.329	2.207
	9	3.034	14.407	4.749
	16	4.596	7.200	1.567
	23	3.881	8.433	2.173

a)

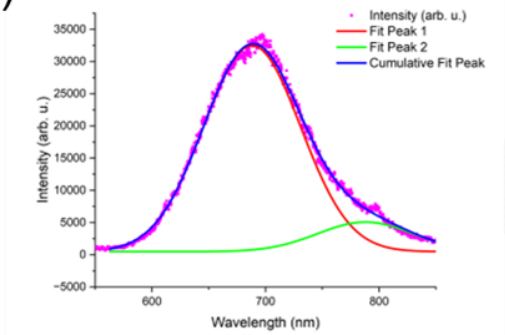
Intensity (arb. u.)
Fit Peak 1
Fit Peak 2
Cumulative Fit Peak
Intensity (arb. u.)
Wavelength (nm)

b)

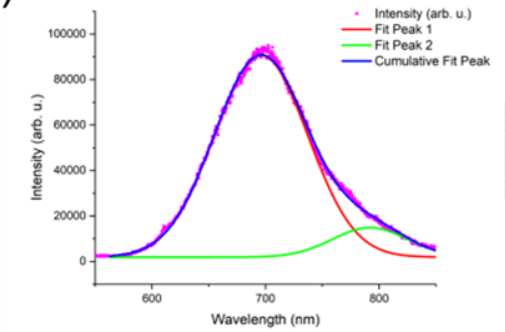
Intensity (arb. u.)
Fit Peak 1
Fit Peak 2
Cumulative Fit Peak
Intensity (arb. u.)
Wavelength (nm)

c)

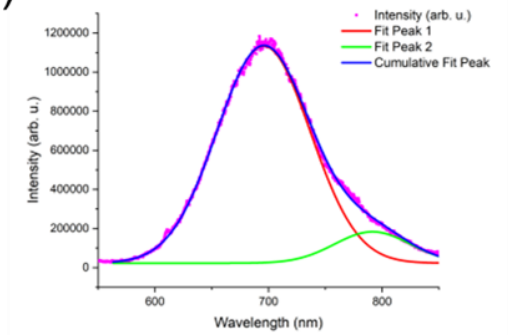
Intensity (arb. u.)
Fit Peak 1
Fit Peak 2
Cumulative Fit Peak
Intensity (arb. u.)
Wavelength (nm)

d)

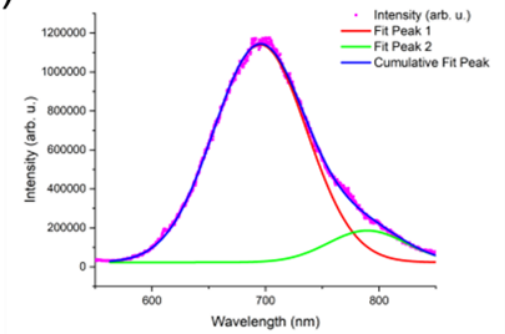
Intensity (arb. u.)
Fit Peak 1
Fit Peak 2
Cumulative Fit Peak
Intensity (arb. u.)
Wavelength (nm)

g)

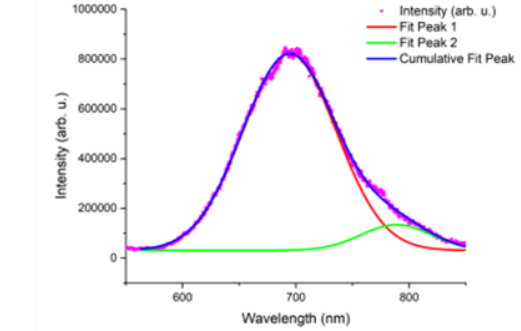
Intensity (arb. u.)
Fit Peak 1
Fit Peak 2
Cumulative Fit Peak
Intensity (arb. u.)
Wavelength (nm)

h)

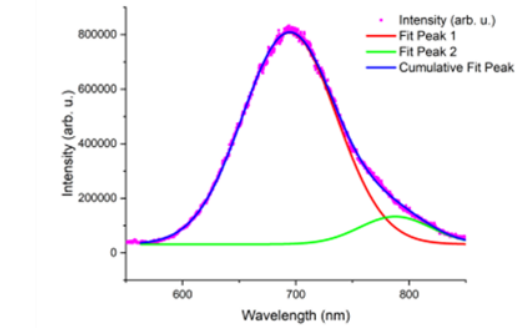
Intensity (arb. u.)
Fit Peak 1
Fit Peak 2
Cumulative Fit Peak
Intensity (arb. u.)
Wavelength (nm)

i)

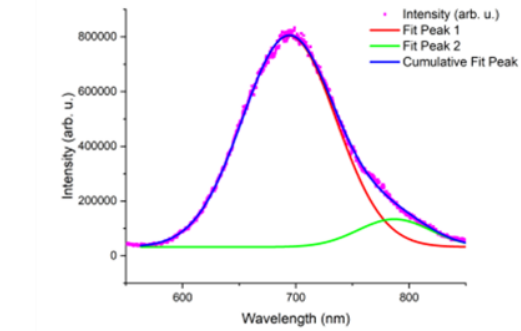
Intensity (arb. u.)
Fit Peak 1
Fit Peak 2
Cumulative Fit Peak
Intensity (arb. u.)
Wavelength (nm)

j)

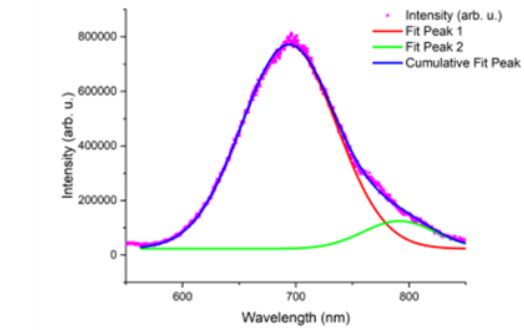
Intensity (arb. u.)
Fit Peak 1
Fit Peak 2
Cumulative Fit Peak
Intensity (arb. u.)
Wavelength (nm)

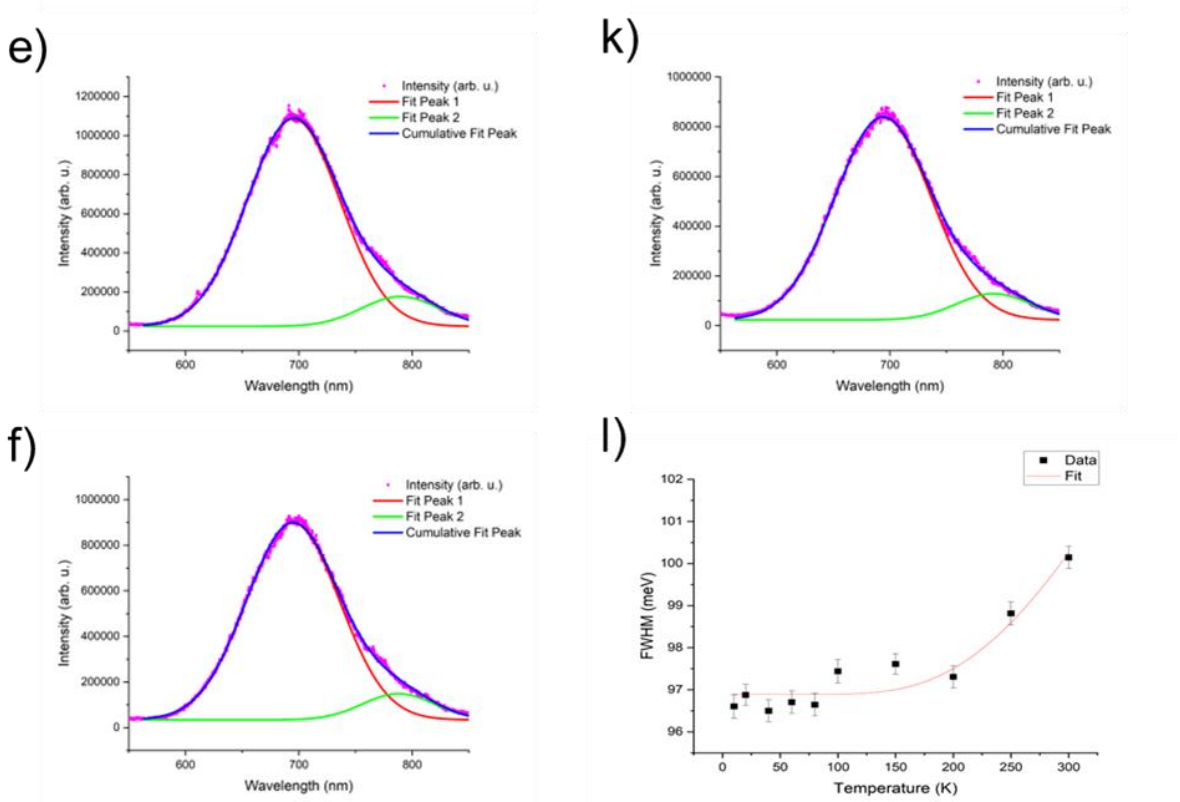

Figure 48. FWHM fitting of $Cs_3Bi_2I_9$ for PL at a) 5K, b) 10K, c) 20K, d) 40K, e) 60K, f) 80k, g) 100K, h) 150K, i) 200K, j) 250K k) 300K and the fitting for FWHM vs temperature l)

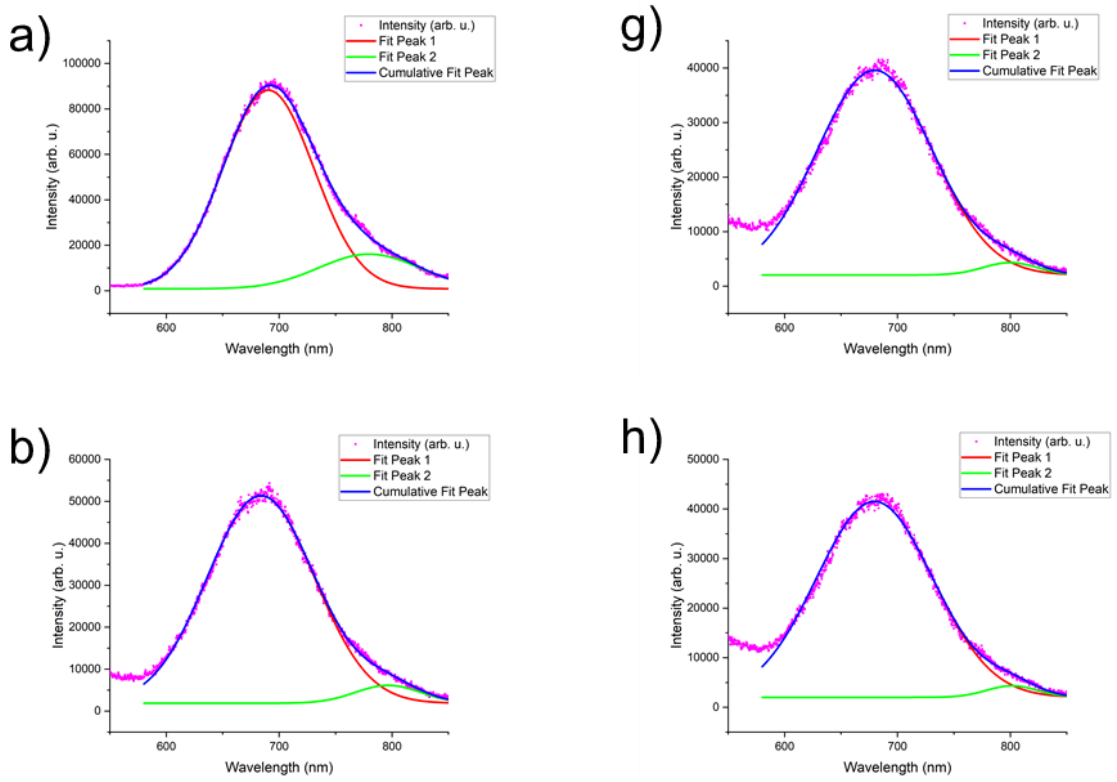

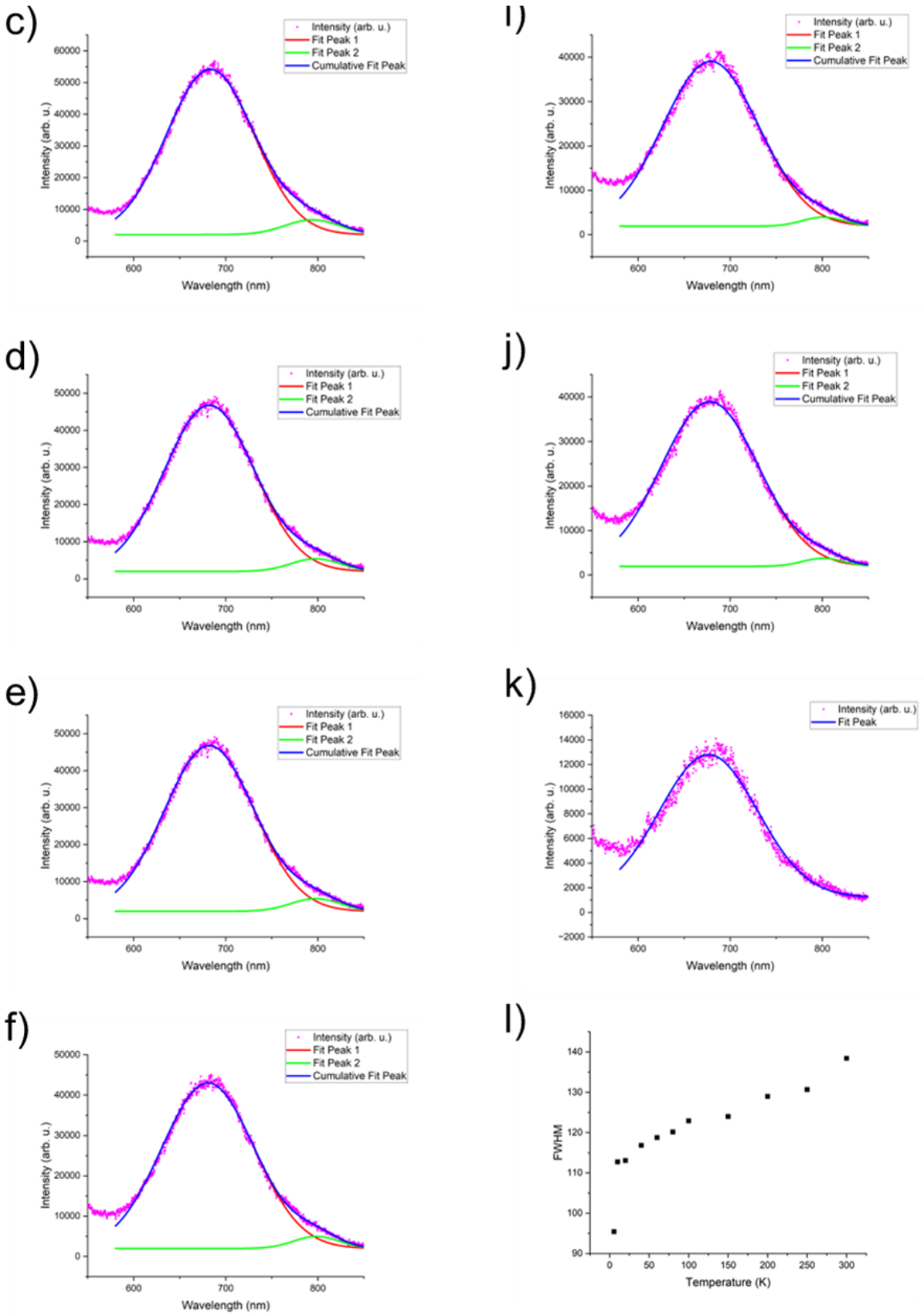

Figure 49. FWHM fitting of $Cs_3Sb_2I_9$ for PL at a) 5K, b) 10K, c) 20K, d) 40K, e) 60K, f) 80k, g) 100K, h) 150K, i) 200K, j) 250K k) 300K and the fitting for FWHM vs temperature l)

Bibliography

1. Gueymard, C.A., D. Myers, and K. Emery, *Proposed reference irradiance spectra for solar energy systems testing.* Solar Energy, 2002/12/01. **73**(6).
2. Peng, Y., et al., *Lead-Free Perovskite-Inspired Absorbers for Indoor Photovoltaics.* Advanced Energy Materials, 2021/01/01. **11**(1).
3. Ma, Q., et al., *One-step dual-additive passivated wide-bandgap perovskites to realize 44.72%-efficient indoor photovoltaics.* Energy & Environmental Science, 2024/03/05. **17**(5).
4. *Photovoltaic Modeling Handbook.*
5. *Characterization of photovoltaic devices for indoor light harvesting and customization of flexible dye solar cells to deliver superior efficiency under artificial lighting.* Applied Energy, 2015/10/15. **156**.
6. Apostolou, G., A. Reinders, and M. Verwaal, *Comparison of the indoor performance of 12 commercial PV products by a simple model.* Energy Science & Engineering, 2016/01/01. **4**(1).
7. Cotfas, D.T. and P.A. Cotfas, *Multiconcept Methods to Enhance Photovoltaic System Efficiency.* International Journal of Photoenergy, 2019/01/01. **2019**(1).
8. Freunek, M., M. Freunek, and L.M. Reindl, *Maximum efficiencies of indoor photovoltaic devices | IEEE Journals & Magazine | IEEE Xplore.* IEEE Journal of Photovoltaics, 2013. **3**(1).
9. *Internet of Things: market data & analysis*. 2024: Statista. Article.
10. Harrop, P. *Battery Elimination in Electronics and Electrical Engineering*. 2017. Article.
11. Pecunia, V., L.G. Occhipinti, and R.L.Z. Hoye, *Emerging Indoor Photovoltaic Technologies for Sustainable Internet of Things.* Advanced Energy Materials, 2021/08/01. **11**(29).
12. Shockley, W. and H.J. Queisser, *Detailed Balance Limit of Efficiency of p-n Junction Solar Cells.* Journal of Applied Physics, 1961/03/01. **32**(3).
13. DiLaura, D.L., *The lighting handbook: reference and application.* (No Title), 2011.
14. *Charge yield potential of indoor-operated solar cells incorporated into Product Integrated Photovoltaic (PIPV).* Renewable Energy, 2011/02/01. **36**(2).
15. Tang, G., P. Ghosez, and J. Hong, *Band-Edge Orbital Engineering of Perovskite Semiconductors for Optoelectronic Applications.* The Journal of Physical Chemistry Letters, 2021/03/17. **12**(17).
16. *Simulation and fabrication of all-inorganic antimony halide perovskite-like material based Pb-free perovskite solar cells.* Optical Materials, 2022/06/01. **128**.
17. Gleskova, H., et al., *Mechanical Theory of the Film-on-Substrate-Foil Structure: Curvature a.* Flexible Electronics, 2009.
18. Heo, J.H., et al., *Recent advancements in and perspectives on flexible hybrid perovskite solar cells.* Journal of Materials Chemistry A, 2019/01/15. **7**(3).

19. Huang, K., et al., *High-Performance Flexible Perovskite Solar Cells via Precise Control of Electron Transport Layer.* Advanced Energy Materials, 2019/11/01. **9**(44).
20. *Enhanced photoconversion efficiency in cesium-antimony-halide perovskite derivatives by tuning crystallographic dimensionality.* Applied Materials Today, 2020/06/01. **19**.
21. Shockley, W. and J. W. T. Read, *Statistics of the Recombinations of Holes and Electrons.* Physical Review, 1952-09-01. **87**(5).
22. *Optical and Electro-Optic Processes.* Dielectric Phenomena in Solids, 2004/01/01.
23. *Semiconductor Physical Electronics.* 2006.
24. del Alamo, J.A. and J.A. del Alamo, *Nanometre-scale electronics with III–V compound semiconductors.* Nature 2011 479:7373, 2011-11-16. **479**(7373).
25. *Solid State Physics.* Physics for Chemists, 2007/01/01.
26. Brandt, R.E., et al., *Searching for "Defect-Tolerant" Photovoltaic Materials: Combined Theoretical and Experimental Screening.* Chemistry of Materials, 2017. **29**(11): p. 4667-4674.
27. Yang, B. and K. Han, *Charge-Carrier Dynamics of Lead-Free Halide Perovskite Nanocrystals.* Accounts of Chemical Research, October 30, 2019. **52**(11).
28. Stoneham, A.M., et al., *Trapping, self-trapping and the polaron family.* Journal of Physics: Condensed Matter, 2007-05-30. **19**(25).
29. *Colloidal Synthesis and Charge-Carrier Dynamics of Cs2AgSb1−yBiyX6 (X: Br, Cl; 0 ⩽y ⩽ 1) Double Perovskite Nanocrystals.* Angewandte Chemie International Edition, 2019. **58**(8).
30. Emin, D., *Weak-coupling polarons: carrier-induced softening (Chapter 3) - Polarons.* 2012/11.
31. Rondiya, S.R., et al., *Self-trapping in bismuth-based semiconductors: Opportunities and challenges from optoelectronic devices to quantum technologies.* Applied Physics Letters, 2021/11/29. **119**(22).
32. *Band Offsets in Semiconductor Heterojunctions.* Solid State Physics, 1992/01/01. **46**.
33. Smith, A.M., A.M. Mohs, and S. Nie, *Tuning the Optical and Electronic Properties of Colloidal Nanocrystals by Lattice Strain.* Nature nanotechnology, 2009/01. **4**(1).
34. Musselman, K.P., Y. Ievskaya, and J.L. MacManus-Driscoll, *Modelling charge transport lengths in heterojunction solar cells.* Applied Physics Letters, 2012/12/17. **101**(25).
35. *Review: Progress in solar cells from hydrogenated amorphous silicon.* Renewable and Sustainable Energy Reviews, 2017/09/01. **76**.
36. *Band gap tuning of a-Si:H from 1.55 eV to 2.10 eV by intentionally promoting structural relaxation.* Journal of Non-Crystalline Solids, 1998/05/01. **227-230**.
37. *Microcrystalline and wide band gap p+ window layers for a-Si p-i-n solar cells.* Journal of Non-Crystalline Solids, 1987/12/02. **97-98**.

38. Dutta, P.S., et al., *Full Spectrum White LEDs of Any Color Temperature with Color Rendering Index Higher Than 90 Using a Single Broad-Band Phosphor.* ECS Journal of Solid State Science and Technology, 2017-11-11. **7**(1).
39. *Nanomanufacturing - Key control characteristics - Part 7-2: Nano-enabled photovoltaics - Device evaluation method for indoor light*. 2023, INTERNATIONAL ELECTROTECHNICAL COMMISSION. Article.
40. Ho, J.K.W., et al., *From 33% to 57% – an elevated potential of efficiency limit for indoor photovoltaics.* Journal of Materials Chemistry A, 2020/01/28. **8**(4).
41. Liu, S., et al., *Buried interface molecular hybrid for inverted perovskite solar cells.* Nature 2024 632:8025, 2024-06-26. **632**(8025).
42. *Organometal Halide Perovskites as Visible-Light Sensitizers for Photovoltaic Cells.* Journal of the American Chemical Society, 2009. **131**(17).
43. Katz, E.A., *Perovskite: Name Puzzle and German-Russian Odyssey of Discovery.* Helvetica Chimica Acta, 2020/06/01. **103**(6).
44. Hikami, S., et al., *High Tc Superconductors of the Perovskite Structure Oxides.* Japanese Journal of Applied Physics, 1987-01-01. **26**(S3-2).
45. *Perovskite solid electrolytes: Structure, transport properties and fuel cell applications.* Solid State Ionics, 1995/07/01. **79**.
46. *CaMn_{1−x} Nb_xO₃ (x ⩽ 0.08) Perovskite-Type Phases As Promising New High-Temperature n-Type Thermoelectric Materials.* Inorganic Chemistry, 2008. **47**(18).
47. He, H., et al., *Perovskite oxides as transparent semiconductors: a review.* Nano Convergence 2020 7:1, 2020-10-02. **7**(1).
48. Zheng, Z., et al., *Development of formamidinium lead iodide-based perovskite solar cells: efficiency and stability*. Chemical Science, 2022/02/23. **13**(8).
49. Du, X., et al., *Lead halide perovskite for efficient optoacoustic conversion and application toward high-resolution ultrasound imaging.* Nature Communications, 2021. **12**(1).
50. *Organometallic Halide Perovskites: Sharp Optical Absorption Edge and Its Relation to Photovoltaic Performance.* The Journal of Physical Chemistry Letters, 2014. **5**(6).
51. Kang, J. and L.-W. Wang, *High Defect Tolerance in Lead Halide Perovskite CsPbBr3.* The Journal of Physical Chemistry Letters, January 11, 2017. **8**(2).
52. Chen, L., et al., *High-Light-Tolerance PbI2 Boosting the Stability and Efficiency of Perovskite Solar Cells.* ACS Applied Materials & Interfaces, May 19, 2021. **13**(21).
53. Xu, J., et al., *Defect Tolerance of Mixed B-Site Organic–Inorganic Halide Perovskites.* ACS Energy Letters, November 5, 2021. **6**(12).

54. Suhail, M., et al., *Chalcogenide perovskites for photovoltaic applications: a review.* Journal of Nanoparticle Research 2022 24:7, 2022-07-06. **24**(7).
55. *Doping in inorganic perovskite for photovoltaic application.* Nano Energy, 2020/12/01. **78**.
56. *On the application of the tolerance factor to inorganic and hybrid halide perovskites: a revised system.* Chemical Science, 2016/06/21. **7**(7).
57. *An extended Tolerance Factor approach for organic–inorganic perovskites.* Chemical Science, 2015/05/18. **6**(6).
58. Sato, T., et al., *Extending the applicability of the Goldschmidt tolerance factor to arbitrary ionic compounds.* Scientific Reports 2016 6:1, 2016-04-01. **6**(1).
59. Bartel, C.J., et al., *New tolerance factor to predict the stability of perovskite oxides and halides.* Science Advances, 2019-02. **5**(2).
60. Umebayashi, T., et al., *Electronic structures of lead iodide based low-dimensional crystals.* Physical Review B, 2003-04-15. **67**(15).
61. Liu, M., et al., *Halide Perovskite Nanocrystal Emitters.* Advanced Photonics Research, 2021/03/01. **2**(3).
62. Duan, L., et al., *Stability challenges for the commercialization of perovskite–silicon tandem solar cells.* Nature Reviews Materials 2023 8:4, 2023-01-09. **8**(4).
63. Steele, J.A., et al., *Thermal unequilibrium of strained black CsPbI3 thin films.* Science, 2019-08-16. **365**(6454).
64. Keshavarz, M., et al., *Tracking Structural Phase Transitions in Lead-Halide Perovskites by Means of Thermal Expansion.* Advanced Materials, 2019/06/01. **31**(24).
65. P. Kore, B., et al., *The impact of moisture on the stability and degradation of perovskites in solar cells.* Materials Advances, 2024/03/18. **5**(6).
66. Xu, R.-P., et al., *In Situ Observation of Light Illumination-Induced Degradation in Organometal Mixed-Halide Perovskite Films.* ACS Applied Materials & Interfaces, February 12, 2018. **10**(7).
67. Huang, W., S.J. Yoon, and P. Sapkota, *Effect of Light Illumination on Mixed Halide Lead Perovskites: Reversible or Irreversible Transformation.* ACS Applied Energy Materials, May 29, 2018. **1**(6).
68. *Toward Eco-friendly and Stable Perovskite Materials for Photovoltaics.* Joule, 2018/07/18. **2**(7).
69. *Dye-Sensitized Solar Cell Goes Solid.* Small, 2012. **8**(24).
70. Igbari, F., Z.-K. Wang, and L.-S. Liao, *Progress of Lead-Free Halide Double Perovskites.* Advanced Energy Materials, 2019/03/01. **9**(12).

71. Correa-Baena, J.-P., et al., *A-Site Cation in Inorganic A3Sb2I9 Perovskite Influences Structural Dimensionality, Exciton Binding Energy, and Solar Cell Performance.* Chemistry of Materials, May 22, 2018. **30**(11).
72. Liao, W., et al., *Lead-Free Inverted Planar Formamidinium Tin Triiodide Perovskite Solar Cells Achieving Power Conversion Efficiencies up to 6.22%.* Advanced Materials, 2016/11/01. **28**(42).
73. Shi, Z., et al., *Lead-Free Organic–Inorganic Hybrid Perovskites for Photovoltaic Applications: Recent Advances and Perspectives.* Advanced Materials, 2017/04/01. **29**(16).
74. Tsai, C.-M., et al., *Formation of Stable Tin Perovskites Co-crystallized with Three Halides for Carbon-Based Mesoscopic Lead-Free Perovskite Solar Cells.* Angewandte Chemie, 2017/10/23. **129**(44).
75. Moyez, S.A., et al., *Thermal engineering of lead-free nanostructured CH3NH3SnCl3 perovskite material for thin-film solar cell.* Journal of Nanoparticle Research 2017 20:1, 2017-12-30. **20**(1).
76. Mercier, N., et al., *Structural diversity and retro-crystal engineering analysis of iodometalate hybrids.* CrystEngComm, 2009/04/20. **11**(5).
77. Krishnamoorthy, T., et al., *Lead-free germanium iodide perovskite materials for photovoltaic applications.* Journal of Materials Chemistry A, 2015/11/24. **3**(47).
78. Kopacic, I., et al., *Enhanced Performance of Germanium Halide Perovskite Solar Cells through Compositional Engineering.* ACS Applied Energy Materials, February 5, 2018. **1**(2).
79. Yu, B.-B., et al., *Heterogeneous 2D/3D Tin-Halides Perovskite Solar Cells with Certified Conversion Efficiency Breaking 14%.* Advanced Materials, 2021/09/01. **33**(36).
80. Chiara, R., M. Morana, and L. Malavasi, *Germanium-Based Halide Perovskites: Materials, Properties, and Applications.* ChemPlusChem, 2021/06/01. **86**(6).
81. Savill, K.J., A.M. Ulatowski, and L.M. Herz, *Optoelectronic Properties of Tin–Lead Halide Perovskites.* ACS Energy Letters, June 10, 2021. **6**(7).
82. Slavney, A.H., et al., *A Bismuth-Halide Double Perovskite with Long Carrier Recombination Lifetime for Photovoltaic Applications.* Journal of the American Chemical Society, February 10, 2016. **138**(7).
83. Greul, E., et al., *Highly stable, phase pure Cs2AgBiBr6 double perovskite thin films for optoelectronic applications.* Journal of Materials Chemistry A, 2017/09/26. **5**(37).
84. Ye, X., et al., *Computational screening of Cs based vacancy-ordered double perovskites for solar cell and photocatalysis applications.* EcoMat, 2023/03/01. **5**(3).
85. Hodgkins, T.L., et al., *Anionic order and band gap engineering in vacancy ordered triple perovskites.* Chemical Communications, 2019/03/07. **55**(21).

86. Filip, M.R., G. Volonakis, and F. Giustino, *Hybrid Halide Perovskites: Fundamental Theory and Materials Design.* Handbook of Materials Modeling, 2018.
87. Saparov, B., et al., *Thin-Film Preparation and Characterization of Cs3Sb2I9: A Lead-Free Layered Perovskite Semiconductor.* Chemistry of Materials, August 6, 2015. **27**(16).
88. Kihara, K., et al., *The crystal structures of β-Cs3Sb2Cl9 and Cs3Bi2Cl9.* urn:issn:0567-7408, 1974-04-15. **30**(4).
89. Pradhan, A., et al., *Effect of Bi Substitution on Cs3Sb2Cl9: Structural Phase Transition and Band Gap Engineering.* Crystal Growth & Design, April 14, 2020. **20**(5).
90. Kun, S.V., et al., *Phase equilibria in RbBr-Sb(Bi)Br3 systems and crystal structure of compounds of A31B25C97 (A1 - Rb, Cs; B5 -Sb, Bi; C7 - Br, I) type.* Neorganicheskie Materialy, 1993. **29**(3): p. 410-413.
91. Lazarini, F. and F. Lazarini, *Caesium enneabromodibismuthate(III).* urn:issn:0567-7408, 1977-09-15. **33**(9).
92. Aleksandrova, I.P., et al., *Low-Temperature Phase Transitions in the Trigonal Modification of Cs 3 Bi 2 Br 9 and Cs 3 Sb 2 I 9.* Phase Transitions, 2002-1-1. **75**(6).
93. Liu, P., et al., *Lead‐Free Cs3Sb2Br9 Single Crystals for High Performance Narrowband Photodetector.* Advanced Optical Materials, 2020/11/01. **8**(21).
94. Chabot, B., et al., *Cs3Sb2I9 and Cs3Bi2I9 with the hexagonal Cs3Cr2Cl9 structure type.* urn:issn:0567-7408, 1978-02-15. **34**(2).
95. Arakcheeva, A.V., et al., *The LT phase of Cs3Bi2I9.* Zeitschrift für Kristallographie - Crystalline Materials, 2001-04-01. **216**(4).
96. Ivanov, Y.N., et al., *Phase Transitions of Cs3Sb2I9 , Cs3Bi2I9 , and Cs3Bi2Br9 Crystals.* Inorganic Materials 2001 37:6, 2001/06. **37**(6).
97. Lehner, A.J., et al., *Crystal and Electronic Structures of Complex Bismuth Iodides A3Bi2I9 (A = K, Rb, Cs) Related to Perovskite: Aiding the Rational Design of Photovoltaics.* Chemistry of Materials, October 14, 2015. **27**(20).
98. Luévano-Hipólito, E., et al., *A Critical Review of the Use of Bismuth Halide Perovskites for CO2 Photoreduction: Stability Challenges and Strategies Implemented.* Catalysts 2022, Vol. 12, Page 1410, 2022-11-11. **12**(11).
99. Xia, M., et al., *Unveiling the Structural Descriptor of A3B2X9 Perovskite Derivatives toward X‐Ray Detectors with Low Detection Limit and High Stability.* Advanced Functional Materials, 2020/06/01. **30**(24).
100. Hoye, R.L.Z., et al., *The Role of Dimensionality on the Optoelectronic Properties of Oxide and Halide Perovskites, and their Halide Derivatives.* Advanced Energy Materials, 2022/01/01. **12**(4).

101. Drude, P., *Zur Elektronentheorie der Metalle; II. Teil. Galvanomagnetische und thermomagnetische Effecte.* Annalen der Physik, 1900/01/01. **308**(11).

102. P, U., M. E, and D.A. F, *Relativistic GW calculations on CH3NH3PbI3 and CH3NH3SnI3 perovskites for solar cell applications - PubMed.* Scientific reports, 03/26/2014. **4**(1).

103. Amat, A., et al., *Cation-Induced Band-Gap Tuning in Organohalide Perovskites: Interplay of Spin–Orbit Coupling and Octahedra Tilting.* Nano Letters, May 8, 2014. **14**(6).

104. López-Fernández, I., et al., *Lead-Free Halide Perovskite Materials and Optoelectronic Devices: Progress and Prospective.* Advanced Functional Materials, 2024/02/01. **34**(6).

105. Holanda, M.S.d., et al., *Layered metal halide perovskite solar cells: A review from structure-properties perspective towards maximization of their performance and stability.* EcoMat, 2021/08/01. **3**(4).

106. Ji, Z., et al., *Reducing current fluctuation of Cs3Bi2Br9 perovskite photodetectors for diffuse reflection imaging with wide dynamic range.* Science Bulletin, 2020/08/30. **65**(16).

107. Gu, J., et al., *Bandgap engineering of a lead-free defect perovskite Cs3Bi2I9 through trivalent doping of Ru3+*. RSC Advances, 2018/07/16. **8**(45).

108. Yu, B.-B., et al., *Alloy-induced phase transition and enhanced photovoltaic performance: the case of Cs3Bi2I9−xBrx perovskite solar cells.* Journal of Materials Chemistry A, 2019/04/09. **7**(15).

109. Shi, M., et al., *Tuning the Optoelectronic Property of All-Inorganic Lead-Free Perovskite via Finely Microstructural Modulation for Photovoltaics.* Small Methods, 2024/02/01. **8**(2).

110. T, G., et al., *Bandgap engineering in two-dimensional halide perovskite Cs3Sb2I9 nanocrystals under pressure - PubMed.* Nanoscale, 01/23/2020. **12**(3).

111. Bass, K.K., et al., *Vibronic Structure in Room Temperature Photoluminescence of the Halide Perovskite Cs3Bi2Br9.* Inorganic Chemistry, 2017.

112. Rieger, S., et al., *Excitons and narrow bands determine the optical properties of cesium bismuth halides.* Physical Review B, 2019-11-20. **100**(20).

113. Liu, Y.-L., et al., *Theoretical insight into the optoelectronic properties of lead-free perovskite derivatives of Cs3Sb2X9 (X = Cl, Br, I).* Journal of Materials Science 2018 54:6, 2018-11-27. **54**(6).

114. Pope, M. and C.E. Swenberg, *Electronic Processes in Organic Crystals and Polymers.* 1999/12/02.

115. Baranowski, M. and P. Plochocka, *Excitons in Metal-Halide Perovskites.* Advanced Energy Materials, 2020/07/01. **10**(26).

116. Galkowski, K., et al., *Determination of the exciton binding energy and effective masses for methylammonium and formamidinium lead tri-halide perovskite semiconductors.* Energy & Environmental Science, 2016/03/09. **9**(3).

117. Miyata, A., et al., *Direct measurement of the exciton binding energy and effective masses for charge carriers in organic–inorganic tri-halide perovskites.* Nature Physics 2014 11:7, 2015-06-15. **11**(7).

118. Li, S., et al., *Lead-Free All-Inorganic Cesium Bismuth Iodide-Based Perovskite Solar Cells: Recent Advances, Current Limitations, and Future Prospects.* Solar RRL, 2024/03/01. **8**(5).

119. Yoo, B., et al., *Structural, Electronic, and Optical Properties of the Vacancy-Ordered Bismuth–Antimony Perovskites (CH3NH3)3(Bi1–xSbx)2I9.* The Journal of Physical Chemistry C, April 25, 2021. **125**(17).

120. Biega, R.-I., et al., *Chemically Localized Resonant Excitons in Silver–Pnictogen Halide Double Perovskites.* The Journal of Physical Chemistry Letters, February 19, 2021. **12**(8).

121. Wang, C., et al., *Crystal structure engineering of metal halide perovskites for photocatalytic organic synthesis.* Chemical Communications, 2023/03/09. **59**(21).

122. Zhang, J., et al., *High Quantum Yield Blue Emission from Lead-Free Inorganic Antimony Halide Perovskite Colloidal Quantum Dots.* ACS Nano, September 11, 2017. **11**(9).

123. Shil, S.K., et al., *Two-Step Chemical Vapor Deposition-Synthesized Lead-Free All-Inorganic Cs3Sb2Br9 Perovskite Microplates for Optoelectronic Applications.* ACS Applied Materials & Interfaces, July 21, 2021. **13**(30).

124. D'Innocenzo, V., et al., *Excitons versus free charges in organo-lead tri-halide perovskites.* Nature Communications 2014 5:1, 2014-04-08. **5**(1).

125. Sendner, M., et al., *Optical phonons in methylammonium lead halide perovskites and implications for charge transport.* Materials Horizons, 2016/10/24. **3**(6).

126. Ioselevich, A. and E. Rashba, *Quantum tunneling in condensed media.* Eds. Yu. Kagan and AJ Leggett. Amsterdam, 1992: p. 347-425.

127. Xia, C.Q., et al., *Limits to Electrical Mobility in Lead-Halide Perovskite Semiconductors.* The Journal of Physical Chemistry Letters, April 6, 2021. **12**(14).

128. Hellwarth, R.W. and I. Biaggio, *Mobility of an electron in a multimode polar lattice.* Physical Review B, 1999-07-01. **60**(1).

129. Herz, L.M., *Charge-Carrier Mobilities in Metal Halide Perovskites: Fundamental Mechanisms and Limits.* ACS Energy Letters, June 8, 2017. **2**(7).

130. Wright, A.D., et al., *Electron–phonon coupling in hybrid lead halide perovskites.* Nature Communications 2016 7:1, 2016-05-26. **7**(1).

131. Keshavarz, M., et al., *Tuning the Structural and Optoelectronic Properties of Cs2AgBiBr6 Double-Perovskite Single Crystals through Alkali-Metal Substitution.* Advanced Materials, 2020/10/01. **32**(40).

132. Steele, J.A., et al., *Giant Electron–Phonon Coupling and Deep Conduction Band Resonance in Metal Halide Double Perovskite.* ACS Nano, August 7, 2018. **12**(8).

133. Kentsch, R., et al., *Exciton Dynamics and Electron–Phonon Coupling Affect the Photovoltaic Performance of the Cs2AgBiBr6 Double Perovskite.* The Journal of Physical Chemistry C, October 25, 2018. **122**(45).
134. Bartesaghi, D., et al., *Charge Carrier Dynamics in Cs2AgBiBr6 Double Perovskite.* The Journal of Physical Chemistry C, February 5, 2018. **122**(9).
135. Wolf, N.R., et al., *Doubling the Stakes: The Promise of Halide Double Perovskites.* Angewandte Chemie International Edition, 2021/07/19. **60**(30).
136. Pan, W., et al., *Cs2AgBiBr6 single-crystal X-ray detectors with a low detection limit.* Nature Photonics 2017 11:11, 2017-10-02. **11**(11).
137. Wu, B., et al., *Strong self-trapping by deformation potential limits photovoltaic performance in bismuth double perovskite.* Science Advances, 2021-02.
138. Wright, A.D., et al., *Ultrafast Excited-State Localization in Cs2AgBiBr6 Double Perovskite.* The Journal of Physical Chemistry Letters, March 30, 2021. **12**(13).
139. Turkevych, I., et al., *Potential of AgBiI4 rudorffites for indoor photovoltaic energy harvesters in autonomous environmental nanosensors.* Japanese Journal of Applied Physics, 2021-04-13. **60**(SC).
140. Kim, Y., et al., *Pure Cubic - Phase Hybrid Iodobismuthates AgBi2I7 for Thin - Film Photovoltaics.* Angewandte Chemie International Edition, 2016/08/08. **55**(33).
141. Zhu, H., et al., *Progress and applications of (Cu–)Ag–Bi–I semiconductors, and their derivatives, as next-generation lead-free materials for photovoltaics, detectors and memristors.* International Materials Reviews, 2024-01-15. **69**(1).
142. Tie, S., et al., *Efficient X-ray Attenuation Lead-Free AgBi2I7 Halide Rudorffite Alternative for Sensitive and Stable X-ray Detection.* The Journal of Physical Chemistry Letters, August 26, 2020.
143. Ghosh, B., et al., *Superior Performance of Silver Bismuth Iodide Photovoltaics Fabricated via Dynamic Hot - Casting Method under Ambient Conditions.* Advanced Energy Materials, 2018/11/01. **8**(33).
144. Sansom, H.C., et al., *Highly Absorbing Lead-Free Semiconductor Cu2AgBiI6 for Photovoltaic Applications from the Quaternary CuI–AgI–BiI3 Phase Space.* Journal of the American Chemical Society, March 8, 2021. **143**(10).
145. Sansom, H.C., et al., *Chemical Control of the Dimensionality of the Octahedral Network of Solar Absorbers from the CuI–AgI–BiI3 Phase Space by Synthesis of 3D CuAgBiI5.* Inorganic Chemistry, November 9, 2021. **60**(23).
146. Buizza, L.R.V., et al., *Interplay of Structure, Charge-Carrier Localization and Dynamics in Copper-Silver-Bismuth-Halide Semiconductors.* Advanced Functional Materials, 2022/02/01. **32**(6).

147. Islam, M.A., et al., *Enhanced surface morphology and photovoltaic properties of a new class of material copper silver bismuth iodide solar cell.* Journal of Materials Research and Technology, 2023/07/01. **25**.

148. Turkevych, I., et al., *Photovoltaic Rudorffites: Lead‐Free Silver Bismuth Halides Alternative to Hybrid Lead Halide Perovskites.* ChemSusChem, 2017/10/09. **10**(19).

149. Mashadieva, L.F., et al., *Experimental investigation of the Ag–Bi–I ternary system and thermodynamic properties of the ternary phases.* Journal of Alloys and Compounds, 2013/02/25. **551**.

150. Xiao, Z., et al., *Crystal Structure of AgBi2I7 Thin Films.* The Journal of Physical Chemistry Letters, September 21, 2016. **7**(19).

151. Fourcroy, P.H., et al., *Etude du systeme AgIBiI3.* Materials Research Bulletin, 1979/03/01. **14**(3).

152. Sansom, H.C., et al., *AgBiI4 as a Lead-Free Solar Absorber with Potential Application in Photovoltaics.* Chemistry of Materials, February 13, 2017. **29**(4).

153. Huang, Y.-T., et al., *Strong absorption and ultrafast localisation in NaBiS2 nanocrystals with slow charge-carrier recombination.* Nature Communications 2022 13:1, 2022-08-24. **13**(1).

154. Sansom, H.C., et al., *Chemical Control of the Dimensionality of the Octahedral Network of Solar Absorbers from the CuI–AgI–BiI3 Phase Space by Synthesis of 3D CuAgBiI5*. Inorganic Chemistry, November 9, 2021.

155. Bera, A., et al., *Energy landscape in silver-bismuth-iodide rudorffites: Combining scanning tunneling spectroscopy and Kelvin probe force microscopy.* Physical Review Materials, 2021-09-22. **5**(9).

156. Kulkarni, A., et al., *Concerted Ion Migration and Diffusion‐Induced Degradation in Lead‐Free Ag3BiI6 Rudorffite Solar Cells under Ambient Conditions.* Solar RRL, 2021/08/01. **5**(8).

157. Shao, Z., et al., *Exploring AgBixI3x + 1 semiconductor thin films for lead-free perovskite solar cells.* Materials & Design, 2018/03/05. **141**.

158. Jung, K.W., et al., *Silver bismuth iodides in various compositions as potential Pb-free light absorbers for hybrid solar cells.* Sustainable Energy & Fuels, 2017/12/19. **2**(1).

159. Zhu, H., et al., *High Photon‐to‐Current Conversion in Solar Cells Based on Light‐Absorbing Silver Bismuth Iodide.* ChemSusChem, 2017/06/22. **10**(12).

160. Zhai, W., et al., *Tuning the morphology and optoelectronic properties of AgBiI4 film through isopropanol treatment.* Journal of Materials Chemistry C, 2022/03/31. **10**(13).

161. Pai, N., et al., *Silver Bismuth Sulfoiodide Solar Cells: Tuning Optoelectronic Properties by Sulfide Modification for Enhanced Photovoltaic Performance.* Advanced Energy Materials, 2019/02/01. **9**(5).

162. Baranwal, A.K., et al., *Lead-free perovskite solar cells using Sb and Bi-based A3B2X9 and A3BX6 crystals with normal and inverse cell structures.* Nano Convergence 2017 4:1, 2017-09-22. **4**(1).

163. Lu, C., et al., *Inorganic and Lead-Free AgBiI4 Rudorffite for Stable Solar Cell Applications.* ACS Applied Energy Materials, August 24, 2018. **1**(9).

164. Shao, Z., et al., *AgBi2I7 layers with controlled surface morphology for solar cells with improved charge collection.* Materials Letters, 2018/06/15. **221**.

165. Kulkarni, A., et al., *Performance enhancement of AgBi2I7 solar cells by modulating a solvent-mediated adduct and tuning remnant BiI3 in one-step crystallization.* Chemical Communications, 2019/04/02. **55**(28).

166. Zhang, Q., et al., *Photovoltage Approaching 0.9 V for Planar Heterojunction Silver Bismuth Iodide Solar Cells with Li-TFSI Additive.* ACS Applied Energy Materials, May 7, 2019.

167. Hu, W., et al., *Bulk heterojunction gifts bismuth-based lead-free perovskite solar cells with record efficiency.* Nano Energy, 2020/02/01. **68**.

168. Seo, Y., et al., *Dynamic casting in combination with ramped annealing process for implementation of inverted planar Ag3BiI6 rudorffite solar cells.* Journal of Power Sources, 2020/03/31. **453**.

169. Zhu, H., et al., *Tuning the Bandgap in Silver Bismuth Iodide Materials by Partly Substituting Bismuth with Antimony for Improved Solar Cell Performance.* ACS Applied Energy Materials, July 16, 2020.

170. Yu, F., et al., *Cs-Incorporated AgBiI4 Rudorffite for Efficient and Stable Solar Cells.* ACS Sustainable Chemistry & Engineering, May 11, 2020. **8**(27).

171. Hosseini, S.S., et al., *The Effect of Multi-walled Carbon Nanotubes and Reduced Graphene Oxide Doping on the Optical and Photovoltaic Performance of Ag2BiI5-Based Solar Cells.* Journal of Electronic Materials 2020 49:10, 2020-08-13. **49**(10).

172. Crovetto, A., et al., *Parallel Evaluation of the BiI3, BiOI, and Ag3BiI6 Layered Photoabsorbers.* Chemistry of Materials, March 30, 2020. **32**(8).

173. Yi, Z., et al., *AgBi3I10 rudorffite for photovoltaic application.* Solar Energy, 2020/08/01. **206**.

174. Park, J.W., et al., *Enhancement of the photovoltaic properties of Ag2BiI5 by Cu doping.* Sustainable Energy & Fuels, 2021/03/09. **5**(5).

175. Wang, Y., et al., *Alkali-metal-ion-doping strategy to improve the photovoltaic properties of Ag2BiI5 solar cells.* New Journal of Chemistry, 2021/08/09. **45**(31).

176. Wu, M.-C., et al., *Composition engineering to enhance the photovoltaic performance and to prolong the lifetime for silver bismuth iodide solar cell.* Chemical Engineering Journal Advances, 2022/05/15. **10**.

177. Hsiao, K.-C., et al., *Doping engineering of carrier transporting layers for ambient-air-stable lead-free rudorffite solar cells prepared by thermal-assisted doctor blade coating.* Chemical Engineering Journal, 2023/01/01. **451**.

178. Wu, H., et al., *Bandgap Tuning of Silver Bismuth Iodide via Controllable Bromide Substitution for Improved Photovoltaic Performance.* ACS Applied Energy Materials, August 8, 2019. **2**(8).

179. Zhang, Q., et al., *Photovoltage Approaching 0.9 V for Planar Heterojunction Silver Bismuth Iodide Solar Cells with Li-TFSI Additive.* ACS Applied Energy Materials, May 7, 2019. **2**(5).

180. Dong, C., et al., *Lycopene‐Based Bionic Membrane for Stable Perovskite Photovoltaics.* Advanced Functional Materials, 2021/06/01. **31**(25).

181. KL, W., et al., *Ion-Dipole Interaction Enabling Highly Efficient CsPbI3 Perovskite Indoor Photovoltaics - PubMed.* Advanced materials (Deerfield Beach, Fla.), 2023 Aug. **35**(31).

182. Grandhi, G.K., et al., *Enhancing the Microstructure of Perovskite‐Inspired Cu‐Ag‐Bi‐I Absorber for Efficient Indoor Photovoltaics.* Small, 2022/09/01. **18**(35).

183. Arivazhagan, V., et al., *Indoor light harvesting lead-free 2-aminothiazolium bismuth iodide solar cells.* Sustainable Energy & Fuels, 2022/06/28. **6**(13).

184. Al-Anesi, B., et al., *Antimony‐Bismuth Alloying: The Key to a Major Boost in the Efficiency of Lead‐Free Perovskite‐Inspired Photovoltaics.* Small, 2023/11/01. **19**(46).

185. Al-Anesi, B., et al., *Antimony-bismuth alloying: the key to a major boost in the efficiency of lead-free perovskite-inspired indoor photovoltaics.* 2023/01/19.

186. Park, B.-W., et al., *Bismuth Based Hybrid Perovskites A3Bi2I9 (A: Methylammonium or Cesium) for Solar Cell Application.* Advanced Materials, 2015/11/01. **27**(43).

187. Johansson, M.B., H. Zhu, and E.M.J. Johansson, *Extended Photo-Conversion Spectrum in Low-Toxic Bismuth Halide Perovskite Solar Cells.* The Journal of Physical Chemistry Letters, August 22, 2016. **7**(17).

188. Lyu, M., et al., *Organic–inorganic bismuth (III)-based material: A lead-free, air-stable and solution-processable light-absorber beyond organolead perovskites.* Nano Research 2016 9:3, 2016-01-09. **9**(3).

189. Hoye, R.L.Z., et al., *Methylammonium Bismuth Iodide as a Lead‐Free, Stable Hybrid Organic–Inorganic Solar Absorber.* Chemistry – A European Journal, 2016/02/18. **22**(8).

190. Steele, J.A., et al., *Giant Electron–Phonon Coupling and Deep Conduction Band Resonance in Metal Halide Double Perovskite.* ACS Nano, August 7, 2018.

191. Frost, J.M., L.D. Whalley, and A. Walsh, *Slow Cooling of Hot Polarons in Halide Perovskite Solar Cells.* ACS Energy Letters, October 27, 2017. **2**(12).

192. Lei, H., D. Hardy, and F. Gao, *Lead‐Free Double Perovskite Cs2AgBiBr6: Fundamentals, Applications, and Perspectives.* Advanced Functional Materials, 2021/12/01. **31**(49).

193. Li, Z., et al., *Understanding the Role of Grain Boundaries on Charge‐Carrier and Ion Transport in Cs2AgBiBr6 Thin Films.* Advanced Functional Materials, 2021/12/01. **31**(49).
194. Nilă, A., et al., *Exciton–phonon interactions in the Cs3Bi2I9 crystal structure revealed by Raman spectroscopic studies.* physica status solidi (b), 2017/04/01. **254**(4).
195. Li, L., et al., *Colloid driven low supersaturation crystallization for atomically thin Bismuth halide perovskite.* Nature Communications 2023 14:1, 2023-06-23. **14**(1).
196. McCall, K.M., et al., *Strong Electron–Phonon Coupling and Self-Trapped Excitons in the Defect Halide Perovskites A3M2I9 (A = Cs, Rb; M = Bi, Sb).* Chemistry of Materials, April 26, 2017. **29**(9).
197. Acharyya, P., et al., *Extended Antibonding States and Phonon Localization Induce Ultralow Thermal Conductivity in Low Dimensional Metal Halide.* Advanced Functional Materials, 2023/10/01. **33**(41).
198. Bator, G., et al., *Raman studies of structural phase transition in Cs3Bi2Br9.* Vibrational Spectroscopy, 1998/03/01. **16**(1).
199. Wu, L., et al., *High‐Pressure Band‐Gap Engineering and Metallization in the Perovskite Derivative Cs3Sb2I9.* ChemSusChem, 2019/09/06. **12**(17).
200. Sun, Q., et al., *Anisotropic dielectric behavior of layered perovskite-like Cs3Bi2I9 crystals in the terahertz region.* Physical Chemistry Chemical Physics, 2020/11/04. **22**(42).
201. Tran, M.N., et al., *Resolving the discrepancies in the reported optical absorption of low-dimensional non-toxic perovskites, Cs3Bi2Br9 and Cs3BiBr6.* Journal of Materials Chemistry C, 2020/08/06. **8**(30).
202. Pazoki, M., et al., *Bismuth Iodide Perovskite Materials for Solar Cell Applications: Electronic Structure, Optical Transitions, and Directional Charge Transport.* December 15, 2016.
203. Malavasi, L., et al., *Band Gap Tuning Through Cation and Halide Alloying in Mechanochemical Synthesized Cs3(Sb1-xBix)2Br9 and Cs3Sb2(I1-xBrx)9 Solid Solutions.* 2023/04/21.
204. Toyozawa, Y., *Excitonic Instabilities of Deformable Lattice - from Self-Trapping to Phase Transition.* Acta Physica Polonica A, 1995. **87**(1): p. 47-56.
205. Schmidt, T., K. Lischka, and W. Zulehner, *Excitation-power dependence of the near-band-edge photoluminescence of semiconductors.* Physical Review B, 1992-04-15. **45**(16).
206. Li, Y., et al., *On the absence of a phonon bottleneck in strongly confined CsPbBr3 perovskite nanocrystals.* Chemical Science, 2019/06/12. **10**(23).
207. Stenutz, R., *Gutmann Acceptor and Donor number*. stenutz. Article.
208. A.Chandrasekaran. *Solvent Physical Properties*. Available from: https://people.chem.umass.edu/xray/solvent.html.

209. Singh, P. and K. Kaur, *Thermodynamic insight of DMSO-DMA and DMSO-DMF binary mixtures across varying temperatures.* Journal of Molecular Liquids, 2024/12/01. **415**.
210. *Gutmann Acceptor and Donor number*. Available from: Gutmann Acceptor and Donor number.
211. Zhang, J., et al., *Binary Solvent Engineering for High-Performance Two-Dimensional Perovskite Solar Cells.* ACS Sustainable Chemistry & Engineering, January 8, 2019. **7**(3).
212. Lal, S., et al., *The Role of Chemical Composition in Determining the Charge -Carrier Dynamics in (AgI)x(BiI3)y Rudorffites.* Advanced Functional Materials, 2024/08/01. **34**(32).